Pattern Recognition using Pulsed-Laser-Deposited $BiFeO_3$ Neuromorphic Devices for Advanced Artificial Intelligence.

A Thesis submitted

in partial fulfillment for the Degree of

Doctor of Philosophy

By

DAYAL G

SC17D020

Department of Physics

INDIAN INSTITUTE OF SPACE SCIENCE AND TECHNOLOGY

THIRUVANANTHAPURAM

MAY 2024

To my beloved parents, sister, and friends…

CERTIFICATE

This is to certify that the thesis entitled 'Pattern Recognition using Pulsed-Laser-Deposited $BiFeO_3$ Neuromorphic Devices for Advanced Artificial Intelligence,' submitted by Dayal G to the Indian Institute of Space Science and Technology, Thiruvananthapuram, in partial fulfillment for the award of the degree of Doctor of Philosophy, is a bona fide record of research work carried out by him under my supervision. The contents of this thesis, in full or in parts, have not been submitted to any other institution or university for the award of any degree or diploma.

Dr. K. B. Jinesh
Supervisor
Professor
Department of Physics

Dr Sudheesh Chethil
Professor and HOD
Department of Physics

Thiruvananthapuram
May 2024

DECLARATION

I declare that this thesis, entitled 'Pattern Recognition using Pulsed-Laser-Deposited $BiFeO_3$ Neuromorphic Devices for Advanced Artificial Intelligence,' submitted in partial fulfillment of the degree of Doctor of Philosophy, is a record of original work carried out by me under the supervision of Dr. K B Jinesh and has not formed the basis for the award of any other degree or diploma, in this or any other institution or university. In keeping with the ethical practice of reporting scientific information, due acknowledgments have been made wherever the findings of others have been cited.

Thiruvananthapuram-695 547 — Dayal G

May 2024 — SC17D020

ACKNOWLEDGEMENTS

First, I want to thank my supervisor, Dr. K B Jinesh from the Department of Physics at IIST. His guidance, support, and the freedom he gave me were key to my development as a researcher. His detailed feedback helped improve my research papers and thesis significantly. He created a supportive environment that encouraged me to think independently and confidently explore new research areas.

I'm also very grateful to the Directors of IIST, Dr. S. Unnikrishnan Nair, and former Directors, Dr. Sam Dayal and Dr. V. K. Dadhwal, for their role in providing excellent facilities that supported my research. Thanks also to Dr. Sudheesh Chethil, the current Head of the Department, and previous Heads, Dr. Umesh Kadhane and Dr. S. Murugesh, for their ongoing academic support and motivation.

The support from IIST was crucial, providing the necessary resources and facilities for my research. I owe a lot to my Doctoral Committee members as well, whose valuable feedback and encouragement guided me through my research. I also appreciate the faculty members in the Department of Physics at IIST, whose advice was crucial to completing my research successfully.

I’m thankful to the Council for Scientific and Industrial Research (CSIR, Government of India) for their financial support (File No: 09/1187(0001)/2017/EMR-1).

A special thank you to my seniors, juniors, and lab mates, whose friendship and teamwork greatly enriched my research experience. To my friends at IIST, I cherish our memories and am grateful for your support, which pushed me to keep going. I’m thankful to all my teachers over the years, whose guidance has always inspired me.

To my family, I cannot express enough how much your love and support mean to me. Special thanks to my parents, Amma and Achan, whose unwavering support and faith in my choices have been the foundation of my success. I also appreciate myself for embarking on this incredible journey and the divine for giving me the strength and guidance throughout.

To everyone who has been part of this journey, I am forever grateful. Your involvement has been invaluable, and I move forward not only with the knowledge I've gained but also with the deep relationships I've formed along the way.

ABSTRACT

The advent of neuromorphic technology marks a pivotal adaptation in modern computational hardware, addressing the evolving demands of artificial intelligence systems. This thesis underscores the importance of neuromorphic technologies in enhancing the interaction between software advancements and hardware capabilities, particularly how they can be immediately beneficial to society. The research presented here explores the use of Bismuth Iron Oxide (BFO), a multiferroic material, for developing neuromorphic devices due to its favourable material properties. A reactive pulsed laser deposition system, designed and assembled in our laboratory, was employed for the deposition of BFO thin films, which were then optimized for quality and consistency.

The core of this thesis revolves around the fabrication of neuromorphic devices using a straightforward metal-insulator-metal configuration, with Fluorine-doped tin oxide as the bottom electrode and gold as the top electrode. Comprehensive studies were conducted on the neuromorphic properties of these devices, with a specific focus on the nonlinearity of synaptic weight updates, which is crucial for real-world applications such as pattern recognition. Additionally, we investigated the impact of varying oxygen vacancy levels on the synaptic responses, revealing significant implications for device performance.

Furthermore, the practical applications of these neuromorphic devices were demonstrated through pattern recognition tasks, showcasing enhanced operational efficiency and accuracy when employing multiple devices simultaneously. This thesis not only presents the development and characterization of BFO-based neuromorphic devices but also exemplifies their potential integration into existing CMOS technology, offering a substantial leap towards advanced neuromorphic applications.

ABBREVIATIONS

AI	Artificial Intelligence
α	The NLF of potentiation
β	The NLF of depression
1T2R	One-transistor/2-resistor
2D	Two dimensional
AFM	Atomic Force Microscopy
ANN	Artificial Neural Networks
$BiFeO_3$, BFO	Bismuth Iron Oxide
CMOS	Complementary Metal-Oxide-Semiconductor
CNN	Convolutional Neural Network
DNNs	Deep neural networks
ECRAM	Electro-Chemical Random Access Memory
EPSC	Excitatory postsynaptic current
FeCAPs	Ferroelectric capacitors
FeFETs	Ferroelectric Field-Effect Transistors
FeRAM	Ferroelectric Random Access Memory
FTJs	Tunneling junctions
FTO	Fluorine doped tin oxide
HZO	$Hf_{0.5}Zr_{0.5}O_2$
IoT	Internet of Things
LTP	Long-term plasticity
MIM	Metal-insulator-metal
MNIST	Modified National Institute of Standards and Technology
MTJ	Magnetic tunnel junction
NLF	Nonlinearity factors
NVM	Non-volatile memory
PCM	Phase Change Memory
PLD	pulsed laser deposition
PPF	Paired-Pulse Facilitation

PZT	Lead zirconate titanate
ReLU	Rectified Linear Unit
RIR	Relative intensity ratio
RMS	Root-mean-square
RPLD	Reactive pulsed laser deposition
RRAM	Resistive Switching Random Access Memory
SNNs	Spiking neural networks
SOT-MRAM	Spin–Orbit Torque Magnetic Random Access Memory
STDP	Spike timing dependent plasticity
STP	Short-term plasticity
STT-MRAM	Spin-Transfer Torque Magnetic Random Access Memory
XPS	X ray photoelectron spectroscopy
XRD	X ray diffraction

TABLE OF CONTENTS

LIST OF TABLES

LIST OF FIGURES

Chapter 1:

Introduction

1.1 Need for Neuromorphic Computing; Von Neumann bottleneck.

Artificial Intelligence (AI) targets the replication of human cognitive abilities in machines. Today's supercomputers, while capable of complex calculations, fall short in efficiency compared to the human brain. Supercomputers, for instance, require about 500 seconds and consume megawatts of power to simulate just 5 seconds of brain activity.[1,2] This inefficiency is largely due to the von Neumann architecture, which separates memory and processing units, connected by a limited bus system, causing data transfer delays and energy loss.[3,4] Additionally, transistor density on chips is maxing out, with advances in lithography pushing the limits of miniaturization and challenging Moore's Law.[5]

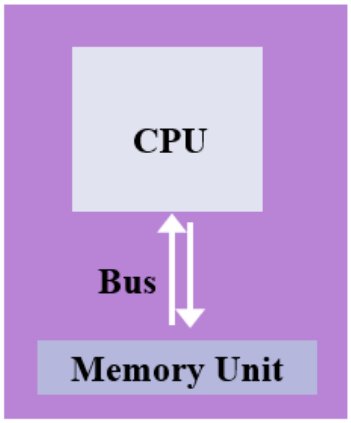

Figure 1.1 General architecture of a computer; von Neumann architecture.

The von Neumann architecture separates computing's brain and memory, causing inefficiency and high energy use.[6] This design has driven technological advances, shown in figure 1.1, but struggles under growing computational demands. The neuromorphic model, processing data where it is stored, offers a solution through parallel, low power operations, setting a goal for computing evolution.

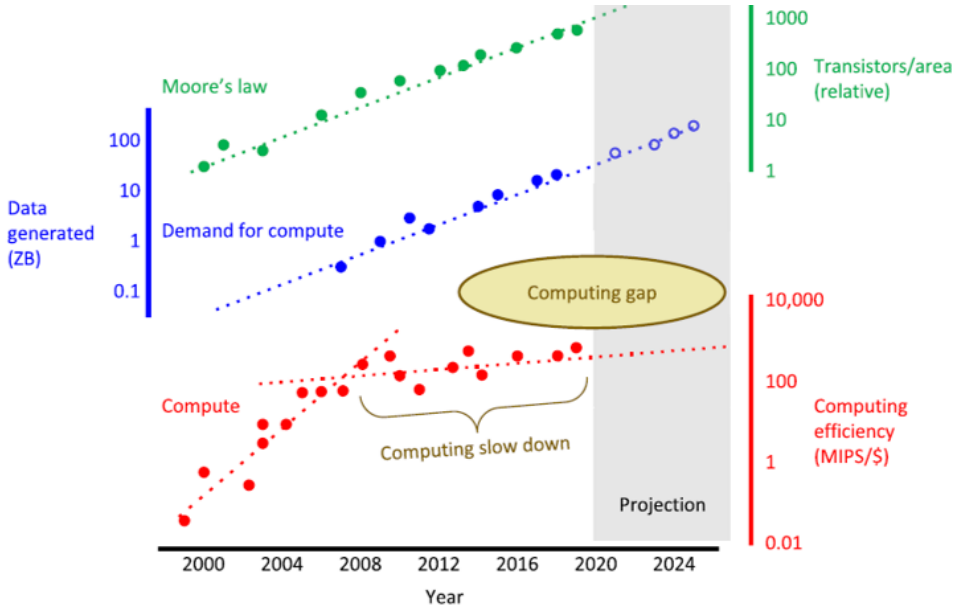

Figure 1.2 The need for neuromorphic technology due to the demand for the computation [7]

Neuromorphic computing, inspired by this brain like efficiency, aims to overcome von Neumann limitations. It focuses on artificial neurons capable of learning and memorizing, essential for mimicking brain functions. Current technology, however, falls short in replicating the brain's vast network of synapses due to the immense resources required for a single synapse, highlighting the gap between conventional computing and the desired brain like efficiency.[8]

In addition to the Von Neumann bottleneck, other significant challenges include Amdahl's law, which highlights the diminishing returns of parallel processing, limitations in lithography that restrict further miniaturization of transistors, and thermal management issues due to increased power density.[9–11]

Advancing beyond the von Neumann architecture, neuromorphic computing seeks to emulate the brain's functionality and efficiency. By developing nano scale devices for neuromorphic functions, this approach aims to bridge the gap, pushing towards a future where computing can process information as efficiently and compactly as the human brain, transforming artificial intelligence's capabilities.[12]

The gap between rapidly increasing data generation and the processing power of current computing systems is becoming more pronounced. The need for neuromorphic technology due to the demand for computation is shown in figure 1.2. This discrepancy highlights the limitations of the Von Neumann architecture and the slowing momentum

of Moore's Law.[13] As silicon-based technology approaches its physical limits, efficiency improvements, once predictable, are now stalling. This stagnation indicates we're hitting the ceiling of what our current computing technologies can achieve, emphasizing the urgent need for a shift in how we process information.[14]

Emerging needs call for innovations beyond traditional computing architectures to address the growing gap between data creation and processing capability. The pursuit of new technologies, such as parallel processing, quantum computing, and neuromorphic computing, offers potential pathways to overcome these limitations.[15] These advancements are crucial for enhancing our ability to manage and utilize the big volumes of data efficiently. Without adopting new computing paradigms, our capacity to process information will increasingly lag behind the pace of data generation, hindering progress in a data driven world. Contrastingly, the human brain processes information through parallel computing with its roughly 100 billion neurons and quadrillion synaptic connections, enabling complex functions like learning and memory with only about 20 watts of power. Thus, AI strives to emulate the human brain's efficiency in processing information.[14,16]

Efforts are increasing to create high density transistor interconnections on chips, leading to the development of neuromorphic chips such as IBM's TrueNorth, APT's SpiNNaker, and Intel's Loihi. Yet, these are still far from matching the brain's efficiency. Several software and hardware approaches have been proposed to enhance AI capabilities.[17] Software based platforms, like Alexa and Siri, incorporate algorithms capable of learning from experience. However, they require massive energy and data sets to function. Neuromorphic computing, combining non-volatile memory (NVM) devices with software like ANNs, shows improved performance but still relies on software, lacking the temporal dynamics necessary for emulating synaptic activities.[18,19]

1.2. Neuromorphic Devices

Neuromorphic devices can be designed to emulate various neural functions, including both neurons and synapses. While memristors are often used to replicate synaptic behavior due to their ability to retain memory states, other technologies like floating-gate transistors and ferroelectric capacitors can also function as synaptic

elements.[20,21] In the brain, synaptic junctions where neurons meet facilitate cognitive functions. Information from the senses triggers action potentials that travel through neurons. At synapses, neurotransmitter release and uptake alter synaptic junction currents, a process known as neuroplasticity, critical for memory formation.[22,23]

Neuromorphic devices use conductance and stimulating pulses to represent synaptic behavior and learning signals, respectively. Various mechanisms, like filament bridging and ion migration, tune device conductance, though terms like memristors and synaptic devices are often used interchangeably.[24–26]

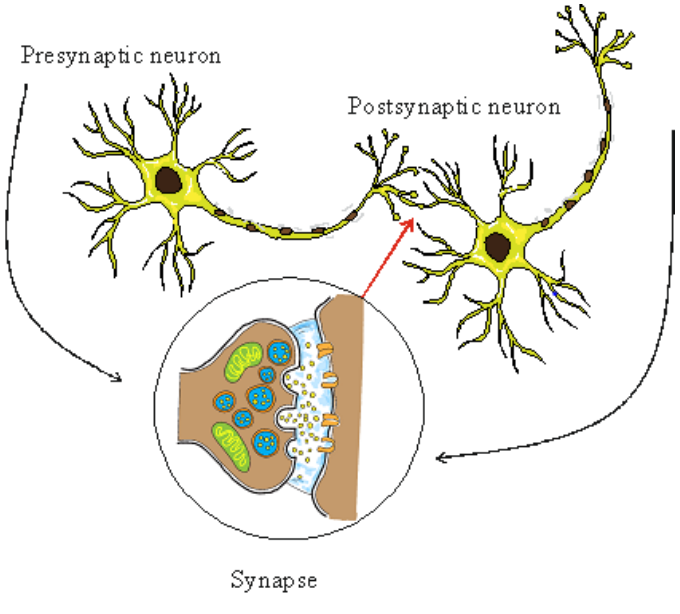

Figure 1.3 Schematics of a biological synapse

Neuromorphic computing also aims to emulate higher order cognition such as the sleep wake cycle and associative learning, often requiring complex CMOS circuits. Recent efforts focus on replicating human like behaviors in devices without external circuit support. [12] Neuromorphic computing aims at parallel information processing capability, real time processing, while it maintains the higher energy efficiency.[27] The fundamental hardware unit of this architecture can be termed as a neuromorphic device. A neuromorphic device is designed to emulate various aspects of neural activity, including the functions of synapses in biological systems. These devices replicate the dynamic processes of learning and memory by adjusting their conductance in response to electrical stimuli, similar to how synaptic strength is modulated in the brain.

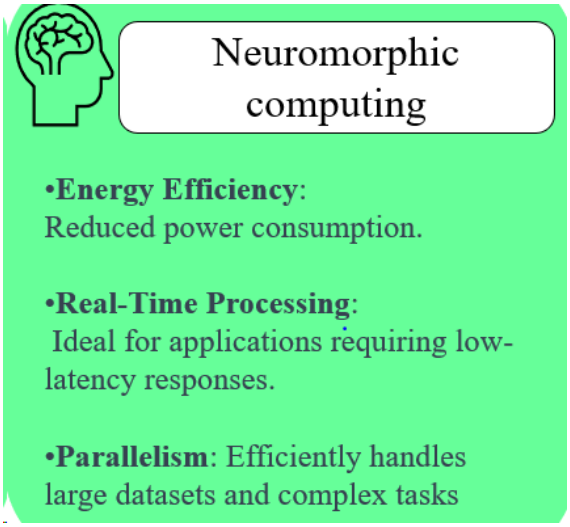

Figure 1.4 Advantages of Neuromorphic computing.

While the structure can be conceived as a simple metal insulator metal capacitor structure, with top electrode represents the preneuron, bottom electrode represents the post neuron, while the thin film sandwiched between the two electrodes represents the synapse.[28] Synapse is where the ion dynamics takes place and the conductance modulation happens. Just like in the real neurons the memory formation largely depends on the strengthening of the synaptic connections and hence the conductance across the synapse, here also the memory formation is due to the conductance variation of the thin film.[29]

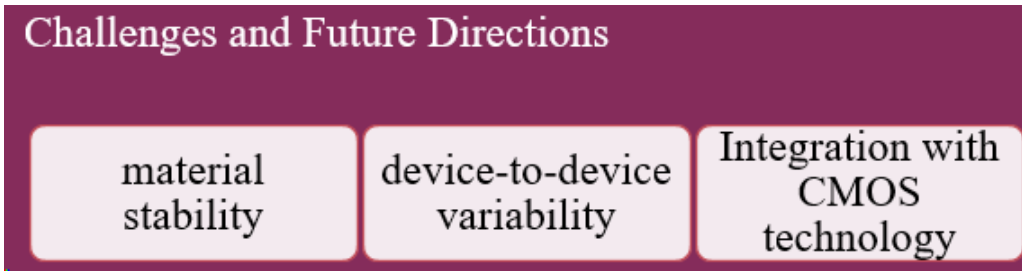

Figure 1.5 Challenges and Future directions.

When we look at the requirement for the neuromorphic devices, we understand that the key components like volatility, plasticity, and the availability of wide range of conductance states etcetera are factors to consider for the devices. The practicality of these devices in the real applications primarily depends on the performance of the devices, energy consumption, and finally scalability.[30,31]

Volatility in neuromorphic devices is defined by their capability to maintain conductance states even when not powered, a critical feature for practical applications.

This characteristic ensures that learned information and computational states are preserved, allowing for the continuation of processes and retention of data across power cycles. It's a cornerstone for devices aiming for long term operation and reliability in real world scenarios.[32,33]

While nonvolatility is important for applications requiring long-term memory retention, volatility is equally critical in scenarios that mimic transient brain functions, such as short-term memory and dynamic learning processes. Volatile neuromorphic devices can offer significant advantages in energy efficiency and speed for certain computational tasks, highlighting the diverse approaches within neuromorphic computing.

Plasticity, on the other hand, describes the adaptability of neuromorphic devices, allowing them to modify their internal connections in response to external stimuli.[27] This feature is inspired by the biological processes observed in the human brain, where synaptic connections strengthen or weaken based on experiences. This ability for self-modification enables neuromorphic devices to learn from their environment, adapt to new situations, and evolve over time, making them highly effective for tasks requiring complex computation and decision-making processes.

Together, volatility and plasticity form the foundation of neuromorphic devices, enabling them to function efficiently in a wide range of applications. By mimicking the brain's mechanisms for memory retention and learning, these devices offer a new paradigm in computing, characterized by resilience, adaptability, and the capacity for continuous learning.[34]

Synaptic plasticity is central to this concept, where the strength of connections changes in response to activity patterns, facilitating learning. Hebbian learning reinforces this by strengthening connections when cells activate simultaneously, embodying the principle that "cells that fire together, wire together."[23,27,35,36] Spike Timing Dependent Plasticity (STDP) further refines this by adjusting connections based on the precise timing of signals, enabling more accurate learning from temporal patterns. Homeostatic plasticity maintains network stability, preventing overexcitation or inhibition, crucial for sustainable learning.[37,38]

Lastly, structural plasticity allows for the dynamic reconfiguration of the network itself, forming new connections or pruning existing ones in response to learning

demands. This adaptability opens up broad applications, from adaptive sensors to advanced machine learning, highlighting neuromorphic devices' potential to revolutionize computing with efficient, real-time learning and decision-making capabilities.

The ability of neuromorphic devices to operate across a wide range of conductance states is a vital attribute, significantly enhancing their dynamic range. This broad spectrum of conductance enables these devices to simulate the analog nature of biological synapses more accurately, where the strength of synaptic connections can vary greatly.[39] By capturing this variability, neuromorphic devices can implement more nuanced and flexible computational models, allowing for a richer representation of information.[40] This, in turn, facilitates the execution of complex cognitive tasks such as learning, pattern recognition, and sensory processing with greater efficiency and precision. The extended dynamic range afforded by variable conductance states thus plays a crucial role in advancing the capabilities and performance of neuromorphic computing systems.[41]

Neuromorphic devices' practicality hinges on performance, energy use, and scalability. Performance wise, these devices need to process and store information quickly, accurately, and reliably to handle complex tasks like pattern recognition and decision making efficiently. This capability is crucial for their application in areas such as robotics and data analysis, where processing vast amounts of data quickly is essential.[42,43]

Energy consumption is equally critical. Neuromorphic computing aims to significantly reduce the energy needed for computations, making these devices ideal for environments where power is limited, like in mobile and wearable tech. The challenge lies in designing devices that mimic the brain's energy efficiency, enabling powerful computing with minimal power use.[44,45]

Lastly, scalability determines neuromorphic devices' widespread adoption. They must easily scale from small to large applications while maintaining performance and efficiency. Overcoming fabrication and integration challenges is key to achieving this, enabling their use across various sectors.[46] Scalability, performance, and low energy use are pivotal for neuromorphic devices' success in real world applications.

Neuromorphic devices face key challenges: material stability, device to device variation, and integration with existing CMOS technology. Material stability is vital as the long term performance of these devices heavily relies on the consistent behavior of their constituent materials.[30,47] Selecting materials that maintain their properties over time is critical to ensuring device reliability and functionality throughout their intended lifespan.

Device to device variation presents another significant hurdle. Inconsistencies between individual neuromorphic devices can lead to complications in their operation and overall system performance. Achieving uniformity across devices is essential for their reliable application in complex computational tasks, where precision and predictability are paramount.[48] The final challenge lies in integrating neuromorphic devices with the well-established CMOS technology. For neuromorphic technologies to be practically applicable, they must seamlessly blend with existing semiconductor technologies. This integration is crucial for leveraging the strengths of both neuromorphic and CMOS technologies, facilitating their adoption in a wide range of applications.[49,50] While neuromorphic devices are not expected to replace CMOS technology entirely, their coexistence is anticipated to enhance computational capabilities, combining the best of both worlds for advanced technological solutions.

1.2.1 Two-Terminal Neuromorphic Devices: Advances in Memory Technologies

Two-terminal neuromorphic devices, typically leveraging memristive technology, are distinguished by their dual-contact configuration. These devices are valued for their straightforward design and efficacy in emulating synaptic functions. Functionally, they operate on the principle that input voltage or current induces a change in resistance across the terminals.[51] This change is akin to synaptic plasticity in biological systems—the fundamental process that allows synapses to strengthen or weaken over time, which is vital for learning and memory.

- Key Features of Two-Terminal Neuromorphic Devices: Memristors: These are the most prevalent form of two-terminal neuromorphic devices. They remember past voltages or currents, reflecting this history as changes in resistance. This capability enables them to retain information, positioning them as suitable candidates for non-volatile memory applications.[52]

- Simplicity: With only two contacts, these devices are easier to manufacture and incorporate into larger systems.
- Energy Efficiency: These devices typically use less power, which is beneficial in energy-sensitive applications.

These characteristics make two-terminal devices particularly valuable for creating compact, energy-efficient neural network architectures that mimic the operational speeds and efficiencies of biological systems.[53]

Various Types of Two-Terminal Neuromorphic Devices:

Resistive Switching Random Access Memory (RRAM): This technology features a metal-insulator-metal (MIM) configuration where the insulating layer can switch between high and low resistance states. Initially, a 'forming' process creates a conductive filament within the insulator to lower resistance. Subsequent voltage pulses can toggle the device between these states, with variations like unipolar and bipolar RRAM offering different mechanisms for switching.[54,55]

Phase Change Memory (PCM): PCM devices operate through a shift in the phase of the active material, typically a chalcogenide compound. Electrical pulses trigger transitions between crystalline and amorphous states, markedly changing the resistance.[56]

Spin-Transfer Torque Magnetic Random Access Memory (STT-MRAM): These devices use a magnetic tunnel junction (MTJ) structure with ferromagnetic metal electrodes. Resistance changes depending on the alignment of magnetic polarizations within the electrodes, controlled by spin-transfer torque. This type is known for rapid switching and high durability but generally supports only binary resistance states.[57]

Ferroelectric Random Access Memory (FeRAM): In FeRAM, a ferroelectric insulator is sandwiched in a MIM stack. External biases orient the electrical dipoles, with polarization state changes detectable via displacement currents generated during switching.[58,59] However, the reading process in FeRAM is destructive to the existing state, which can make it both time-consuming and energy demanding.

These two-terminal devices each have unique structures and mechanisms that facilitate the modification and detection of memory states through electrical impulses, enhancing their scalability over traditional Flash memory. Their varied functionalities

and operational characteristics are making significant impacts in the field of neuromorphic computing, driving advancements in memory technology and beyond.

1.2.2 Advanced Functionalities of Three-Terminal Neuromorphic Devices

Three-terminal neuromorphic devices offer an enhancement over their two-terminal counterparts by incorporating an additional terminal, which allows for more intricate functionality and control. These devices typically utilize transistor-like structures where one of the terminals is used to modulate the flow of current between the other two. This configuration enables precise control over the device's conductive state, facilitating more sophisticated emulation of synaptic behaviors.

Key Features of Three-Terminal Neuromorphic Devices are:

Transistor-Based Architecture-: In devices like floating gate transistors, a terminal is dedicated to controlling the flow of electrons within the device, effectively altering the conductivity in response to input signals. This capability allows for dynamic adjustments in the device's operational state, closely mimicking synaptic activities.

Enhanced Functionality-: The additional terminal introduces gating mechanisms, which can emulate complex synaptic functions such as facilitation and depression. This enhanced functionality supports the replication of more nuanced neural interactions, a key aspect of simulating brain-like capabilities.

Circuit Design Flexibility-: With the extra terminal, designers can create more complex circuits that emulate larger portions of neural systems, including entire neural pathways. This flexibility is crucial for developing advanced neuromorphic systems that require dynamic reconfiguration and sophisticated network interactions.

Applications and Implications

These advanced features make three-terminal neuromorphic devices particularly suitable for sophisticated applications where adaptability and learning are essential. For instance, they play a pivotal role in developing dynamic neuromorphic systems capable of complex learning and memory tasks, significantly enhancing the capabilities of artificial neural networks.

Examples of Three-Terminal Devices

Ferroelectric Field-Effect Transistors (FEFETs)-: These devices use a MOS structure with a ferroelectric layer as the gate dielectric. The gate voltage alters the polarization state of the ferroelectric material, adjusting the threshold voltage of the FEFET. This allows for non-destructive read operations and supports high-density configurations such as vertical 3D structures, making FEFETs highly suitable for compact and efficient memory arrays.[60]

Electro-Chemical Random Access Memory (ECRAM)-: ECRAM devices feature a solid-state electrolyte as the gate dielectric which facilitates ion migration, notably Li+ ions, within a lithium phosphorous oxynitride electrolyte. The gate voltage direction influences the ions' movement, which modulates the device's conductivity and effectively decouples the writing and reading pathways. This unique mechanism enhances conductance update linearity, making ECRAM devices highly promising for emulating synaptic connections.[61]

Spin–Orbit Torque Magnetic Random Access Memory (SOT-MRAM)-: SOT-MRAM operates similarly to STT-MRAM but utilizes a current through a heavy metal electrode to switch the magnetization state of the ferromagnetic layers via spin-polarized electron accumulation induced by spin Hall or Rashba effects. This technology achieves fast switching times and improved endurance, making it suitable for high-performance memory applications.[62]

Memristive Transistors (Memtransistors)-: These incorporate a polycrystalline 2D semiconductor as the channel in a MOS structure, where applying a voltage can trigger a resistance transition through mechanisms such as grain boundary or impurity migration. Memtransistors combine memory and processing capabilities, exhibiting neuromorphic features like spike accumulation and spike-timing plasticity.[63]

In summary, three-terminal neuromorphic devices expand the boundaries of what's possible in simulating neural functions, offering enhanced control, functionality, and flexibility. Their ability to emulate complex synaptic behaviors and integrate into sophisticated circuits makes them a cornerstone in the ongoing evolution of neuromorphic technology.

1.3 Materials for Neuromorphic Technology

Phase-Change Memory (PCM): PCM materials are crucial due to their ability to switch between different physical states, thus allowing the emulation of synaptic behaviors in neuromorphic systems. These changes in state can reliably represent the varying strength of synaptic connections.

Memristive Oxide-Filament Resistive Devices: Utilizing the property of resistance change based on the history of applied voltage, these devices offer a way to mimic the plasticity of synapses, critical for learning and memory in the brain.[64]

Electrochemical Metal-Filament Devices: These are designed to form and dissolve conductive filaments under electrical influence, replicating the dynamic nature of synaptic functions.

Nonfilamentary RRAM Materials: As a variant of resistive random-access memory, nonfilamentary RRAM provides a scalable and reliable option for neuromorphic computing, avoiding the pitfalls of filament instability.[65]

Topological Insulator Materials: These materials are noted for their unique electronic properties, which facilitate low-power and efficient computations akin to neural processes, potentially enhancing the computational efficiency of neuromorphic systems.[66]

These materials form the backbone of developing dense, low-power, and highly connected arrays that mimic the brain's architecture, playing a pivotal role in overcoming the limitations of traditional computing, especially in processing complex, unstructured data.[67]

Ferroelectric and Multiferroic Materials

Ferroelectric and multiferroic materials stand out in the realm of neuromorphic computing for their distinctive ability to maintain and switch electrical polarization states, similar to binary states in digital memory but with the added flexibility and speed suited for analog processing.[68]

Ferroelectric synapses utilize the shifting polarization within ferroelectric domains to modulate synaptic conductance, crucial for mimicking the learning and memory

functions of the brain. Materials like lead zirconate titanate (PZT) or $Hf_{0.5}Zr_{0.5}O_2$ (HZO) are common, where their polarization orientation can be altered by external electric fields, affecting the resistance of the device.[69]

Innovative designs, such as those studied by Boyn et al. and Guo et al., demonstrate the use of ferroelectric materials in complex stacked structures that allow for nuanced control of synaptic behaviors through electric fields.[70,71] These structures not only facilitate basic ON and OFF states but also enable intermediate states by adjusting the proportion of domains oriented upwards or downwards, thus enhancing the mimicking of time-dependent synaptic plasticity.[68,72,73]

Challenges and Advances in Ferroelectric Technology

Despite the promising functionalities of ferroelectric materials, they face challenges such as scalability, data retention, and integration with existing technologies.[74] Ferroelectric capacitors (FeCAPs), field-effect transistors (FeFETs), and tunneling junctions (FTJs) each bring specific advantages and hurdles:

- FeCAPs and FeFETs are explored for their direct control over voltages and potential for high-density memory but struggle with issues related to endurance and scalability.
- FTJs offer a method to measure current changes non-destructively through a ferroelectric barrier, although increasing current density remains a challenge for broader applications.[73]

By better understanding ferroelectric phases and optimizing material structures, there is significant potential to enhance the performance and reliability of these devices, paving the way for their expanded use in complex computing applications.[75]

In our quest for the ideal material for neuromorphic applications, we identified Bismuth Iron Oxide ($BiFeO_3$, BFO) as a standout candidate. This ternary oxide perovskite, known as Bismuth Ferrite, boasts a complex ABO_3 perovskite structure, classifying it as multiferroic material. BFO is distinguished by its simultaneous display of ferroelectricity and antiferromagnetism, making it a material of considerable interest in the field. One of its notable attributes is the ability to exhibit large polarization at room temperature, a characteristic that greatly enhances its applicability in various devices.[69,76–78]

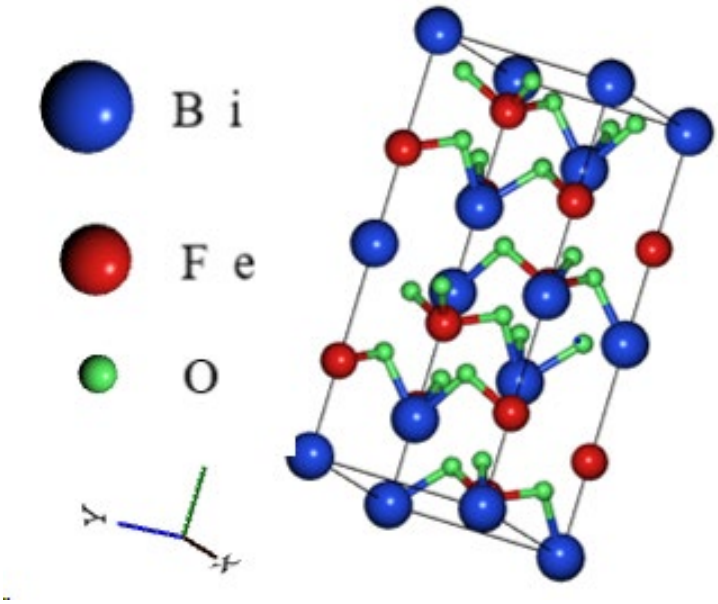

Figure 1.6 $BiFeO_3$ molecular structure.

BFO thin films, crucial for device miniaturization and integration, can be fabricated through several methods, including the sol gel process and, more prominently, pulsed laser deposition (PLD). PLD, in particular, has been recognized for its capability to produce thin films of superior quality. This method allows for precise control over the film's composition and structure, ensuring the material's properties are optimized for the intended application.[53,77]

Pulsed Laser Deposition (PLD) stands out as the preeminent technique for the deposition of Bismuth Iron Oxide ($BiFeO_3$) due to its unparalleled ability to ensure controlled deposition and high film quality.[79] The precision afforded by PLD allows for meticulous control over the deposition process, which is critical for achieving uniformity and consistency in the thickness and composition of the deposited films. This level of control is essential for applications of BFO, where the functional properties of the material are highly dependent on the structural integrity and uniformity of the films.[80] Moreover, the enhanced film quality achievable with PLD is instrumental in realizing the desirable structural and functional properties of BFO, including its magnetic and ferroelectric characteristics, which are pivotal for its use in various advanced technological applications.[81]

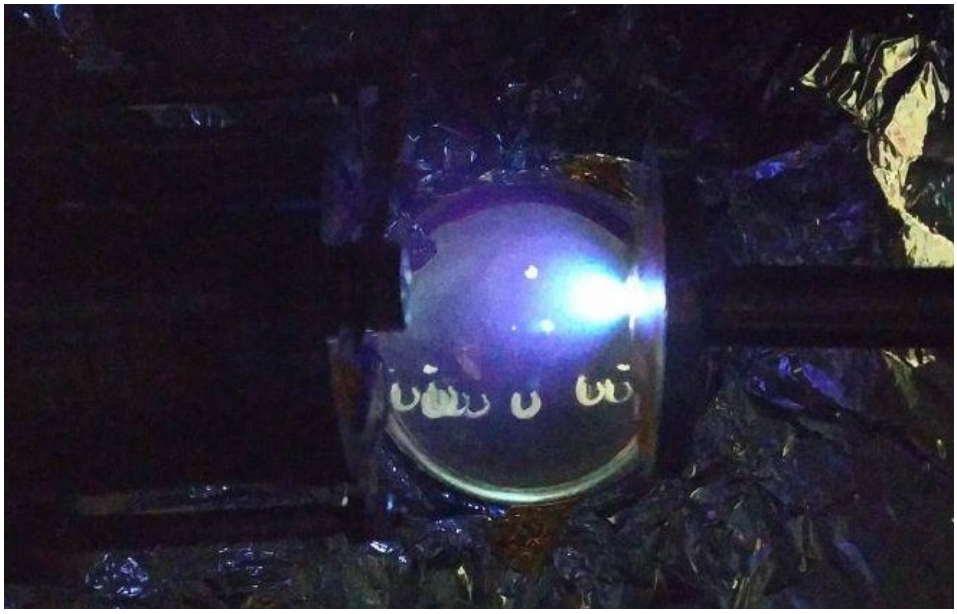

Figure 1.7 Pulsed Laser Deposition

Furthermore, PLD's versatility in accommodating a wide range of materials and its specific effectiveness for oxide deposition make it particularly suitable for complex oxide compounds like $BiFeO_3$. The technique's ability to ensure thorough oxygenation of the films is crucial for optimizing the material's properties, as the oxygen content directly influences the phase composition and, consequently, the physical properties of BFO films.[82] The flexibility in adjusting deposition parameters, such as substrate temperature, further enhances PLD's suitability for tailoring the properties of $BiFeO_3$ films to meet specific application requirements. These attributes collectively underscore why PLD is considered the best choice for depositing BFO films, offering a unique blend of precision, quality, and versatility that is critical for harnessing the full potential of this complex oxide material.[83]

During the fabrication of our neuromorphic devices, we paid special attention to ensuring that the processes were compatible with existing CMOS technology. Specifically, we optimized the substrate temperature during the pulsed laser deposition to approximately 400°C. This careful calibration was done to ensure that the temperature remained within a range that would not compromise CMOS technology's integrity. This integration strategy underscores our commitment to developing materials and processes that not only advance the capabilities of neuromorphic computing but also harmonize with established semiconductor manufacturing techniques, paving the way for broader application and adoption.[53,84]

1.4 Application Domains of Neuromorphic Technology and Research Challenges

The ability of neuromorphic technology to process data efficiently and in a manner similar to the human brain has led to significant interest from various industries.

1.4.1 Image and Pattern Recognition in AI Software

One of the key areas where neuromorphic technology excels is in image and pattern recognition, particularly when paired with AI software. Deep neural networks (DNNs) and spiking neural networks (SNNs) that run on neuromorphic hardware can handle complex visual data with remarkable speed and accuracy. This capability makes them invaluable for applications such as facial recognition, automated surveillance systems, and autonomous vehicle navigation. The combination of neuromorphic technology with AI software enables real-time processing and decision-making, which is crucial for tasks that require immediate responses, such as recognizing and classifying objects in a camera feed.[19,49,85]

1.4.2 Medical Applications

Neuromorphic technology has a profound impact on the medical field. It facilitates the development of "lab on a chip" technologies, which combine sensors and processors into compact devices capable of performing complex analyses. This allows for rapid diagnostic testing, reducing the need for extensive lab work and enabling quick responses to health concerns. Additionally, neuromorphic technology can enhance pattern recognition for medical imaging, particularly in the detection of cancer and tumours. By mimicking the brain's pattern recognition capabilities, these technologies can sift through vast amounts of imaging data, highlighting anomalies, and facilitating early diagnosis, which is critical for effective treatment.[86,87]

1.4.3 Big Data and the Internet of Things

Neuromorphic technology is also making strides in the domains of Big Data and the Internet of Things (IoT). Neuromorphic processors can handle multiple data streams simultaneously, making them ideal for managing the extensive data generated by IoT devices. This capability is crucial for smart home systems, urban infrastructure management, and industrial automation, where real-time data processing from various

sources is necessary. The energy-efficient nature of neuromorphic chips also makes them well-suited for IoT applications, allowing devices to operate for extended periods in remote or challenging environments.[88,89]

1.5 Research Challenges

While neuromorphic technology has shown promise across these domains, there are several research challenges that must be addressed to fully realize its potential.

1.5.1 Scalability

One of the main challenges is scalability. As neuromorphic systems grow in complexity, managing larger networks of neurons and synapses becomes increasingly difficult. Researchers are working to develop scalable architectures that can handle these extensive networks while maintaining performance and functionality.[90]

1.5.2 Material and Device Development

Finding materials and devices that can accurately replicate biological neural functions is another major hurdle. Current materials may lack the durability or stability needed for long-term operation, prompting ongoing research into new materials that can fulfil these requirements.[48,91]

1.5.3 Programming and Integration

Neuromorphic systems require novel programming approaches that reflect their unique neural adaptation capabilities. Additionally, integrating these systems into existing computing infrastructures is complex, necessitating the development of new hardware interfaces and software platforms to facilitate seamless communication with traditional technologies.[92]

1.5.4 Energy Efficiency

While neuromorphic chips are inherently more energy-efficient than traditional processors, optimizing their energy consumption is crucial for practical deployment. Enhancing their energy efficiency is key to ensuring sustainability, particularly as they scale up.[44,93]

In conclusion, neuromorphic technology offers significant promise across various domains, including AI software, medical applications, and Big Data. However, to fully

unlock its potential, research and development must continue to address challenges in scalability, materials, programming, integration, and energy efficiency.

1.6 Challenges in Linear and Nonlinear Paired-Pulse Facilitation (PPF) and Prediction Accuracy in Neuromorphic Systems

In the context of neuromorphic computing, achieving high linearity in the synaptic response—particularly during the potentiation and depression phases—is crucial for tasks like image and speech recognition, where precision is paramount. However, the inherent nonlinearity observed in many RRAM synapses poses significant challenges. Nonlinearities can distort the synaptic weight updates essential for learning and recognition, leading to decreased accuracy in these applications.[94]

Nonlinearity is a fundamental feature in many computational processes, such as the operation of logic gates and the activation functions used in neural networks (e.g., sigmoid, ReLU). Nonlinearity is crucial for enabling complex behaviors and decision-making capabilities in both biological and artificial neural networks. However, linearity is preferred in specific applications, such as certain types of analog signal processing and modeling tasks, where a predictable, proportional response is essential. This balance between linearity and nonlinearity is key to optimizing the performance of neuromorphic systems depending on the intended application.[95–97]

To enhance synaptic linearity, increasing the structural complexity of synapses is a common approach. For example, employing a one-transistor/2-resistor (1T2R) configuration has shown to improve update linearity, despite the increased area due to the additional components.[98,99] Alternatively, devices like Li-based ECRAMs or organic-based memories often feature three-terminal structures that achieve enhanced linearity in potentiation and depression processes. These configurations maintain high linearity even within a narrow conductance window, demonstrating almost linear behavior as reflected in energy efficiency and the precision of synaptic updates.

1.6.1 Complexity of Crossbar Arrays in Miniaturization

The miniaturization of crossbar arrays introduces another layer of complexity and challenges. As these arrays become smaller, maintaining performance and reliability

without increasing the complexity of the system becomes more difficult. Miniaturization often requires precise control over material properties and device architecture to prevent issues such as signal crosstalk and interference, which can degrade the array's overall functionality.[100,101]

The integration of advanced synaptic structures within a miniaturized crossbar array is crucial for enhancing the system's capability while addressing the limitations of scalability and manufacturability.[26] For instance, the implementation of complex synaptic designs, such as those involving multiple PCM devices in parallel, not only helps in increasing the dynamic range of synaptic weights but also reduces stochastic variability, which is vital for consistent performance during training phases.[102–104]

1.6.2 Addressing Prediction Accuracy and System Complexity

To tackle the issues of prediction accuracy and system complexity, several strategies have been proposed. Enhancing the granularity of conductance steps and reducing associated variability are key considerations. By structuring weight updates to diversify demands on resistive devices within different layers of the memory hierarchy, systems can balance requirements such as linearity, endurance, and retention.[45,105] This balance is crucial for optimizing performance and integration density, enabling the deployment of neuromorphic systems in practical applications.[42,106] Incorporating advanced weight structures, like differential pairs of PCM devices combined with capacitance-controlled transistors, further enhances the management of synaptic weights.[107] These structures support the use of conventional datasets for training, such as MNIST, achieving accuracy comparable to software-based approaches. This method not only addresses the challenges of prediction accuracy but also ensures that neuromorphic systems can be scaled effectively while maintaining high levels of energy efficiency.[108]

In summary, addressing the challenges are critical for advancing neuromorphic technology towards real-world applicability, ensuring that devices not only mimic the human brain's capabilities but also achieve the necessary reliability and efficiency for widespread adoption.[109]

In this thesis we see how we fabricate the neuromorphic device with the material of our choice and use the device to recognise the patterns showing its ability to meet the challenges discussed here

1.7 Scope of the Thesis

This doctoral thesis delves into the cutting-edge field of neuromorphic computing, with a particular focus on the role of Bismuth Ferrite (BFO) in the development of memristor based neuromorphic systems. The research embarked upon a comprehensive journey starting from the exploration of memory and neuromorphic systems, underpinned by the pivotal role of memristors, to the detailed investigation of BFO's unique properties and its suitability for neuromorphic applications. A significant portion of the study involves PLD deposition and analysis of BFO thin films for neuromorphic devices, focusing on replicating specific synaptic functions like synaptic plasticity. While not mimicking the full complexity of the brain, these devices serve as essential building blocks for advanced neuromorphic computing systems. The thesis also ventures into practical applications, notably pattern recognition, thereby marking its contribution to the field.

The scope of this thesis encompasses the development of a reactive PLD system, the optimization of deposition parameters for crafting high quality BFO thin films, and the in-depth analysis of their neuromorphic properties. This foundational work sets the stage for the exploration of BFO neuromorphic devices, their linearity, and the impact of oxygen vacancies on device performance. The research culminates in demonstrating the applicability of these devices in advanced computing tasks, including efficient pattern recognition using neural network models. By bridging materials science with neuromorphic engineering, this thesis outlines a forward-looking perspective on the use of BFO in neuromorphic systems, highlighting its potential to revolutionize computing and data management in an era increasingly defined by complex computational challenges.

Content of the chapters are briefly discussed here:

Chapter 1 discusses the challenges of future computing needs. It traces the development and significance of the neuromorphic systems, highlighting neuromorphic computing's evolution as a solution to the von Neumann bottleneck. The chapter underscores the importance of precise control and high-quality film deposition in

creating effective neuromorphic systems, with a special focus on Bismuth Iron Oxide (BFO) for its unique properties, laying the groundwork for exploring BFO based memristors.

Chapter 2 delves into the specifics of constructing a reactive Pulsed Laser Deposition (PLD) system for the deposition and characterization of BFO thin films. It details the operational parameters of the PLD process, emphasizing the role of the Nd: YAG laser in achieving precision. The chapter covers the calibration and control mechanisms essential for maintaining film thickness and introduces Atomic Force Microscopy (AFM) as a tool for analysing the surface quality of deposited films, setting the stage for understanding the complexities of fabricating high quality BFO films for neuromorphic applications.

Chapter 3 focuses on the deposition process of BFO thin films using PLD and their detailed characterization. It reviews the literature on BFO deposition, highlighting its importance for neuromorphic systems due to its ionic and polarization properties. The chapter explains the use of X ray photoelectron spectroscopy (XPS) and X ray diffraction (XRD) for material characterization, alongside AFM for surface analysis, providing insights into the quality and suitability of BFO films for neuromorphic computing. Chapter explores the fabrication and analysis of BFO Neuromorphic Devices, investigating their neuromorphic properties, such as response to electrical pulses and short-term plasticity (STP), which are essential for mimicking brain like functions. The chapter details the examination of key parameters like off current, duty cycle, and the impact of oxygen vacancies on device performance, contributing significantly to understanding BFO devices' potential in neuromorphic computing.

Chapter 4 examines the linearity of BFO neuromorphic devices and its implications for real world applications. It discusses the importance of device linearity in neuromorphic systems and explores methods to enhance this characteristic by manipulating oxygen vacancies. The chapter highlights the correlation between oxygen vacancies, synaptic weights, and plasticity time constants, offering insights into customizing synaptic systems for specific applications based on linearity.

Chapter 5 demonstrates the application of BFO neuromorphic devices in pattern recognition tasks, incorporating neural network models to leverage their computational efficiency. It emphasizes the use of Convolutional Neural Networks (CNNs) for their

pattern recognition capabilities and explores parallel processing to improve execution time. Through practical examples, such as handwritten digit recognition, the chapter showcases the potential of BFO devices in advanced computing applications, setting the stage for future research directions.

Chapter 6, the concluding chapter, synthesizes the journey of discovery and innovation detailed in the thesis. It revisits the development of the PLD system, the exploration of BFO materials, and their application in neuromorphic devices. Highlighting the achievements and potential future research areas, such as multilayer structure optimization and the influence of magnetic fields, this chapter reflects on the broader implications of the research and envisions a dynamic future for BFO neuromorphic devices in advancing computing technologies.

Chapter 2:

Construction of a reactive pulsed laser deposition system, deposition, and Characterization of BFO thin films

2.1. Introduction

Pulsed Laser Deposition (PLD) is a thin film deposition technique used in materials science and engineering. It works by directing a powerful pulsed laser beam at a material inside a vacuum chamber. In RPLD, high-energy laser pulses generate a plasma plume by ionizing the target material, which then deposits as a thin film on the substrate.[110,111] PLD allows precise control over factors like layer thickness, composition, and structure, thanks to its ability to adjust deposition parameters. This control, combined with the vacuum environment that prevents outside contamination, ensures the creation of high-quality, pure thin films suitable for many different uses.[112] PLD is versatile and works with a wide range of materials, from metals to ceramics. This flexibility allows for the creation of complex thin films with multiple components, layers, and structures. It's used in various fields such as electronics, optics, and energy devices, where precise thin film fabrication is crucial. Additionally, PLD can evenly deposit thin films across large surfaces, and real-time monitoring techniques help keep the process on track.[113,114] As the demand for customized thin films grows, PLD continues to play a vital role in driving innovation and developing advanced materials and technologies.[115]

This chapter describes the construction of a reactive pulsed laser deposition (RPLD) system and its calibration. Using this home-built system, thin films of Bismuth iron oxide (BFO) were deposited. The films were characterized, and the deposition process was optimized. This chapter begins with the discussion on theoretical aspects of the process of PLD, then parameters of PLD, and the essential components the pulsed laser deposition system.[110,116]

This chapter describes about the design and construction of the PLD system. While we discuss the processes, we delve into the laser's properties, such as the pulse

energy and wavelength, highlighting their roles in precise deposition control. To optimize the deposition process, we fine-tune individual parameters and establish a calibration curve based on varying deposition times while keeping other variables fixed. For the surface morphology analysis, we employ atomic force microscopy (AFM) to estimate the film roughness. Additionally, we rely on X-ray photoelectron spectroscopy (XPS) to understand the stoichiometry and X-ray diffraction (XRD) to analyse the crystallinity of the films.

This chapter concludes with the complete design and working of the PLD system and the $BiFeO_3$ films deposited using the system. These insights provide the foundation for subsequent chapters, where we explore BFO-based memristors for neuromorphic applications

2.2. Construction of the Reactive Pulsed Laser Deposition System

2.2.1 The process of pulsed laser deposition

PLD is a versatile physical vapor deposition technique, which employs a high-power laser for the ablation of the target materials, which leads to the film deposition on the desired substrates.[117] It consists mainly of a vacuum chamber with a transparent port for laser entry. The two main components inside the vacuum chamber are the target and the substrate holder. The target material and the substrate are oriented parallel, facing each other at a specific distance apart. The laser focused to the target ablates the target material creating a plasma plume, which moves normal to the surface of the target. A thin film of the target material is gradually developed on the substrate that is exposed to the plume. Substrate temperature is regulated by the substrate heater embedded in the substrate holder.

The process of pulsed laser deposition is composed of different stages.

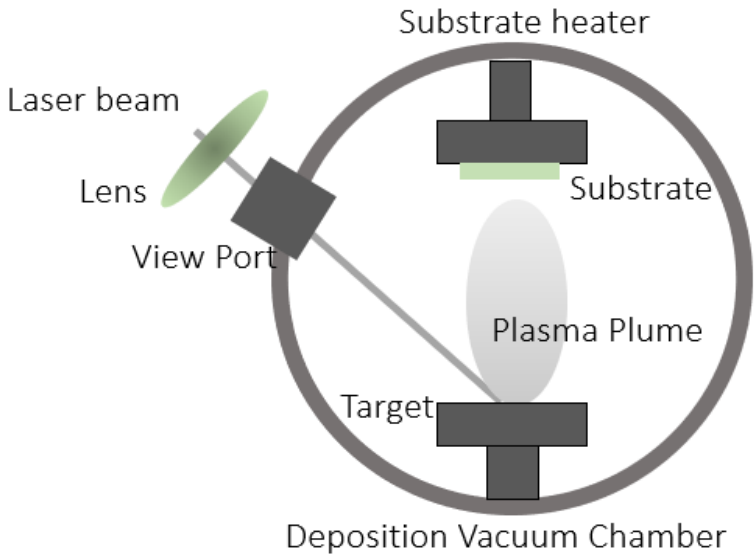

Figure 2.1 Schematics of a Pulsed Laser Deposition System

2.2.1.1 Laser ablation of target

The essential processes of a Pulsed Laser Deposition (PLD) instrument, which are critical for fabricating thin films, include laser ablation, plasma formation and its expansion, and the nucleation and growth of materials on a substrate.

Laser absorption

Ultra-short laser pulses facilitate material removal through a combination of thermal and nonthermal processes, which are not exclusively dependent on the target material's ability to absorb light.[118] At the outset, non-thermal interactions are predominant, with photons inducing electron transitions within the material. Multiphoton excitation can occur when two photons simultaneously excite a molecule within picoseconds.[119] The Beer–Lambert law is used to calculate how deeply laser light penetrates the material, which is critical for estimating non-thermal effects. For thermal interactions, processes like Pulsed Laser Deposition (PLD) involve rapid heating of localized areas, potentially causing mechanical stress and other side effects. The ejection of material is a result of both electronic and thermal ejection mechanisms, where heat-induced bond cleavage can lead to molecule desorption and fragmentation.[120]

2.2.1.2 Plasma plume dynamics

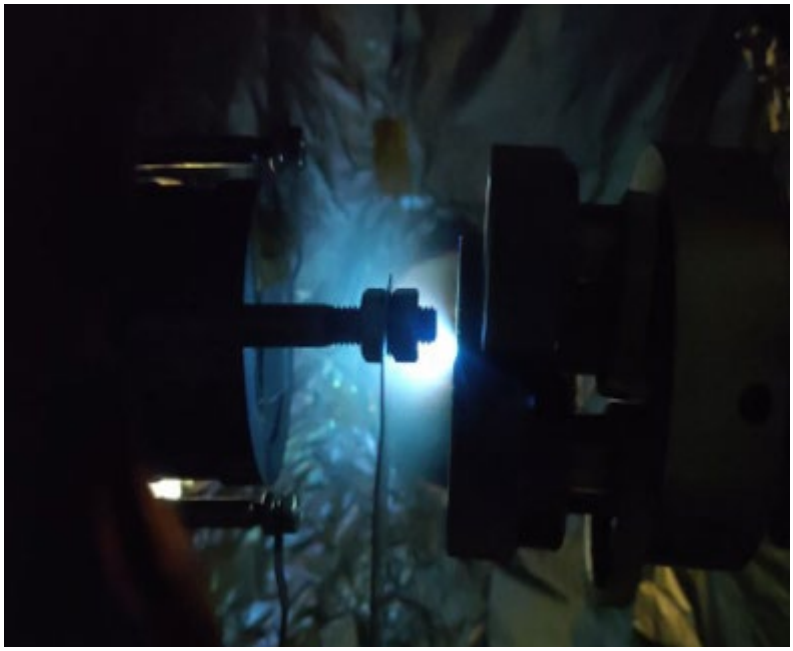

Figure 2.2 Pulsed Laser Deposition

Laser light is absorbed not just by the solid target but also by the vapor it creates, leading to complex reactions that eject electrons and energize the plasma. As the vapor gets denser, it forms a layer that propels the plasma's expansion. In the early stages of plasma formation, lighter elements and electrons race ahead while heavier one's trail behind, creating a natural sorting effect. This separation sets up an electric field that further boosts the ions, shaping how the plasma expands and what will reach the substrate forming the film.[121,122]

2.2.1.3 Film nucleation and growth

The plasma plume gets to surface of the hot substrate. The plume species get absorbed into the surface of the substrate by either physisorption or chemisorption. Low coverage of the plume results in the diffusion, where atoms hop on energetically favourable positions while the high coverage can result in chemical diffusion due to chemical interactions between the atoms. A defect free surface helps in diffusion. Cluster formation on the surface is determined by the surface tension of the clusters and the surface free energy of the substrate.[123]

In thin films, atoms aggregate via heterogeneous nucleation to a critical size before stable growth. Different growth modes depend on the binding interactions within the film as well as between the film and the substrate.

Volmer-Weber (Island Growth): Characterized by the nucleation and growth of isolated islands of material on the substrate, this mode typically results in non-uniform films with rough surfaces due to the discontinuous nature of the film formation.

Frank-van der Merwe (Layer-by-Layer Growth): This mode involves the deposition of material one atomic layer at a time, leading to the formation of smooth and continuous films. It is ideal for producing films with high uniformity and minimal surface roughness, though it may not always accommodate strain effectively.

Stranski-Krastanov (Layer-plus-Island Growth): Initially follows the layer-by-layer growth mode but transitions into island formation after a few monolayers. This mode offers a balance between achieving a smooth film surface and relieving strain within the film, making it advantageous for maintaining crystalline quality in materials that experience significant lattice mismatch with the substrate.[123,124]

In this thesis, the Stranski-Krastanov growth mode is preferred for the deposition of $BiFeO_3$ films. This mode is chosen because it effectively combines the smooth surface morphology typically achieved through layer-by-layer growth with the strain-relief benefits of island formation. This balance is crucial for maintaining the film's crystalline quality and minimizing defects that could impact the performance of neuromorphic devices.

Evidence supporting the preference for the Stranski-Krastanov growth mode is drawn from X-ray Diffraction (XRD) and Atomic Force Microscopy (AFM) analyses. XRD results indicate a high degree of crystallinity and well-defined peaks corresponding to $BiFeO_3$, suggesting that the film has maintained its structural integrity during growth. Additionally, AFM images reveal a smooth surface with occasional islands, consistent with the expected morphology of films grown via the Stranski-Krastanov mode. These observations confirm that this growth mode is the most effective for achieving the desired properties in our $BiFeO_3$ thin films.

2.2.2 Parametric influences in pulsed laser deposition

PLD is a versatile thin film deposition technique for depositing diverse materials with tailored properties. Stochiometric transfer of the material from the target to the

substrate is the key highlight. In PLD one can adjust the structure, composition, and the density of the thin film. Vapor species is dependent on different parameters. One can refer to the existing literature to start with deposition of a material initially, however, needs to optimize the parameters for different PLD systems. Main parameters to optimize include laser power, working gas environment, substrate, and target.

Table 2.1 Laser parameters and influence on the deposition

Laser Parameters	
Parameter	Significance
Wavelength	For better absorption
Fluence	High enough to sustain ablation
Pulse width	Controls the laser-target interaction time
Repetition rate	Controls the deposition rate
Spot size	Controls the uniformity of ablation and hence film
Deposition Conditions	
Background gas	Act as reactant and controls the kinetics of the ablated species.
Target substrate distance	Trade-off between thickness and span of deposition on substrate
Substrate temperature	For optimal growth conditions

2.2.2.1 Laser

The following laser parameters are discussed in detail here:

Wavelength selection

The wavelength needs to be selected properly for pulsed laser deposition. Band gap of the material determines the laser wavelength required for pulsed laser deposition. Common lasers used for PLD include, ArF, KrF, XeCl, and Nd: YAG.[125] Deposition of metals by laser ablation is inefficient because of the reflection by conduction band electrons.[126] However, oxides absorb the UV well. Laser wavelength selection hence

allows to target specific bonds in the target material. Overall plume composition and hence the film quality can be determined by the wavelength of the laser.

The decision to use an Nd laser (1064 nm) was based on its ability to match the bond energies in the $BiFeO_3$ target, allowing for controlled ablation and deposition. If a KrF excimer laser (248 nm) were used, its higher photon energy could result in more aggressive ablation, potentially increasing the deposition rate but also introducing more defects in the film. This could compromise the film quality, particularly in terms of surface smoothness and crystalline integrity. A comparison from the literature supports that while KrF lasers can increase deposition efficiency, they may also lead to higher defect densities compared to Nd lasers, which offer more controlled growth conditions.[127–129]

Here we have used UV (third harmonics of Nd: YAG laser with wavelength 355 nm) for laser ablation of the Bismuth iron oxide target.

Pulse width and pulse energy.

In PLD, laser-target interactions are crucial in early stages of material ejections. Pulse energy density controls the plume ejection efficiency which in turn is determined by pulse width and energy of the laser pulse.[120] Ejection and plasma formation happens at an order of picoseconds. Femto-second pulses generate high electron densities, while nanosecond ablation is suitable for depositing complex films due to monoatomic species formation. Ablation threshold determines if the removal of a material is predominantly thermal or non-thermal.[130] In our experiments case, laser with pulse width of 8ns was used and the energy density of the beam was 4 J/cm^2.

Spot size

The laser beam is focussed using a lens, effectively reducing the area of the beam to a spot. The size of the spot determines the plume size and material characteristics of the hence deposited thin film.[131] Intense plasma created by focussed laser affects the removal of the particles. The energy density of the laser determines the ablation of the target, which will be very high upon focusing.[120]

We have focussed the laser beam to a spot size of 1 mm^2, and all the deposition of the BFO films are done at an area energy density of 4 J/cm^2.

2.2.2.2 Gaseous environment

Inter-particle collisions happen as the ablated particles travel from target to substrate within the plasma plume. They occur at the plume's contact front with the surrounding gas and near the substrate surface. Usage of the background gas during deposition allows controlling film composition and reduce particle energy. Several factors like gas pressure and reactivity impact the extent of the collision and chemical reactions during travel, affecting the formation and thus the properties of the films.

The vacuum chamber is initially evacuated and then the background gas is filled to provide the deposition atmosphere. Initial vacuum is set to 10^{-6} mBar and with background gas filled to chamber, the working pressure becomes 10^{-2} mBar. The atmosphere inside the vacuum chamber affects the ions in the plasma plume that is ejected towards the substrate. The energy of the ions reaching the substrate surface hence is affected by the background gas. With the use of background gas one can add elements to contribute to the thin film deposition as, usage of oxygen as background gas will ensure oxygen in thin films. Hence, oxygen hence is while depositing the oxide thin films. Gas type as well as the pressure while deposition causes its effect in the film properties like crystallinity as well as the film thickness. [132] In this pulsed laser deposition system, we have used oxygen when depositing bismuth iron oxide as to ensure the proper incorporation of the oxygen element to the BFO thin films.

Pressure of the background gas plays important role in plasma kinetics and hence do control the collision of the particles to the surface of the substrate.[133] Usage of a reactive gas like oxygen will also influence the elemental composition of the depositing thin film. During the deposition there exists three different pressure regions inside the vacuum chamber. These are 1) low pressure regime 2) transition regime and 3) diffusion like regime. In low pressure regime, there exists the minimal gas interaction, resulting in comparatively thicker film. In transition regime, plume interacts with the gas resulting in the variation in the elements across the film. This happens on a range of 10^{-3} to 10^{-2} mBar. Diffusion like region happens in the range of 10^{-2} to 1 mBar. This is where the species gets slow down, and the film get even distribution. While deposition of the BFO thin films, we have kept the pressure around 3×10^{-1} mBar and are giving uniform even films over an area of 1 $inch^2$.

2.2.2.3 Substrate

From the plume generated by the laser, the thin films grow on the substrate. The substate will be already in an elevated temperature to ensure the proper diffusion and reaction of the atomic species. The ionic species arriving at the substrate surface diffuse and reacted with each other to form the film. This results in the layer-by-layer growth of the thin film on substrate surface. Highly ordered monolayers need high diffusion. Also, the substrates lattice compatibility is essential for better nucleation of the film to the surface. High temperature depositions usually result in better crystalline thin films. Optimal temperatures are crucial for the optimal deposition of the thin films. The crystallinity of the film is affected by the substate temperature, is a common observation. Also, the substrate needs to be chosen as it affects the strain/ defects develops in the film during the growth. Surface stability will be determined by this factor. And finally, the choice of substrate dependents on the type of measurements or the structure of the device to be fabricated.

We have used Fluorine doped tin oxide (FTO)coated glass as the substrate. The main reason for selecting FTO is that it is a highly conducting material with high-temperature stability, and it is a standard substrate for device fabrication. The substrate temperature of the deposition was deliberately brought down to comparatively lower temperatures of 400^{o} C, to make sure that the process temperature is in range of existing CMOS processes, because finally, these neuromorphic devices will have to be integrated to the existing CMOS technology.

2.2.2.4 Target

Pulsed Laser Deposition (PLD) being the technique that enables the transfer of complex stoichiometries from a target to a substrate, with the target's composition being critical for the stoichiometry of the resulting thin films. However, there are challenges in achieving the desired compositions due to the material's properties and atomic composition. The physical properties of the target such as its crystallinity and density are also key to producing high-quality films.

Material and composition

The composition of a thin film may not always be the same as in the target, but variations are possible in the exact composition and stoichiometry. Lighter elements are prone to scattering, leading to their faster depletion from the substrate. The difference

in atomic mass can cause more pronounced compositional deviations. The stoichiometry of the film is also affected by the volatility of the elements, which tends to reduce the presence of light or volatile elements. To counter these issues, deposition parameters can be adjusted to ensure the film composition aligns with the target. The energy required for ablation is determined by the target material's band gap, dictating the laser wavelength used. However, using high laser fluence can lead to droplet formation on metallic targets, which compromises the quality of the film. Finally, the composition of both the target and the film can evolve during the deposition process because of melting and vaporization.

Surface quality

Target density dictates the thin film characteristics and finish quality. For optimal deposition in PLD, material density must exceed 90%. Ablation causes surface degradation and thus the plume features as well, which eventually alters the film content and uniformity. Clean surfaces require pre-ablation polishing. Bidirectional ablation lessens particulate directionality. Secure storage and target pre-ablation preserve optical traits.

Target to substrate distance

In PLD deposition, the ablated material is mostly confined within a 30° range in the solid angle of the plume. The distance from the target to the substrate dictates the angle and density of the plume, influencing film thickness and composition. Larger distances yield thinner films; conversely, shorter distances amplify species rebound due to high kinetic energies. Interactions between plume species and background gases are critical for the distribution of the elements in the film, particularly below the mean free path distance and with reactive gases.

2.2.3 Components and design of the PLD System

In this section, we are examining the components of the PLD system individually. All these components have been customized to work together for the development of the PLD system. With the PLD process in mind, we have designed, modified, and integrated these components.

Figure 2.3 PLD System

2.2.3.1 Laser:

One of the essential components of a Pulsed Laser Deposition System is the laser. Solid state lasers are usually preferred with the PLD systems. Primarily the lasers are chosen depending on the wavelength, suitable for a particular choice of material ablation. Pulse length can affect the ablation and film growth. In this PLD, we used 355 nm wavelength laser, which is the third harmonic of ns and an Nd: YAG solid state laser. The pulse width and repetition rate of the pulses were 8 ns and 10 Hz respectively.

2.2.3.2 Vacuum chamber:

A high vacuum is required in the deposition chamber to control the behavior of particles and plasmas. The rate at which particles deposit on surfaces and the mean free path—the average distance particles travel before colliding—can be calculated with specific equations. As the pressure decreases, particle deposition slows down, and that mean free path increases, significantly influencing the plasma's activity within the chamber.

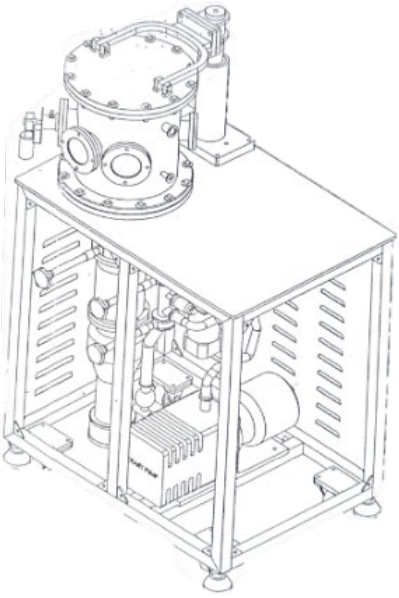

Figure 2.4 Deposition system

The vacuum chamber diameter was 30 cm and height were 40 cm. There were two vacuum pumps to facilitate the evacuation process. The rotary vane pump was used to take the internal pressure close to 0.01mBar and then the high vacuum pump takes the pressure to 10^{-5} mBar. We employed the diffusion pump as the high vacuum pump.

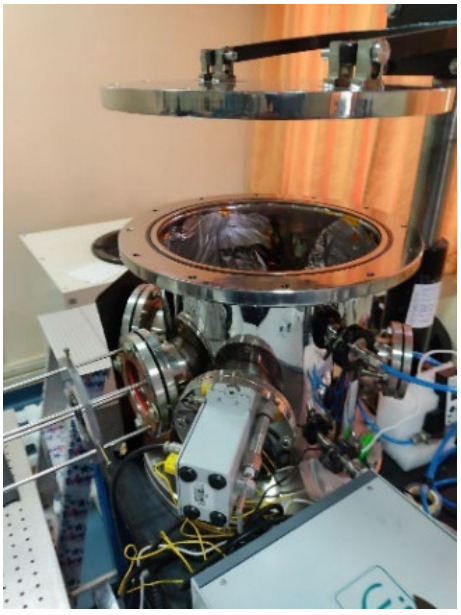

Figure 2.5 Deposition chamber

After reaching the high vacuum, we allow a regulated flow of working gas inside the chamber at a required pressure by letting the gas through a Mass flow controller. Ones the required pressure is reached, the deposition can be done.

2.2.3.3 Target holder.

Ablation experiments utilize targets that are typically rod-shaped or disk-shaped, each with distinct advantages. To prevent surface cratering, the target's position must be continually adjusted during the laser ablation process. Rod-shaped targets are mechanically simpler and allow for the construction of layered structures, yet they demand precise alignment to ensure consistent ablation. On the other hand, disk-shaped targets are more straightforward to manufacture and feature customizable movements that facilitate even ablation across the target surface. We are using disk shaped targets with a diameter of 1 inch, 0.25-inch thickness in this PLD system. The BFO targets are 99.9% pure and are bought from ACI Alloys, Inc. (SanJose, USA). The target is set to rotate while deposition to ensure uniformity in target consumption. We designed the target carousal and finally realized it resourcing it externally to integrate with the deposition chamber.[112]

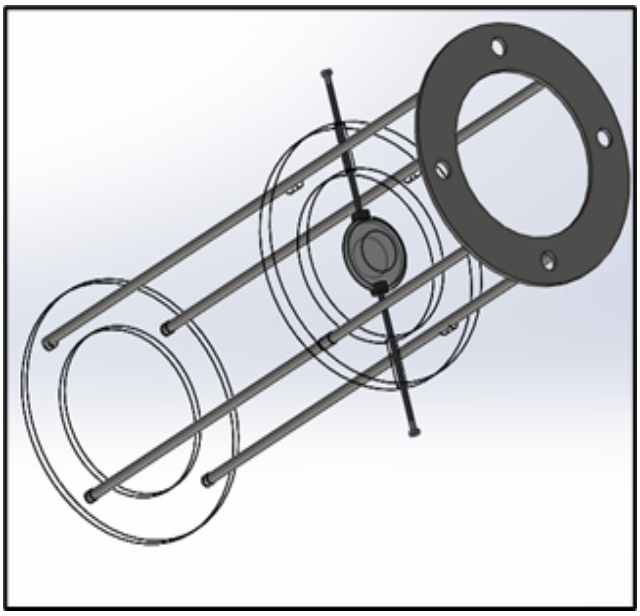

Figure 2.6 Lens adjuster designed

Figure 2.6 shows the design of a crucial component, the lens adjuster, which plays a pivotal role in focussing the laser beam to the target. Figure 2.7 highlights the successful integration of this lens adjuster into the system. In Figure 2.8, we see a substrate holder equipped with a heater, ensuring precise temperature control during experiments. Lastly, Figure 2.9 presents a multi-target carrousel, a key element that efficiently manages and selects multiple targets within the system, for various experiments and applications. The target holders were specifically designed for one-

inch diameter targets. The chosen target is positioned in front of the laser to intercept the laser beam and create the plume.

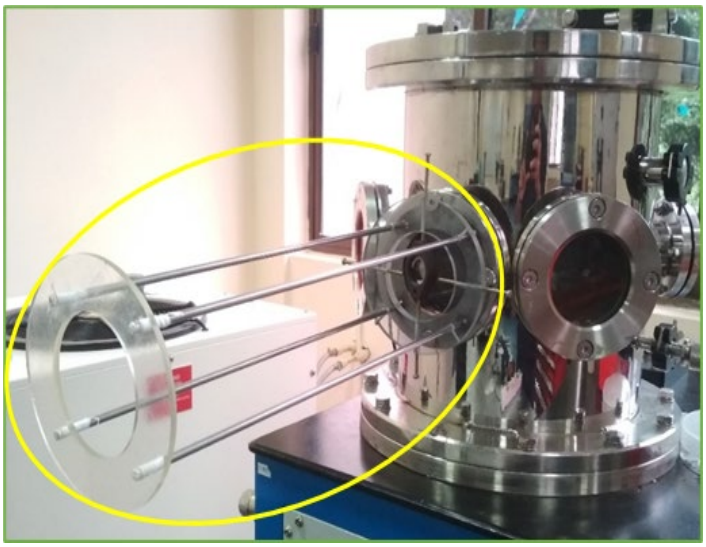

Figure 2.7 Lens adjuster integrated into the system

2.2.3.4 Heater and substrate holder.

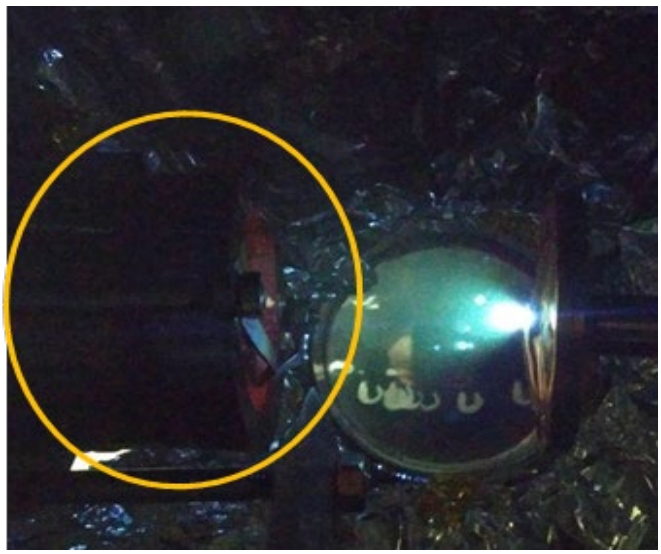

Figure 2.8 Substrate holder with Heater

.

The growth of crystalline materials requires high substrate temperatures, which is achievable by resistive or laser-based heaters that can reach up to 1000°C. The geometry of these heaters influences the volume of the chamber that is heated and the density of the plasma, which in turn affects the growth of the material. Here we have the heater which can go up to 1000° C, however for the deposition we have used a

substrate temperature of 400° C to make sure that the process is compatible with the existing CMOS technology.

Figure 2.9 The multi-target Carrousel

Heater and substrate holder is designed according to the chamber and specifications are made to sure that the heater goes over 1000º C for most of the PLD depositions. Finally, then realized using a company to later be integrated to the deposition chamber.

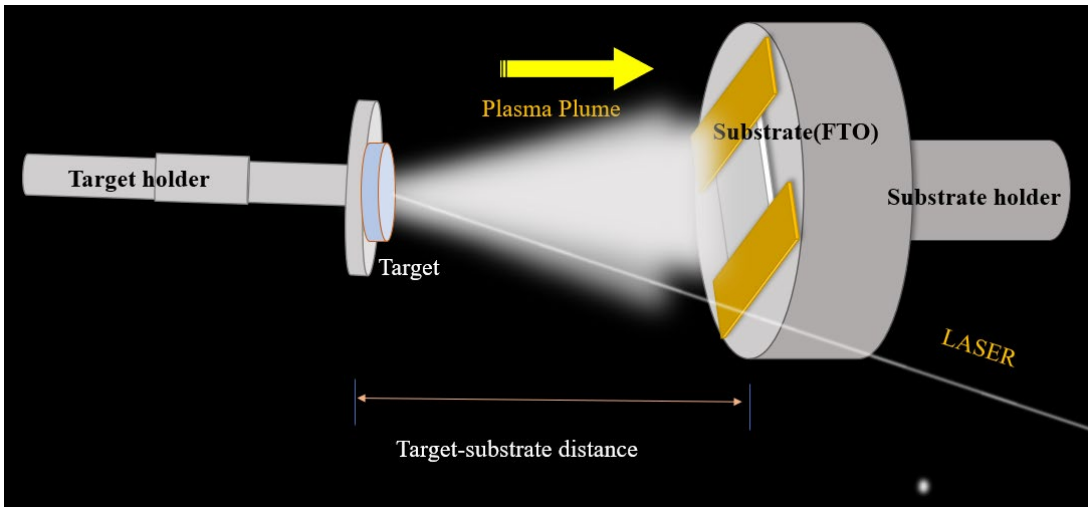

Figure 2.10 A pictorial representation of plume ablation when laser pulses strike the target

Figure 2.10 illustrates the plume ablation phenomenon generated by laser pulses impacting the target. In Figure 2.11 captures the photograph of the deposition.

Figure 2.11 Photograph of the plume

2.3. Deposition of BFO Thin Films

We have developed the reactive pulsed laser deposition system. Having many parameters influence in deposition, it is crucial to optimize the parameters to have a controlled thin film deposition. After going through many iterations of varied parameters we arrived at the following optimised parameters values. We can have different thickness of the BFO film by changing the duration of deposition.

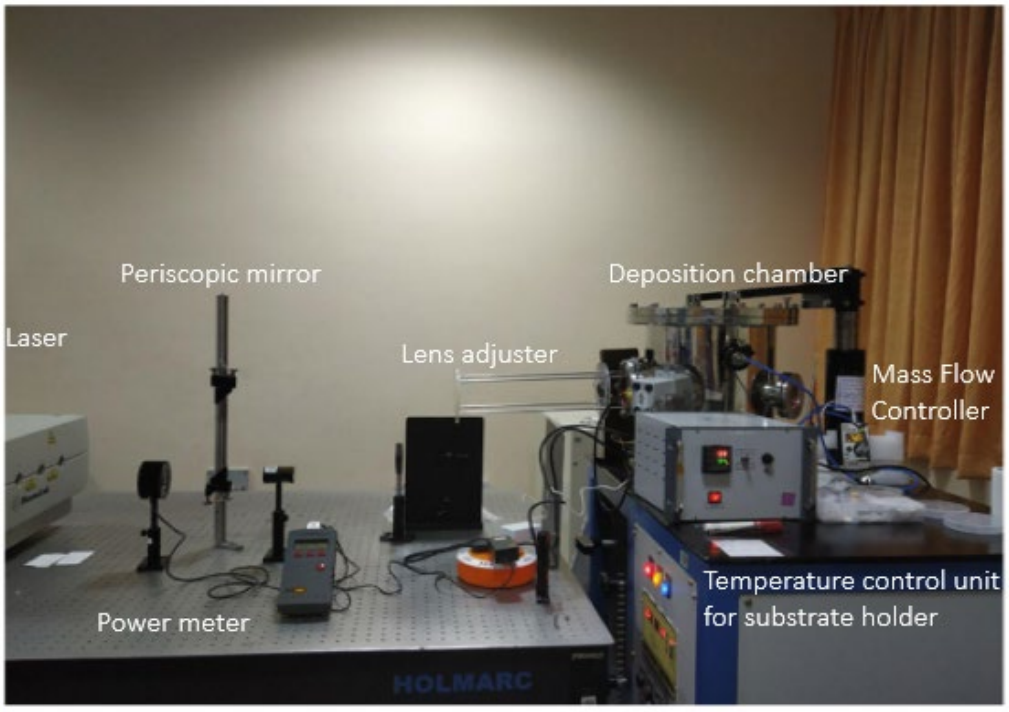

Figure 2.8 Reactive Pulsed Laser Deposition System

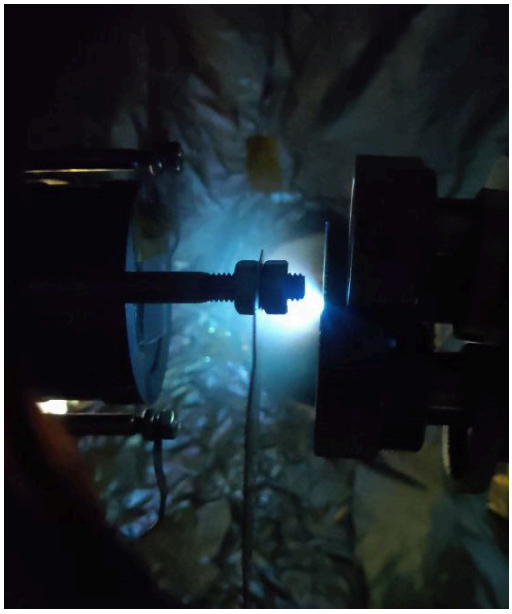

Figure 2.13 Deposition

Figure 2.12 illustrates the setup of the Reactive Pulsed Laser Deposition System used for the deposition process. In Figure 2.13, we present a photograph of the actual deposition process itself.

Table 2.2 Deposition parameters

Laser Parameters		
1	Wavelength	355 nm
2	Fluence	4 J/cm^2
3	Pulse width	8 ns
4	Repetition rate	10 Hz
5	Spot size	1 mm^2
Vacuum Parameters		
6	Base pressure	10^{-5} mBar
7	Target- Substrate distance	40 mm
8	Substrate temperature	400 C

Table 2.2 presents the deposition parameters used in our study. The laser parameters included a wavelength of 355 nm, fluence of 4 J/cm², pulse width of 8 ns, repetition rate of 10 Hz, and a spot size of 1 mm². In the vacuum chamber, the base

pressure was 10^{-5} mBar, however, later get filled with gas to a deposition pressure of 0.3 mBar, with a target-substrate distance of 40 mm and a substrate temperature of 400°C.

We have deposited multiple BFO thin films with different deposition duration such as 2, 5, 10, 20, and 40 minutes to get different thickness. A step-profile was made in the film to measure the film thickness for this variation in deposition duration. Analysis of multiple measurements gave us the calibration curve, shown in figure 2.14. We estimated the rate of deposition of the deposition for particular set of parameters and duration of deposition hence can be decided for a desired thickness of BFO film.

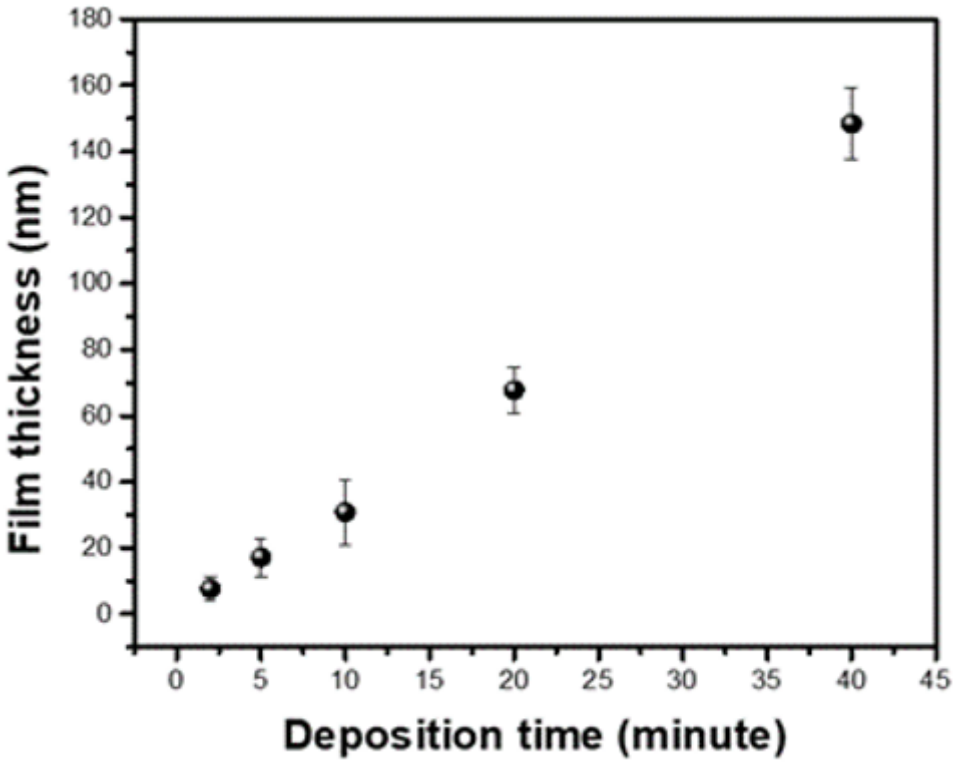

Figure 2.14 The calibration curve of BFO deposition for the other parameters remains constant

To establish a calibration curve, we maintained all other parameters constant while varying the deposition time. This allowed us to correlate deposition duration with thickness accurately. Our analysis revealed that the deposition rate was approximately **3.5 nm** per minute, which enables us to estimate the film's thickness at specific deposition durations with precision.

2.4. Characterization of BFO Thin Films

The films' material characteristics have undergone a comprehensive examination to assess their suitability for use in the development of neuromorphic devices. This detailed analysis involved the application of various techniques.

Firstly, Atomic Force Microscopy (AFM) was employed using instruments such as Naio Nanosurf AFM. AFM allowed us to explore the surface morphology of the films and obtain precise measurements of their thickness. These insights are crucial in understanding the physical properties of the material. Secondly, X-ray Diffraction (XRD) was conducted using the advanced Bruker D8 ADVANCE Diffractometer. This technique provided a thorough investigation of the films' structural characteristics. By analysing diffraction patterns, we gained valuable information about the crystalline phases and grain orientation within the material. Lastly, X-ray Photoelectron Spectroscopy (XPS) was utilized with the Thermo Scientific ESCALAB instrument. XPS played a significant role in the analysis of the film's chemical composition and elemental properties. This technique allowed us to identify the types of atoms present and the nature of their chemical bonds.

2.4.1 Atomic Force Microscopy (AFM)

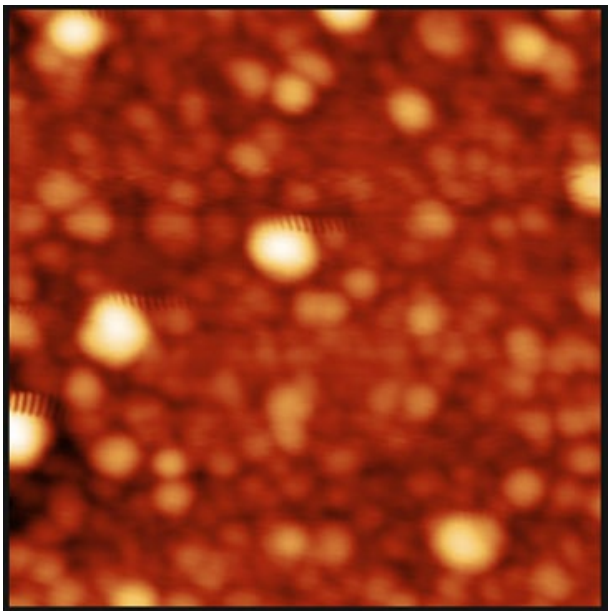

Figure 2.15 The surface morphology of the films was studied by AFM operating in the tapping mode (NaioAFM, Nanosurf)

We examined the surface structure of the films using Atomic Force Microscopy (AFM) with a specific technique called tapping mode. This was done using the Naio

Nanosurf AFM instrument. In the provided figure 2.15, you can see the AFM topography image of the film, which gives us a visual representation of its surface.

To quantify the surface roughness of the films, we calculated the root-mean-square (RMS) roughness, which turned out to be approximately 4.38 nanometers with a small margin of error, around ± 0.1 nm. This measurement helps us understand the surface roughness variation of the film's surface. The result ensures that the film is apt for device fabrication purposes. Additionally, we used AFM to estimate the thickness of the film. By analysing the height profile of the film obtained from the AFM data, we determined that the film's thickness is approximately 71± 5 nm. This information is crucial in characterizing the film's physical properties and understanding its dimensions.

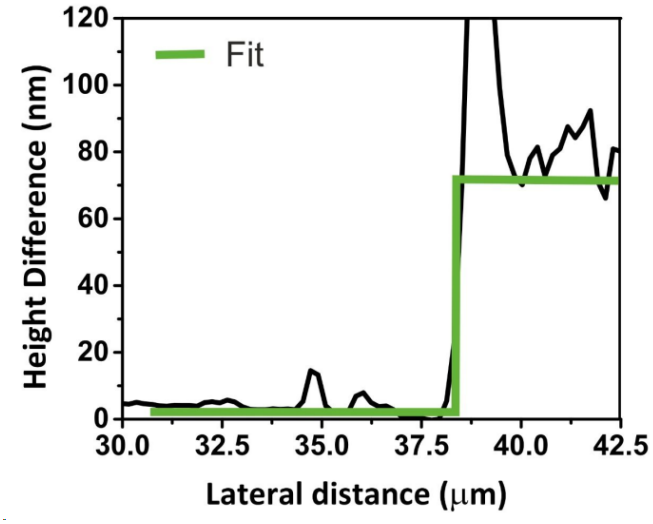

Figure 2. 16 Height profile of the film measured with AFM.

2.4.2 X-ray photoelectron Spectroscopy (XPS)

We utilized X-ray electron spectroscopy (XPS) as a powerful analytical tool to investigate the elemental composition of the film. XPS proves to be the optimal choice for comprehending the film's composition, enabling us to scrutinize both the broad and narrow spectra of its constituent elements. Our analysis encompassed the examination of the broad XPS spectra, and the subsequent narrow scans dedicated to the elements Bi, Fe, and O. To establish the chemical states of each element, we set a carbon peak at 284.83 eV as our reference point.[134]

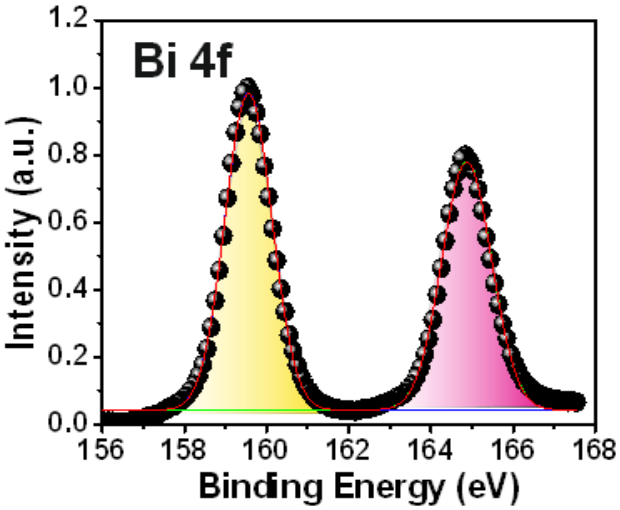

Figure 2.17 XPS analysis of the sample showing the spectra of Bi–4f,

The narrow-scan XPS spectra of Bi 4f, Fe 2p, and O 1s are depicted in Figure 2.17-2.19, respectively. Notably, the characteristic peak profiles in Figure 2.17 indicate that the bismuth within the film exists primarily in the Bi 3+ valence state. Additionally, the difference between the bismuth 4f states' peaks, amounting to 5.3 eV, corresponds to the 4f5/2 and 4f7/2 states of Bi in its oxide phase,[135] with a slight shift of approximately 2 eV observed.

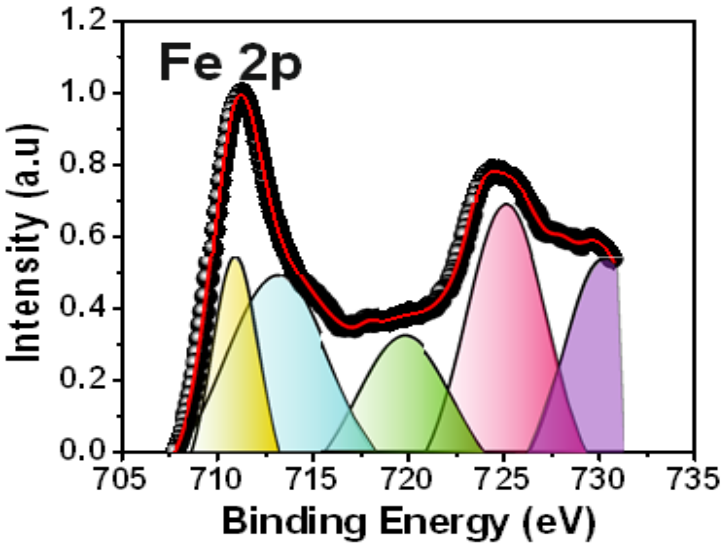

Figure 2.18 XPS analysis of the sample showing the spectra of Fe–2p

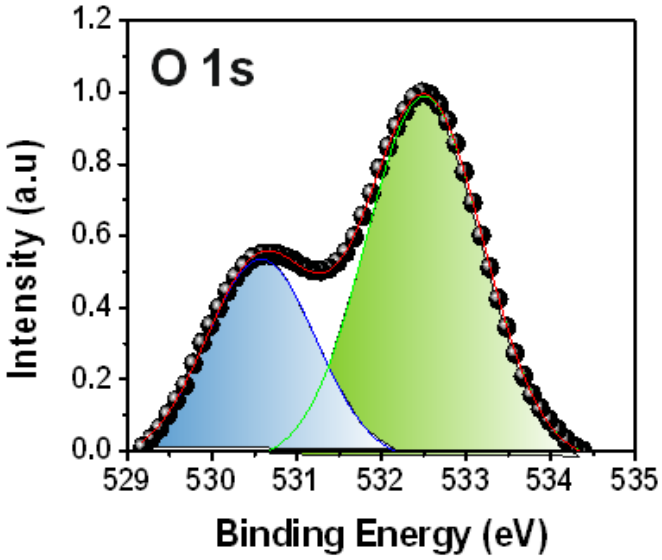

Figure 2.19 XPS analysis of the sample showing the spectra of O–1s.

Further evidence for the iron's valence state is revealed by satellite peaks, situated approximately 8 eV above the 711-eV peak, confirming the prevalence of Fe 3+ in the film[136]. We observe that the peaks for both bismuth and iron exhibit shift towards higher binding energies, which we attribute to the formation of oxygen vacancies. It has been documented that the creation of oxygen vacancies leads to an increase in the equilibrium electron density within the system,[137] consequently raising the binding energy of the elements. The existence of oxygen vacancies is discerned by examining the ratio of the areas under the curve of the dangling bond to the adsorbed oxygen in the O 1s spectrum.[138] In the context of perovskite oxides, this ratio is estimated to be 1.95. XPS analysis revealed a Bi ratio of 1:1. The oxygen content appeared higher due to the presence of adsorbed oxygen. By isolating the contributions of adsorbed and lattice oxygen, we determined the film composition to be $BiFeO_{2.9-3}$, accounting for the presence of oxygen vacancies.

2.4.3 X-ray diffraction (XRD)

To understand the structural characteristics of the thin film, we carried out X-ray diffraction (XRD) analysis. The XRD pattern of the BFO thin films deposited using the Pulsed Laser Deposition (PLD) method was obtained using the Cu Kα line with a wavelength of 1.54 Å. In the resulting XRD spectrum, a prominent peak at 32.5° dominates.[139,140] This peak corresponds to the (110) plane of the rhombohedral distorted perovskite structure, characterized by a space group of R3c (JCPDS 72-2035).

Importantly, this finding suggests the presence of a single-phase structure, with no detectable secondary phases. Additionally, we observe minor diffraction peaks indicating the (200) and (210) planes.

The figure 2.21 represents the molecular structure of bismuth iron oxide (BFO) using BURAI software. Simulating the rhombohedral perovskite structure within the software, we observed that the XRD simulation yielded a dominant peak at approximately 32 degrees.

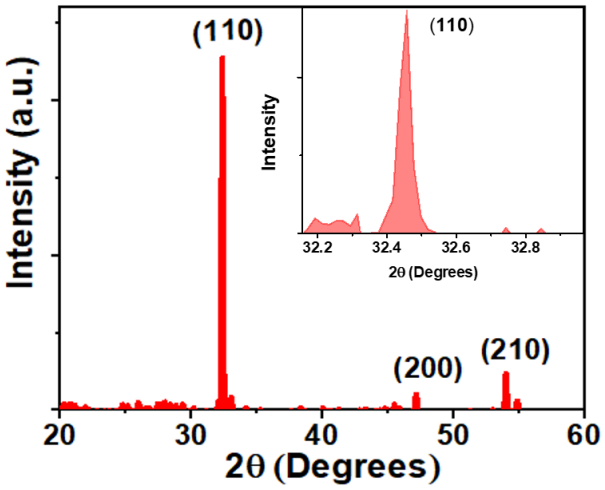

Figure 2.20 XRD pattern of BFO film

One can calculate the average crystallite size (**D**) in the direction of diffraction using the Scherrer equation [141] with the given values: $2\theta = 32.5°$, FWHM of the peak (β) = 0.0339 radians, Wavelength of X-ray (λ)= 1.542 Å (angstroms) and Scherrer constant (**K**) = 0.9

Using the Scherrer equation:

$$D = \frac{K\lambda}{\beta \cos(\theta)}$$

Now, calculating D, we get around 42.4 Å.

So, the average crystallite size D in the direction of diffraction is calculated to be approximately 42.4 angstroms. Remarkably, this estimation aligns well with the grain size we observed during our atomic force microscopy analysis. This convergence underscores the consistency of our findings across different analytical techniques.

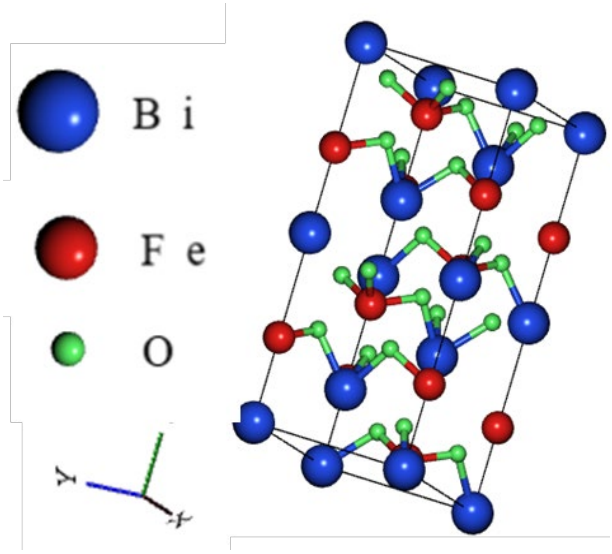

Figure 2.21 Rhombohedral distorted perovskite structure - software: BURAI.

2.5. Conclusions

PLD is a versatile technique that allows for precise control during thin film deposition, maintaining target stoichiometry. This chapter extensively details the establishment of a reactive pulsed laser deposition system for Bismuth Ferrite (BFO) thin film deposition, emphasizing thorough parameter optimization for efficient, high-quality film production. We commenced by introducing the deposition method, delving into the theoretical aspects, and exploring the factors influencing PLD. Subsequently, we discussed the design and construction of the PLD system, highlighting its tailored components.

With the developed system, we conducted depositions to optimize parameters, achieving good-quality films. We determined a deposition rate of 3.5 nm per minute for fixed parameters and conducted extensive film quality analyses using AFM, XRD, and XPS methods, revealing a roughness of approximately 4.38 nm and a thickness of roughly 71 nm for 20 minutes of deposition. The XRD spectrum indicated a single-phase (110) rhombohedral perovskite structure without secondary phases, confirming the film's composition as $BiFeO_3$.

Having successfully deposited high-quality BFO thin films using the self-built reactive PLD system, we proceeded to employ these films in the fabrication of BFO neuromorphic devices in the subsequent chapters.

Chapter 3:

Fabrication and Characterization of a BFO Neuromorphic Device

3.1. Introduction

The development and progression of neuromorphic technology find their roots in the intricate functionalities of synaptic networks inherent to biological neural networks. These networks exhibit a remarkable capability for the parallel processing of numerous information streams concurrently.[13,142] Such an ability, when translated into electronic systems, presents unprecedented opportunities to navigate and potentially circumvent the limitations imposed by the von Neumann architecture that characterizes contemporary computing systems.[4,143] The fundamental inspiration behind this technological evolution stems from the human brain's complex structure, comprising approximately 10 billion neurons interconnected by around 100 trillion synaptic connections.[14,144] This intricate network facilitates the simultaneous processing of information, with the energy efficiency of processing a single bit of information in the brain being significantly superior to its electronic counterpart—about 10 femtojoules in the brain versus 10 picojoules in electronic circuits.[44,45]

Recent scholarly investigations have illuminated the capacity of a single synaptic terminal to store information up to 4.7 bits. This discovery extrapolates to an astounding capacity for information transmission across the brain, reaching volumes of one petabyte per second. Such insights advocate for the integration of neuromorphic engineering principles into modern information technology systems. By doing so, we stand on the cusp of achieving parallel processing capabilities with minimal energy requirements.[12] Additionally, the potential for miniaturization inherent in electronic systems promises significantly enhanced 'neural' densities, offering speeds that far surpass biological counterparts. Recent advancements have seen the implementation of two-terminal capacitor-like devices and three-terminal transistor configurations in crafting artificial neural network circuits.[33,51,52] These developments have paved the way for realizing arrays of neural devices, with several applications in artificial intelligence already coming to fruition.

Delving into the biological paradigms that inspire these technological advancements, we observe that communication within real biological neurons is facilitated through synapses, which serve as bridges between neurons.[22] These synaptic connections involve a complex process whereby an action potential in one neuron triggers the release of neurotransmitters, which then bind to receptors in a neighbouring neuron, prompting the transmission of the signal. Emulating this biological phenomenon, simple electronic synapses are conceptualized as capacitors, with electrodes representing the pre and postsynaptic terminals separated by a dielectric material acting as the synaptic cleft.[45,51,70] Among the neuromorphic devices, two-terminal memristors stand out as particularly effective analogues for artificial synapses.

Neuromorphic devices are characterized by their response to voltage pulse inputs, mirroring the action potentials in biological neurons. The memory response of these devices, differentiated into short-term and long-term plasticity, is critical for mimicking the adaptive learning and memory retention capabilities of biological systems.[145–147] The exploration of various materials and configurations for neuromorphic devices has led to significant discoveries and innovations, particularly in the development of memristive devices that offer simpler fabrication processes and mechanisms.[63,65,67] A noteworthy contribution to this field is the development of $BiFeO_3$ (BFO)-based thin electronic synapses, which exhibit high reproducibility, synaptic responses, and linearity essential for neuromorphic applications.[53,81,82] The BFO thin films, prepared via pulsed laser deposition on fluorine-doped tin oxide glass, demonstrate promising neuromorphic functions such as long-term potentiation and depression, standing out for their linear response to voltage pulses—a critical feature for their integration into functional circuits.[80]

In summary, the journey towards neuromorphic technology is marked by an interdisciplinary effort to replicate the unparalleled efficiency and parallel processing capabilities of biological neural networks in electronic systems. Through the development of novel materials and device configurations, this field promises to revolutionize our computational capabilities, paving the way for more efficient, scalable, and intelligent computing architectures.[44,144,145]

In Chapter 2, the details of the construction and optimization of the Pulsed Laser Deposition (PLD) system and the deposition of the Bismuth Ferrite $BiFeO_3$ (BFO) were

discussed in detail. This Chapter is an exploration of (BFO) Neuromorphic Devices, which represent a promising avenue in the field of neuromorphic computing due to their unique properties that emulate certain aspects of the human brain. This chapter delves into the fabrication processes and conducts an in-depth study of BFO Neuromorphic devices, unravelling their distinct characteristics.

The investigation commences with a meticulous examination of how BFO devices respond to electrical pulses, revealing the remarkable neuromorphic properties that set them apart from other materials. This distinctive behavior underscores the potential utility of BFO in neuromorphic computing, as it offers a platform for mimicking neural processing within artificial systems.

To gain deeper insights into the neuromorphic properties of these devices, a detailed analysis of parameters such as off-current, duty cycle, and paired pulse facilitation is conducted.[33] This analysis not only elucidates the nuances of BFO device behavior but also paves the way for fine-tuning their performance to cater to specific neuromorphic applications. The meticulous examination of these parameters enhances our understanding of how BFO devices can be harnessed effectively within neuromorphic systems.

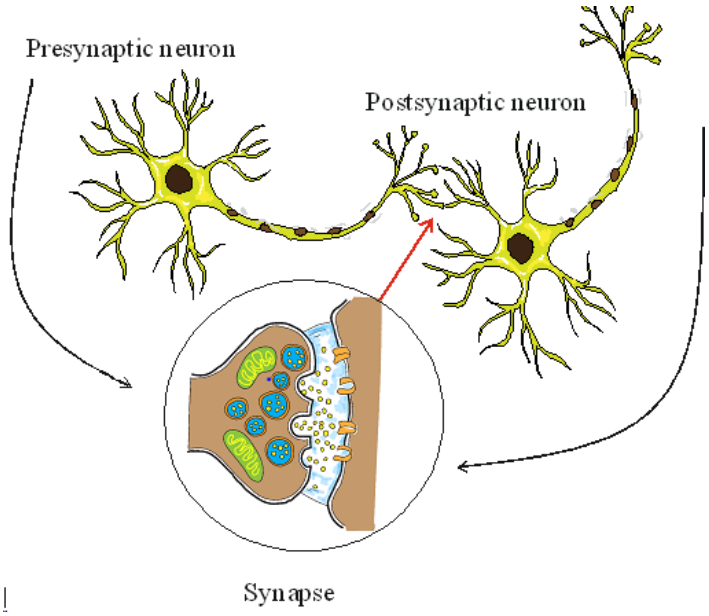

Figure 3.1 Representation of a biological synapse

An important aspect of this chapter is the investigation into spike timing dependent plasticity (STDP) in BFO devices, a fundamental concept in neuromorphic systems that elucidate the type of plasticity associated with the devices. STDP governs

the strength of synaptic connections based on the timing of neural signals, a mechanism that plays a crucial role in learning and memory processes. Understanding the STDP characteristics of BFO devices sheds light on their adaptability and dynamic behavior. The findings regarding STDP within BFO devices contribute significantly to the broader understanding of neuromorphic computing and offer valuable insights for future advancements in the field.[37,38]

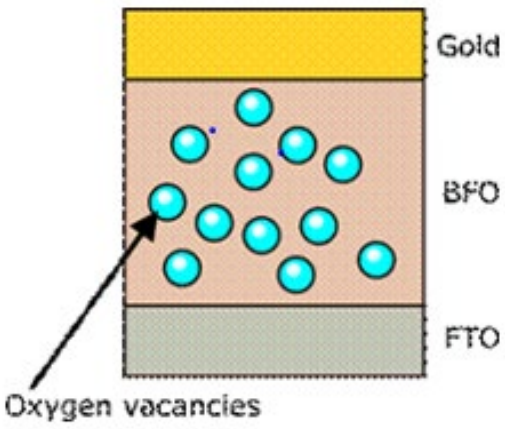

Figure 3.2 Sketch of the neuromorphic device with BFO layer sandwiched between the top layer (Gold) and Bottom layer (FTO)

In the biological neurons, communication takes place through synapses, which are the connecting links between two neurons. A synapse is a junction between two neurons, where the presynaptic neuron releases neurotransmitters that influence the activity of the postsynaptic neuron. When an action potential arrives at the neurons through the dendrites, it triggers the release of neurotransmitters from synaptic vesicles of the pre-synapse into the synaptic cleft. These neurotransmitters then bind to specific receptors on the postsynaptic neuron, potentially initiating an action potential in the postsynaptic neuron, facilitating signal transmission between neurons. This electrical signal in the postsynaptic neuron is known as the excitatory postsynaptic current (EPSC).[16,22]

To emulate this synaptic behavior in neuromorphic devices, a simple electronic synapse model is proposed. In this model, one electrode represents the presynapse, the other electrode acts as the post synapse, and the medium between them mimics the synaptic cleft. Typically, a dielectric material is used as the synaptic medium that emulates the synaptic behavior of biological neurons.

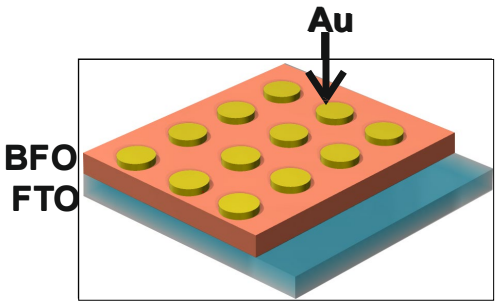

Figure 3.3 An array of neuromorphic devices fabricated for testing

The film has a thickness of 70 nm, with gold contacts measuring 1 mm² in area and 150 nm in thickness. Within this framework, two-terminal memristors emerge as excellent candidates for artificial synapses due to their ability to modulate electric current responses in response to voltage pulse inputs with specific duty cycles or frequencies.

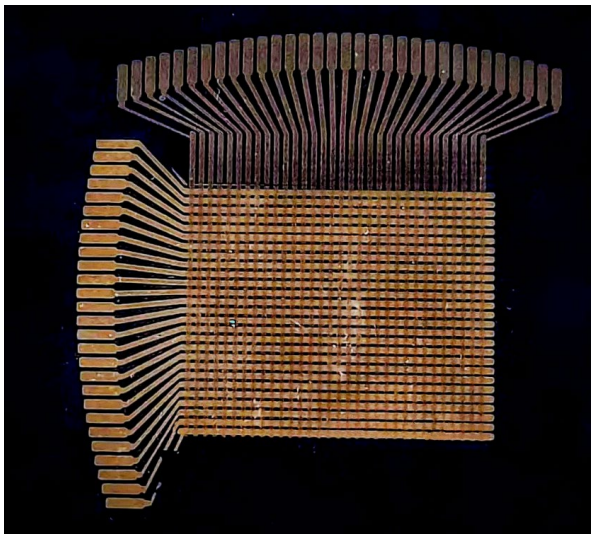

Figure 3.4 An array of neuromorphic devices fabricated in crossbar architecture

The foundation laid in this chapter, both in terms of understanding BFO neuromorphic devices and the emulation of synaptic behavior, sets the stage for the practical implementation of artificial neural networks and neuromorphic systems in the subsequent chapters of this thesis. The response of neuromorphic devices to external voltage triggers bears a striking resemblance to the way biological neurons react to action potentials. These voltage pulses effectively mimic the action potentials elicited within the complex neural networks of biological systems. Depending on the speed at which the neuromorphic system responds to input signals and the duration for which it

retains the information, the memory response can be classified into two distinct categories: short-term plasticity (STP) and long-term plasticity (LTP).[27,148] An important parameter for quantifying the performance of neuromorphic devices is the variation in the output function in response to successive action potentials, a phenomenon known as paired-pulse facilitation (PPF).

In neuromorphic engineering, researchers have explored various materials and their combinations for the development of two-terminal neuromorphic devices. These materials encompass a wide range, including two-dimensional materials, perovskites, and both doped and undoped metal oxides and semiconductors. Within this landscape of materials and device configurations, the focus of much research has gravitated towards two-terminal memristive devices as the preferred electronic element for numerous applications. These devices offer simplicity in fabrication and exhibit relatively straightforward mechanisms underlying their neuromorphic characteristics.

The core mechanisms in two-terminal memristive systems often involve partial conductive filament formation, oxygen vacancy migration, charge trapping, or interface modulation.[24,25,149] However, the inherent variability in these transport mechanisms can result in cycle-to-cycle variations due to their uncontrollable nature. Thus, the quest for materials that reliably retain neuromorphic responses remains a fundamental issue in constructing reproducible neuromorphic elements.

3.2 Neuromorphic Device fabrication and electrical characterisation

This study introduces a novel approach by utilizing thin electronic synapses based on $BiFeO_3$ (BFO) that has exceptional qualities such as high reproducibility, robust synaptic responses, and modest linearity, all of which are indispensable for the realization of efficient neuromorphic elements. BFO stands out as a well-established material characterized by its ferroelectric and antiferromagnetic properties. It can be seamlessly transformed into thin-film form through the pulsed laser deposition (PLD) technique, ensuring that the elemental ratios closely resemble those of the target material.

The neuromorphic devices constructed using BFO thin films exhibit substantial synaptic responses to input voltage pulses, with their conduction mechanisms explored in greater detail within this study.

The deposition of BFO thin films onto fluorine-doped tin oxide (FTO) glass plates via pulsed laser deposition (PLD) serves as the foundation for this investigation. A comprehensive analysis of the neuromorphic functions of these devices, including long-term potentiation (LTP), long-term depression (LTD), and spike-timing-dependent plasticity (STDP), has been diligently conducted. A crucial property for the utility of neuromorphic devices in circuits is the linear response of the excitatory postsynaptic current (EPSC) to voltage pulses. Noticeably, most of the materials reported in the literature display nonlinear behavior in their synaptic responses (potentiation and depression). However, the PPF of PLD-BFO thin films has been scrutinized extensively in this manuscript, revealing that the potentiation in BFO devices leading to LTP exhibits remarkable linearity, rendering them exceptionally suitable for a wide range of neuromorphic applications.[28,48]

3.2.1 Paired pulse facilitation (PPF)

The specific synaptic device structure employed in this study consists of a layered configuration comprising Fluorine-doped Tin Oxide (FTO) as the bottom layer, a central (active) layer of Bismuth Ferrite ($BiFeO_3$), and an upper layer of Gold (Au) as electrodes. Subsequently, the electrical characteristics of these devices were carefully examined through a series of measurements conducted using a four-point probe-station linked to a Keysight 2912A measurement unit.

To stimulate and record the electrical responses of the devices, carefully tailored pulse trains were generated within the measurement unit, aligning with the experimental requirements. From figures 3.1-3.3 we get a visual comparison between the structural elements of the fabricated device and the biological synaptic connection, highlighting the striking resemblance between the two. In this analogy, the $BiFeO_3$ layer within the device takes on the role of the synaptic cleft, serving as the interface where critical ionic movements crucial for synaptic functionality transpire. Meanwhile, the Au layer functions as the pre synapse, while the FTO layer serves as the post synapse.

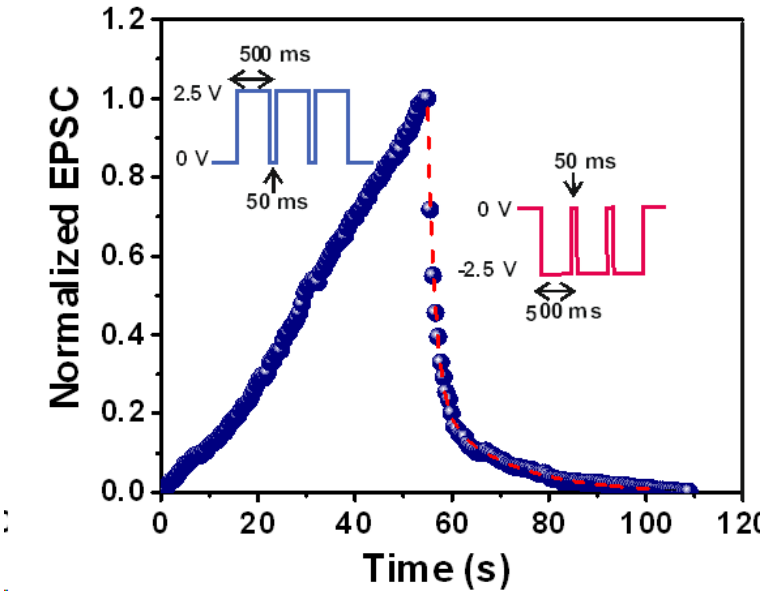

Figure 3.5 Potentiation and Depression

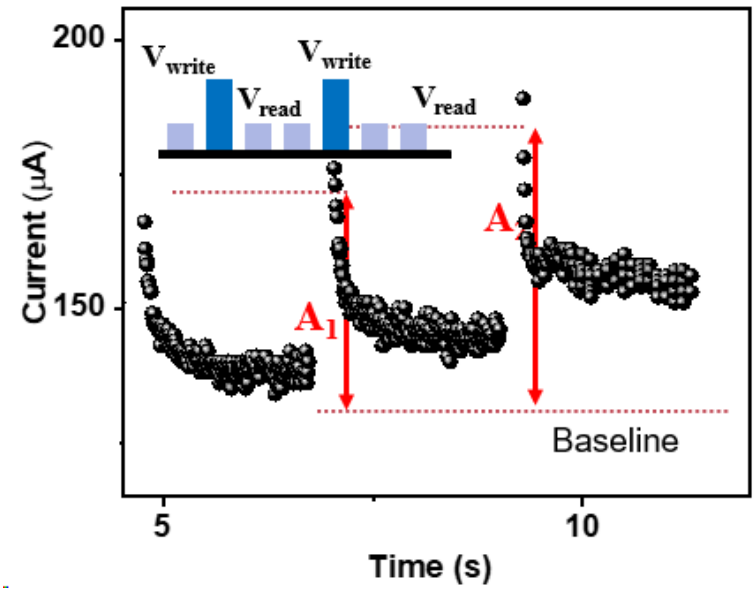

Figure 3.6 Increment in the conductance state of the neuromorphic device with series of voltage input trains

In Figure 3.5, the normalized current profiles during the potentiation and depression phases, induced by a train of action potentials, are depicted. These action potentials are characterized by a 500 ms on-time and a 50 ms off-time, with voltage ranging from 0 to ± 2.5 V. As evident from the EPSC plot, the device's response to the potentiating voltage pulses adheres to the desired linear behavior, a critical feature for neuromorphic circuit designs.

In contrast, the depression curve exhibits an exponential decay pattern, representing the relaxation of ions back to their original state within the system. This decay can be effectively fitted using a double exponential function,

$$y = A_1 \exp(-t/\tau_1) + A_2 \exp(-t/\tau_2),$$

where τ_1 and τ_2 are the time constants.[94] The calculated values reveal τ_1 to be approximately 14.52 ± 0.91 s and τ_2 to be approximately 1.55 ± 0.04 s, implying the involvement of two distinct relaxation mechanisms contributing to plasticity degradation. The rapid process, characterized by τ_2, can be attributed to the swift diffusion of ions back to their initial states, while the slower timescale, indicated by τ_1, may be associated with the polarization and relaxation of electric dipoles within the $BiFeO_3$ film.

In the figure 3.6, we see that the baseline of the conductance for the device with consecutive applied voltage inputs are gradually getting higher. With the application of the successive pulses, the conduction of the film gets modified due to the redistribution of the ions with every voltage pulse. Figure 3.7 shows the mechanism proposed for the neuromorphic responses of the BFO films under the application of constant voltage pulses.

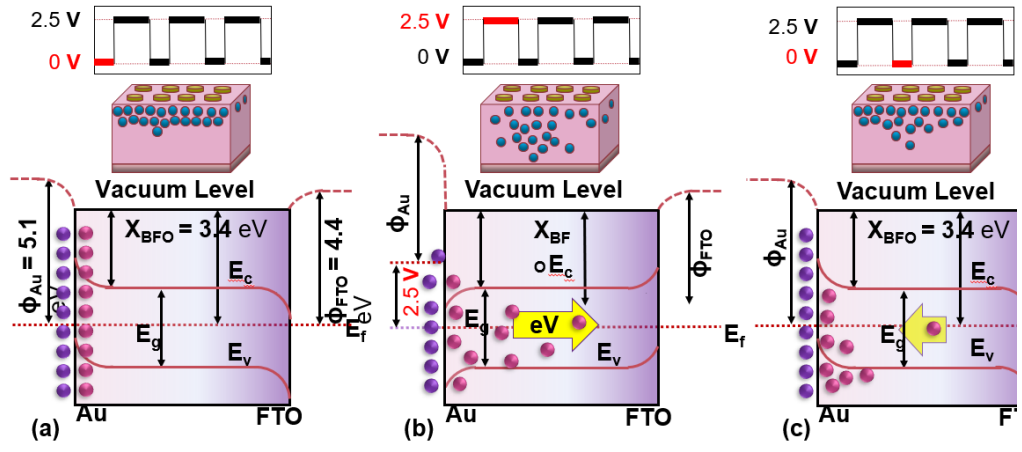

Figure 3.7 band diagram changes of the BFO device while application of the pulses

The behavior of the FTO/BFO/Au device when voltage pulses are applied, along with the band diagram is shown in the figure 3.7. When a positive voltage pulse is applied, the Schottky barrier is reduced, causing oxygen vacancies to drift into the bulk of the BFO film, as seen in Fig. 7b. Since the applied voltage (2.5 V) is higher than the Schottky barrier (1.7 eV), it causes a downward bend in the BFO band, and the Fermi

level of gold (Au) lines up with BFO's conduction band. This alignment allows electrons to move across the interface during the positive pulse.

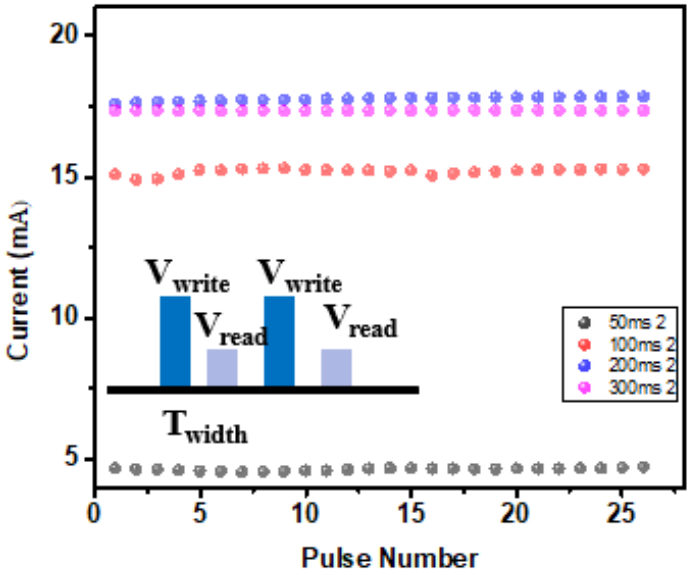

Figure 3.8 PPF for on-time variation

When the pulse returns to zero, the Schottky barrier returns, and the ions move back to the interface, as shown in Fig. 7c. However, applying repeated voltage pulses causes a cycle of releasing and partially pulling back the oxygen vacancies. The release of vacancies is mostly due to diffusion and the repulsion between ions, while their movement back to the interface is driven by the internal electric field from the work function difference. Thus, potentiation happens more slowly than depression

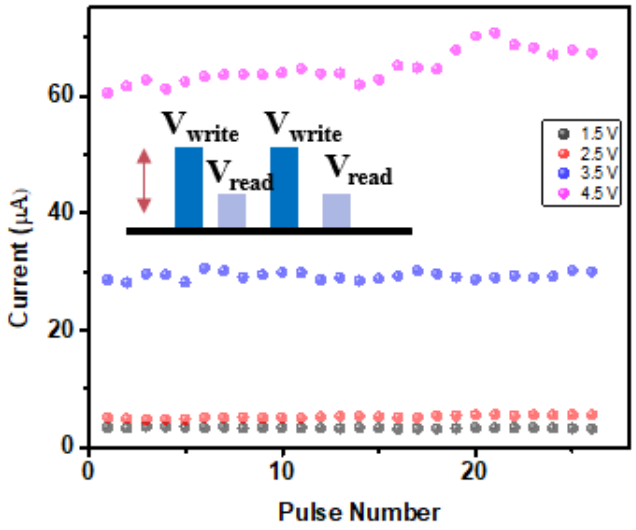

Figure 3.9 PPF for pulse amplitude variation.

The memory retention time in the device depends on how long it takes for the ions to move back to their stable positions. The movement of ions back to the interface is also affected by the repulsion between the ions. Here in figure 3.8, we see the increased conductance of the device for the increased pulse width. With the on time increasing the conductance baseline is increased respectively.

In Figure 3.9, the conductance for the device when the device with larger pulse amplitude is shown. We see that the conductance baseline and paired pulse facilitation are increased in correspondence with the increase in the voltage amplitude. Figure 3.10 illustrates the mean value of the excitatory postsynaptic current (EPSC) exhibited by five distinct FTO/$BiFeO_3$/Au devices in response to a voltage pulse train stimulus. This stimulus possesses a pulse amplitude ranging from 0 V to 2.5 V, an on-time duration of 500 ms, and an off-time interval of 50 ms. The EPSC response is notably linear, and it demonstrates a remarkable relative enhancement factor, exceeding 650% concerning the current generated by the initial pulse. It is noteworthy that all $BiFeO_3$-based devices exhibit a similar, if not more substantial, potentiation enhancement with successive action potentials.

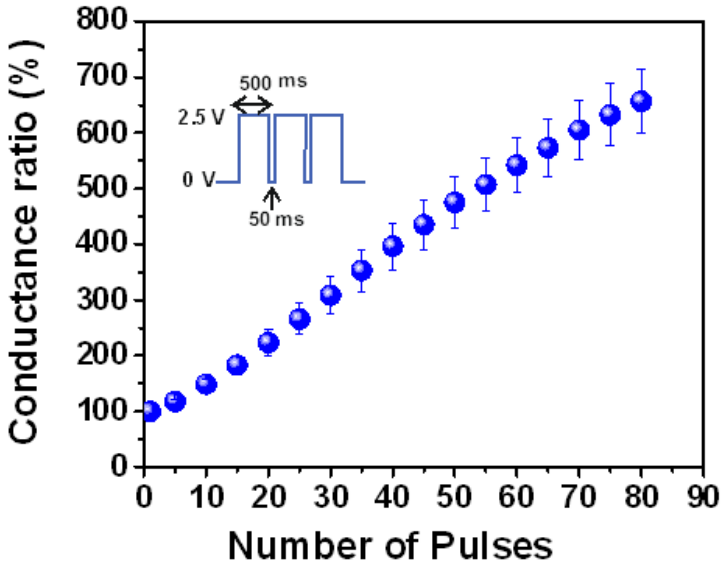

Figure 3.10 Spike number dependent plasticity (SNDP)

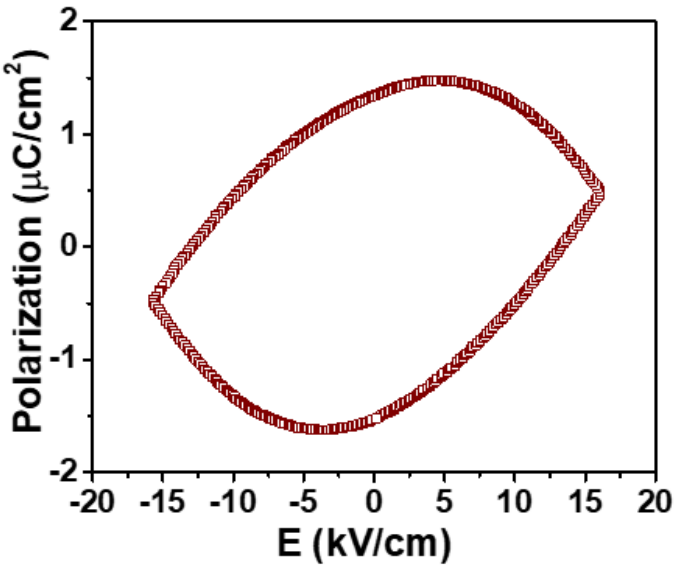

Figure 3. 11 Polarization characteristics of the BFO film

To delve further into the influence of polarization, dielectric polarization measurements were conducted on Au/$BiFeO_3$/Au devices, as depicted in Figure 3.11. Given the limited film thickness of only 70 nm, the electric field was carefully restricted to ±15 kV/cm to prevent field-induced defect generation and Fowler–Nordheim tunneling.[75,78] Nonetheless, the film still exhibited a remarkable polarization of 1.5 μC/cm^2. It is important to note that although $BiFeO_3$ is renowned for its multiferroic properties and giant polarization, the observed values in this study appeared to be significantly lower, mainly attributed to the presence of oxygen vacancies within the $BiFeO_3$ films, which in turn contributed to higher conductivity levels. This discrepancy highlights the complex interplay of material properties in these neuromorphic devices, warranting further investigation and analysis.[78,150]

3.2.2 Spike timing dependent plasticity (STDP)

The foundational concept of Hebb's postulate underlines the fundamental principle governing synaptic plasticity within neural connections. According to this postulate, synaptic plasticity arises as a consequence of the persistent and repetitive interaction between postsynaptic neurons and presynaptic neurons. This enduring stimulation leads to the reinforcement and strengthening of synaptic connections, ultimately resulting in a phenomenon known as long-term plasticity (LTP). In practice, the plasticity of a synaptic connection is a complex interplay of all the incoming spikes arriving at a neuron. Depending on the precise timing of these potentiating and

inhibitory pulses, synaptic plasticity can either be potentiated or depressed. This nuanced process gives rise to spike-time-dependent plasticity (STDP) in synaptic connections.[38]

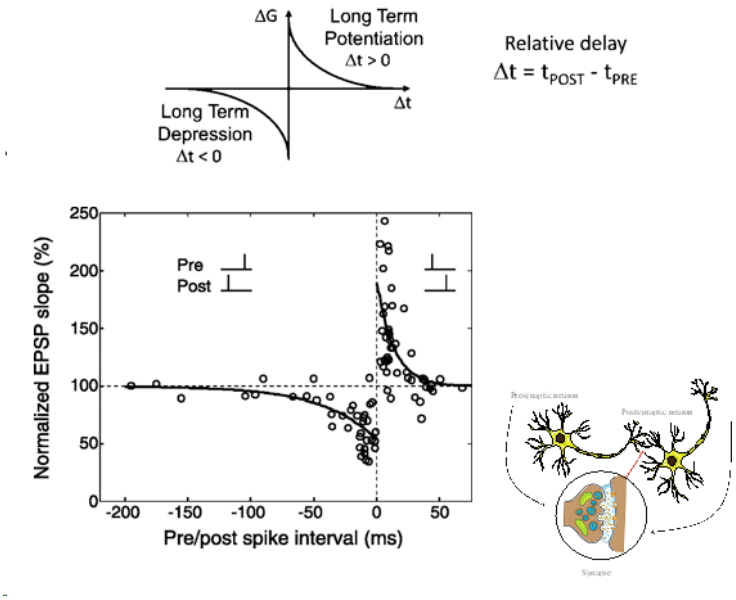

Figure 3.12 Spike timing dependent plasticity (STDP) of a biological neuron (ref.[151])

While STDP primarily hinges on the timing of spikes in biological neurons, an intriguing parallel can be drawn to electronic synapses. In electronic synapses, a similar effect can be induced by employing opposite voltage pulses separated by a time interval Δt. This phenomenon bridges the gap between biological neural systems and their electronic counterparts.

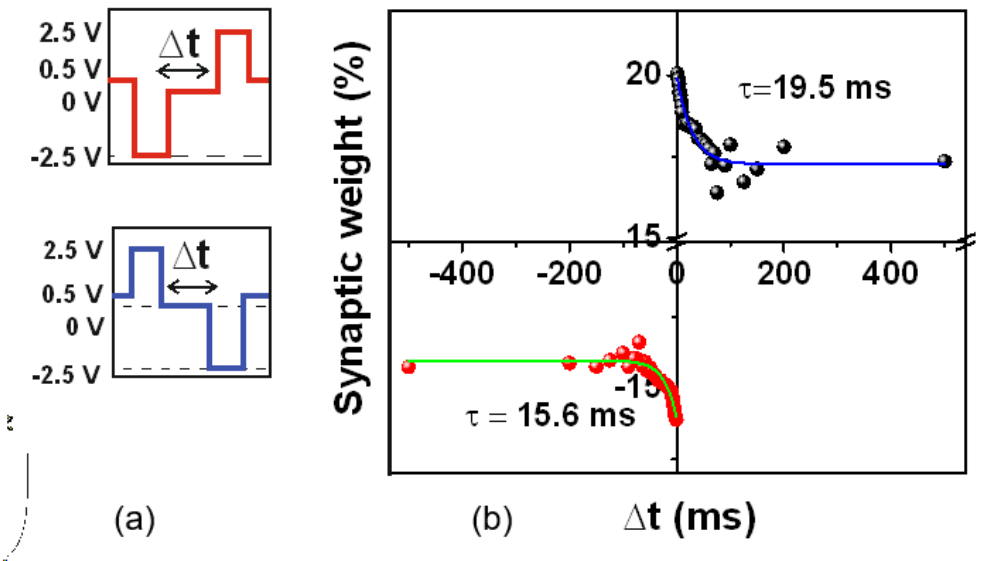

Figure 3.13 STDP of the BFO neuromorphic devices. a) Voltage pulses b) Characteristics

By applying pre- and post-neural pulses with varying time delays, as illustrated in Figure 3.13a, we measured the STDP of the FTO/$BiFeO_3$/Au device, as shown in Figure 3.13b.

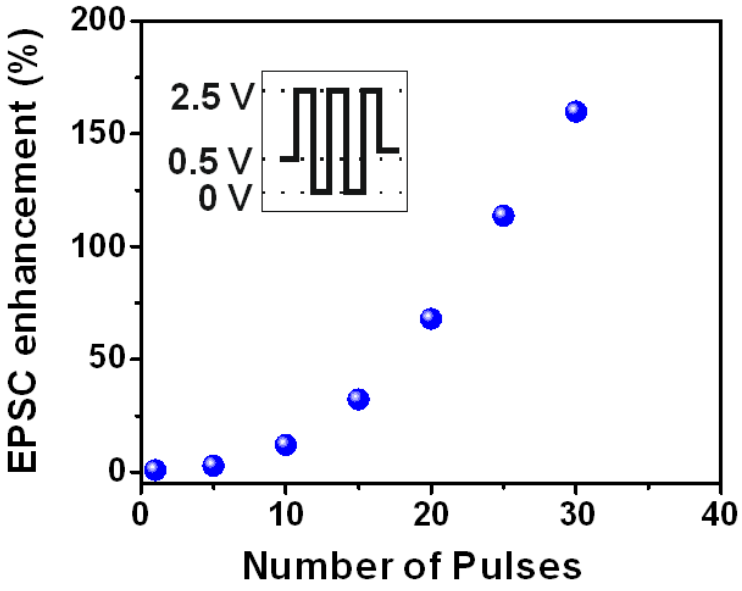

Figure 3.14 Spike number dependent plasticity of the FTO/BFO/Au devices

In cases where Δt assumes a positive value, the system exhibits potentiation characterized by a relatively short timescale of 19.5 ms, indicative of short-term plasticity. Conversely, when Δt is negative, the system undergoes short-term depression, with a timescale of 15.6 ms. These distinct characteristics bear a striking resemblance to the STDP patterns observed in biological neural systems. Notably, these findings are pivotal in understanding Hebbian learning and associative learning in biological neural systems. This understanding extends beyond biology and finds application in the realm of machine learning, where unsupervised learning processes are grounded in similar principles.[151]

Associative learning, a cognitive feature typically attributed to the collective activities of several neurons converging on a single synapse in biological systems, can be effectively replicated in electronic synapses using a single device.[152] This noteworthy development has profound implications for the integration of neural functions at a large scale within integrated circuits, all within the constraints of nanoscale device dimensions. The ability to mimic such essential learning mechanisms in electronic synapses paves the way for more advanced and efficient neuromorphic computing systems.

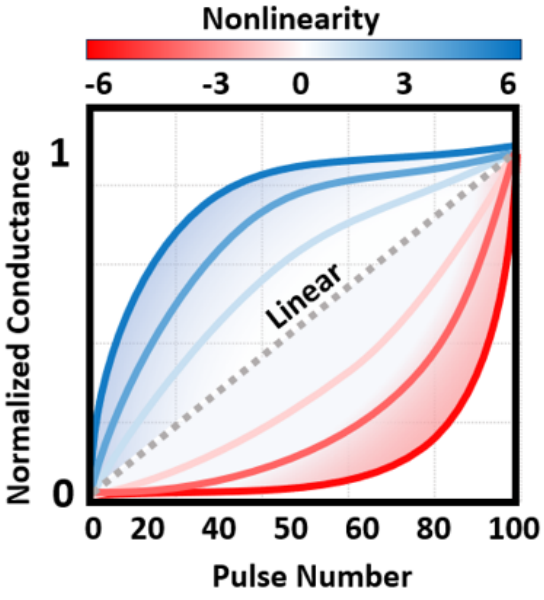

Figure 3.15 Linearity diagram

The concept of plasticity in learning, especially when subjected to repeated cycles, plays a fundamental role in comprehending how both human and artificial brains adapt to various stimuli. Within the context of this chapter, we delve into a specific methodology known as spike-number-dependent plasticity (SNDP) as a means to investigate and elucidate this phenomenon. SNDP is a technique that enables us to observe alterations in the base-current of a device before and after applying a series of action potentials. In essence, it provides us with insights into how the frequency and quantity of spikes can modulate the effectiveness of synaptic connections, thus drawing a parallel to the process of learning in human brain.[153]

The significance of SNDP becomes particularly evident in artificial synapse. Our research reveals that as we apply more electrical pulses to an artificial synapse, its conductivity improves. This observation holds substantial implications for the development of devices designed to emulate human synapses. As Figure 3.14 visually demonstrates, we illustrate this phenomenon using square wave potential spikes, effectively showcasing SNDP in action. Furthermore, we employ this data to quantitatively measure the changes occurring within the synapses of our device, thereby providing a concrete basis for our findings.

Beyond SNDP, the role of pulse frequency emerges as a critical factor in the behavior of these artificial synapses. This is where spike-frequency-dependent plasticity (SFDP) comes into play. SFDP considers the rate at which action potentials

are fired, adding an important temporal dimension to the learning and memory processes of artificial systems. Our exploration of SFDP offers valuable insights into how the precise timing of neural signals influences synaptic strength. This understanding holds paramount importance when designing advanced neuromorphic systems that aim to replicate not only the structural characteristics of human synapses but also their remarkable capacity for learning and retaining information.[149,154]

In summary, the meticulous examination of SNDP and SFDP in artificial synapses stands as a cornerstone in the comprehension of synaptic plasticity. This knowledge is of utmost importance in the field of neuromorphic engineering, as it empowers us to advance the development of devices that not only mimic the intricate architecture of human synapses but also replicate their unparalleled ability to learn and remember information, heralding a new era of artificial intelligence.

3.2.3 Linearity of the synaptic response

Incorporating electronic synapses into real circuits requires meeting certain critical criteria, and among these, the linearity of synaptic weight updates emerges as a pivotal factor. This characteristic ensures the precision and reliability of information processing in artificial neural networks.[155] In Figure 3.5, we can discern the inherent linearity in the synaptic weight update, particularly in the context of Long-Term Potentiation (LTP), where the Excitatory Postsynaptic Current (EPSC) exhibits a linear relationship with the number of applied voltage pulses. To rigorously assess the linearity of this synaptic weight update, we followed a previously established methodology. The resultant theoretical fit, based on experimental data, is presented in Figure 3.16.

$$I_p = I_{min} + \left(\frac{I_{max} - I_{min}}{1 - e^{-\frac{P_{max}}{A}}}\right)\left(1 - e^{-\frac{P}{A}}\right)$$

$$I_d = I_{max} - \left(\frac{I_{max} - I_{min}}{1 - e^{-\frac{P_{max}}{A}}}\right)\left(1 - e^{\frac{P - P_{max}}{A}}\right)$$

Where I_p, I_{min}, I_{max}, P_{max}, I_d, are Potentiation current, minimum current, maximum current, maximum number of pulses to reach that current change, and depression current respectively.

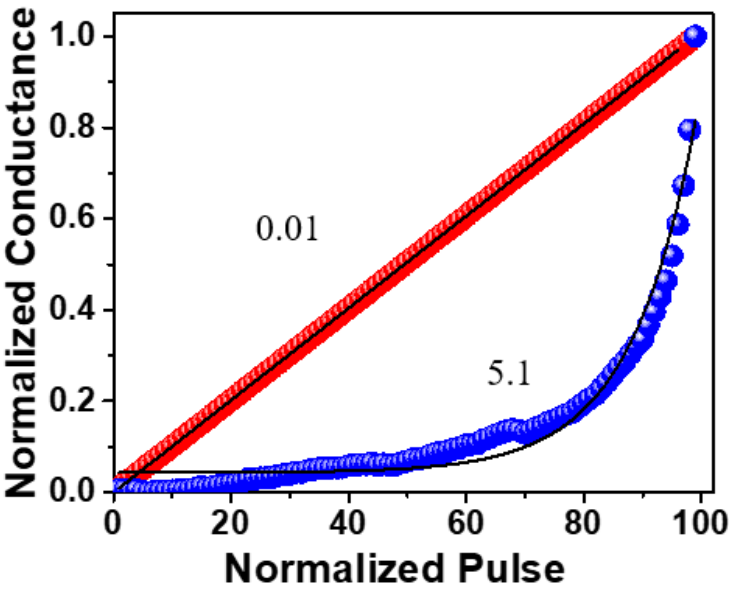

Figure 3.16 Linearity of the device for potentiation and depression is 0.01 and 5.1 respectively.

Our analysis reveals that the nonlinearity factor (NLF) associated with LTP is astonishingly low, measuring less than 0.01, while that of Long-Term Depression (LTD) stands at 5.1. This stark contrast in NLF values between potentiation and depression originates from the underlying physical mechanisms governing these two processes.[155] LTP is primarily an electric field-assisted, drift-driven phenomenon, wherein the applied voltage pulses play a critical role in facilitating synaptic strengthening. Conversely, LTD occurs either in the absence of an electric field, which is dominated by diffusion, or when the voltage polarity is reversed. In the latter scenario, a complex interplay between drift and diffusion forces prompts the ions to return to their original equilibrium distribution. Consequently, the ion migration mechanisms in these two cases differ significantly.

Notably, the NLF values reported in this study are comparable to those of recently reported synaptic devices based on materials like MoS2 and graphene. However, our devices exhibit superior linearity, particularly in the context of LTP. This enhanced linearity bodes well for the practicality of these synapses in applications such as pattern recognition, where a high degree of learning accuracy is paramount. To put this into perspective, the NLF reported here indicates a learning accuracy exceeding 95%.[19,94]

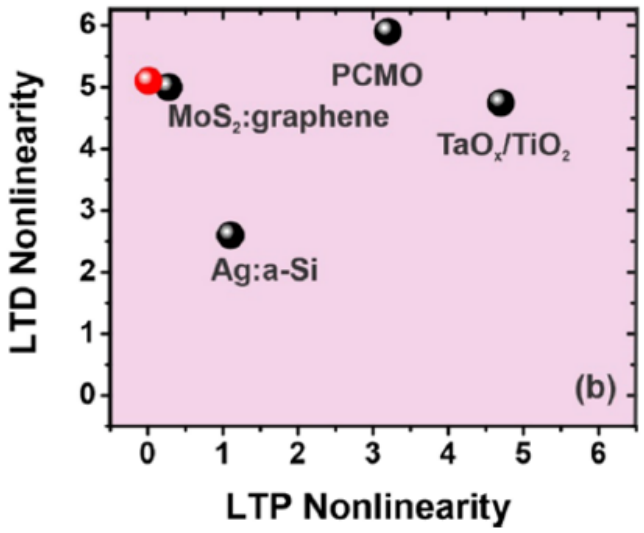

Figure 3.17 Linearity of the device when compared with other reported devices.

For a comprehensive assessment of our devices, Figure 3.17 provides a comparative chart displaying NLF factors reported in the existing literature, serving as a benchmark for the performance of our electronic synapses. This comparative analysis reaffirms the exceptional linearity and precision of our synaptic weight updates, underscoring their potential significance in the field of artificial neural networks and advanced computing systems.

3.3. Conclusion

In this section, we present a comprehensive summary of the key findings and implications of our research on the construction of synaptic devices through the pulsed laser deposition of $BiFeO_3$ thin films. The results of our study demonstrate remarkable synaptic properties, holding significant promise for advancing the field of neuromorphic engineering. Our investigation has successfully yielded synaptic devices capable of generating an exceptional excitatory postsynaptic current in response to input voltage stimuli. This observed electrical behavior underscores the proficiency of $BiFeO_3$ thin films as a promising material for the development of synaptic devices. Moreover, the depression curve associated with these devices has revealed the presence of two distinct relaxation processes. We have attributed these processes to ionic relaxation with a fast timescale and the dielectric polarization component with a slower

timescale, shedding light on the complex dynamics underlying the functionality of these devices.

Of particular significance is the observation that our $BiFeO_3$-based synaptic devices exhibit remarkable spike-time-dependent plasticity (STDP), a phenomenon reminiscent of Hebbian-type associative learning observed in biological neurons. This characteristic is of paramount importance for the field of artificial intelligence as it opens the door to unsupervised learning mechanisms. Our findings have also demonstrated the ability of these devices to engage in repetitive learning, characterized by spike number-dependent plasticity (SNDP), further showcasing their potential for practical application in neuromorphic systems.

One critical aspect of our research pertains to the nonlinearity of synaptic weight updates. We have calculated the nonlinearity factor for Long-Term Potentiation (LTP) to be less than 0.01, equating to a learning accuracy exceeding 95%. This exceptional accuracy in synaptic weight modulation underscores the robustness and reliability of our devices.

Looking forward, the potential for further enhancements in device linearity through material modifications is a promising avenue of research. By refining the properties of $BiFeO_3$-based devices, we can optimize their overall linearity, thereby expanding their compatibility with Complementary Metal-Oxide-Semiconductor (CMOS) technology. The versatility and adaptability of $BiFeO_3$-based devices hold tremendous potential for shaping the future of neuromorphic engineering, providing a solid foundation for continued advancements in artificial intelligence and cognitive computing.

Chapter 4:

Tuning the neuromorphic properties of BFO Devices for Application

4.1. Introduction

The well-known von Neumann bottleneck of current computer architecture arises due to the latency of fetching the data through stringent bus-lines in the conventional computers.[156–158] Recent developments in the technology demands an exponentially increasing digital data to be administered in the near future. Be it the large set of unstructured data from Internet of Things (IoT) sensors or various devices, handling them is beyond the capability of conventional computers.[159] Administering such large volume of data requires fast and energy-efficient computational techniques that goes beyond the von Neumann architecture. Though Artificial Neural Networks (ANN) has been widely employed in daily life, the hardware base to perform artificial intelligence operations is still the conventional Complementary Metal-Oxide-Semiconductor (CMOS) platform, which is highly power consuming.[160] Evidently, a novel technology that is compatible with the ANN system is the need of the hour to replace the von Neumann architecture. Among the various options, Neuromorphic technology is a promising emerging technology that emulates the functioning of the neurons in biological brain, where multitudes of neurons are interconnected through synaptic terminals to form an enormous neural network.[161]

Several device schemes have been proposed to create neuromorphic characteristics, which mainly include memristors, [162–165] and memtransistors.[166] Memtransistors is memristive transistors with the advantage that it inherently has the 1T-1R configuration in a single device, however, at the expense of three terminals per device. Memristive neuromorphic devices are simpler in the sense that it has only two terminals and the operation and device stacking is comparatively simpler than memtransistors. Memristors are faster than the floating gate (flash) memory in write and read process and have larger endurance.[166] In memristive neuromorphic devices, the history of the previous measurements manifest either as hysteresis in the current-voltage sweeps, or as successive increase in current for voltage pulses of constant

amplitude. While the strengthening of a neural path leads to memory in biological neural networks, strengthening of electrical conductivity is emulated in electronic synapse by means of manipulating the traps, moving charges, polarizations etc. The kinetics of these charges and polarizations will lead to long-range or short-range plasticity. Since ions and free charges move swiftly, neuromorphic systems based on those generally exhibit short-range memory. In this perspective, several material combinations have been examined to enhance the memory per pulse, which is known as paired pulse facilitation (PPF), and to increase the memory retention time per pulse, which gives the long-term plasticity. A combination of ion kinetics and polarization is useful to enhance the memory.[167] Multiferroic materials are particularly interesting candidates for memristive neuromorphic devices due to their large polarizations in addition to the inherent oxygen vacancies in the sample.

Among various multiferroic materials investigated for neuromorphic applications, Bismuth ferrite ($BiFeO_3$, BFO) is a ferroelectric material with a large ferromagnetic phase transition Curie temperature (1103 K) and antiferromagnetic phase transition Neel temperature (643 K) [168] which makes it an important material for wide range of applications that range from photovoltaics[134] to optoelectronics, spintronics, ferroelectric memory, and magnetic memory applications.[169–171] Recently, we have reported BFO as a material with large neuromorphic memory .[167]

In this work, we show that the linear weight update of the neuromorphic device is directly related to the oxygen vacancies present in the film. Researchers have used many ways to change the oxygen vacancies in the BFO film they used, some include change the concentration of bismuth, hence manipulating the oxygen vacancies.[138] Doping is another way to tune the oxygen vacancies in BFO.[172] In this work, we changed the oxygen vacancies in the film by changing the oxygen percentage during the pulsed laser deposition (PLD) of the film. After deposition the film at different oxygen percentage, we confirmed the change in oxygen vacancies in the films using X-ray Photoelectron Spectroscopy (XPS), and the impact of the oxygen vacancies in the paired pulse facilitation (PPF), spike-time dependent plasticity (STDP) and the nonlinearity of the PPF has been studied.

4.2 Fabrication of the Synaptic Devices:

The BFO synaptic devices were fabricated with a metal−insulator−metal (MIM) structure. Device structure is shown in figure 4.4 (b). Bismuth Iron Oxide ($BiFeO_3$) films were deposited on the Fluorine doped Tin Oxide (FTO)/ glass substrate using pulsed laser deposition (PLD) technique. The BFO target (99.9% pure) was procured from ACI Alloys, Inc. (San Jose, USA). BFO thin film neuromorphic devices were made in a metal-insulator-metal (MIM) capacitor structure with FTO as bottom electrode and gold as top electrode. Gold top electrodes were deposited by thermal evaporation. An array of thin film devices is fabricated with a shadow mask of 1 mm^2 area for top electrode. For pulsed laser deposition, a Nd-YAG solid-state high-power laser is used, at a power density of 4J/cm^2. Third harmonics of a Q-switched solid-state Nd: YAG laser (Quanta Ray, Spectra-Physics) of wavelength 355 nm with a repetition rate of 10 Hz and a pulse width of 8 ns was used to ablate the target materials. Substrate temperature of 400 ° C is used. The base pressure of the deposition chamber was 10^{-6} mbar, but the working pressure during the deposition was maintained at 0.2 mbar. For reactive PLD, oxygen was fed to the system mixed with argon during the deposition, maintaining a total 40 sccm gas flow into the chamber. Three sets of samples were deposited varying oxygen content as 0% oxygen and 100% Ar (0 sccm oxygen and 40 sccm Ar), 50% oxygen and 50% argon (20 sccm oxygen and 20 sccm argon) and 100% oxygen and 0% Ar (40 sccm oxygen and 0 sccm argon).

An extensive material analyses of the pulsed-laser-deposited BFO films has been reported in our earlier work.[167] Since we are varying the oxygen content in the film to examine the linear weight update of the devices, X-ray photoelectron spectroscopy (XPS, Thermo Scientific ESCALAB) was employed to analyse the chemical and elemental properties of the film. The electrical and neuromorphic properties were recorded by a precise source/measure unit (Keysight B2912a).

4.3 Material Characterization:

We have reported earlier that the BFO films deposited are polycrystalline as the XRD patterns indicate and were matching to the space group of R3c, showing a distorted perovskite crystal structure. Sharpness of the peak at 32 shows the high

crystallinity. It is important to see that the crystalline nature of the films is not changed with variation of the oxygen vacancies in the films. XPS was used to find the elemental composition of the film. Regardless of the oxygen pressure used, the composition of the film is nearly same as the molecular formula $BiFeO_3$, while noticeable changes are there with the oxygen vacancies as will be discussed later in this manuscript. The narrow range scan of the bismuth, iron and oxygen are taken for each film and the detailed comparison has been done. Figure 4.1 (a) shows the broad-scan spectrum of the BFO sample. Figure 4.1 (b) and (c) show the narrow range scan spectra for the Bi 4f and Fe2p. Similarly, we have details of the element iron, Fe 2p spectra in figure 4.1(b). Deconvoluted spectra shows binding energies corresponding to Fe 2p1/2 and 2p3/2, which is due to the spin orbit effect. Presence of satellite peak at 718 which is 8 eV to the 2p2/3 shows that the valence state of the iron in the film is 3+.

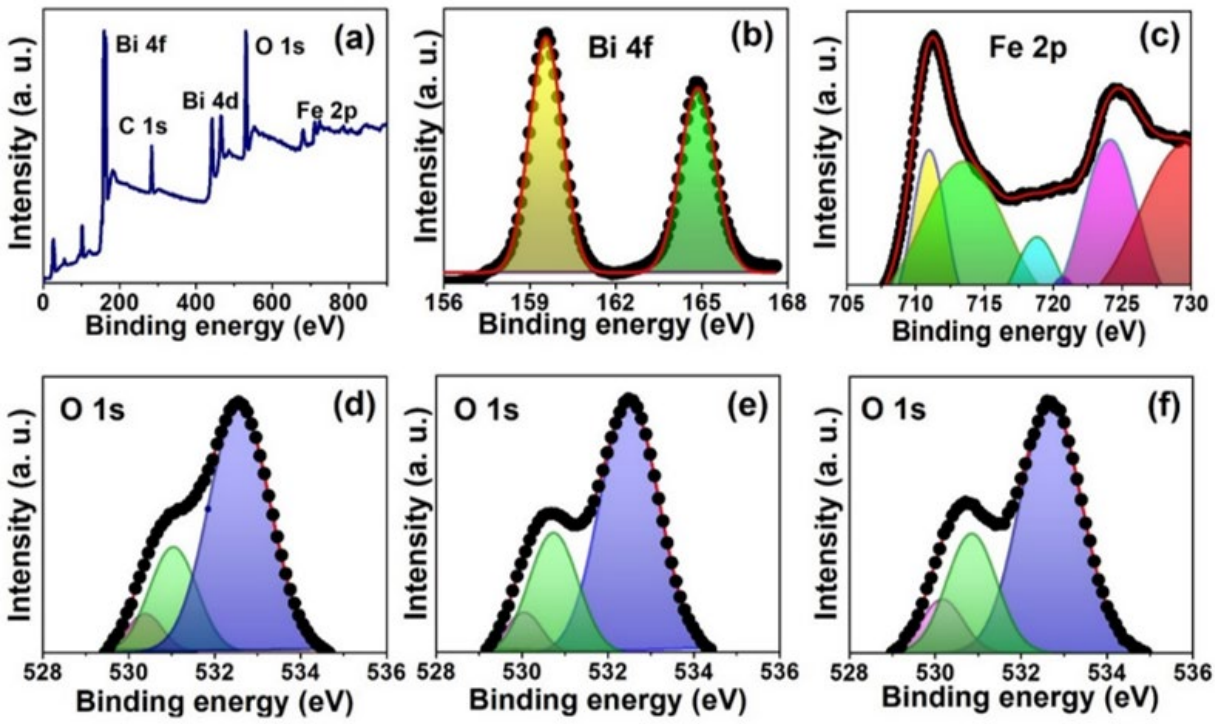

Figure 4.1 XPS spectra of samples. (a) shows a broad scan of the sample (b)bismuth 4f; (c) spectra of Fe 2p electronic binding energy; (d) oxygen 1s spectrum of $BiFeO_3$ deposited with O: Ar = 1:0, (e) O: Ar = 1:1 and (f) O: Ar = 0:1. The peak at 530.7eV corresponds to oxygen vacancies and the peak at 532.6 eV corresponds to the adsorbed oxygen. These relative intensity ratios (RIR) of oxygen vacancies to the adsorbed oxygen are 0.101, 0.111, and 0.145 respectively.

The figure 4.1 (c)-(e) shows the detailed spectra of the oxygen O 1s spectra in details. (c), (d), and (e) are in decreasing order of oxygen vacancy concentration in the films. We see three peaks for the oxygen spectra given here. Peaks at 530 eV corresponds to the metal bonded oxygen atoms. Peaks at 531eV corresponds to the

dangling bonds, mainly the oxygen vacancies. Peaks at 532 eV is the presence of the adsorbed oxygen. The prominent peak of oxygen is due to adsorption of OH^- groups at the surface forming the lower energy peak component in the spectra.[173,174] Relative intensity ratio (RIR) of the oxygen peaks can help us to determine the relative quantity of the oxygen vacancies in the films. Relative peak intensity ratio of the film is determined by ratio between the relative intensity of the oxygen-metal bond peak and the sum of the peak intensities of the dangling bond and the adsorbed oxygen. Here onwards, we refer to the devices as Device 1, Device 2 and Device 3 with RIR in increasing order. Assigning the values, we refer Device 1 is with minimum RIR of 10.2%, Device 2 is with RIR value of 11.05% and Device 3 is with the RIR of 14.51%.

Figure 4.3 (a) shows the diagram of a biological synapse, through which the neurons are interconnected. Fig. 4.3(b) explains the configuration of the device fabricated, with FTO as the bottom electrode, BFO as the active medium and gold as the top electrode, which decides the device area. Figure 4.3(c) shows the current-voltage curves plotted as log(I) versus log(V) at the high resistive state (HRS) for devices 1,2 and 3. This figure shows that the leakage current through the device depends upon the defect density in the films, due to larger space-charge limited conduction. Leakage current of the films show a trend that is expected from the defect assisted leakage. Figure 4.3 (c) shows the leakage current measured at the high-resistive state. The log(I)-log(V) plots have two linear sections, one with slope 1 and another with slope 2, which correspond to Ohmic and space-charge-limited current (SCLC) conduction regimes. With increasing oxygen content, less oxygen vacancies will be present in the film, which in turn reduces the (oxygen-vacancy-related) trap states in the material. The first indication of this comes from the lowering of leakage current as the oxygen pressure increases. Trap density (N_t) can be calculated from the Ohmic-SCLC transition voltage (V_T) using the expression [175]

$$N_t = \frac{2\varepsilon V_{TFL}}{qd^2} \qquad (1)$$

where, V_{TFL} is known as the trap-filled-limited voltage, d is the thickness of the film and ε is the dielectric constant of BFO. Figure 4.3(d) is a plot between N_t and RIR, which shows that the trap density reduces with increasing oxygen pressure during the deposition. Comparing with the conclusions made from the XPS data, this result confirms that the oxygen vacancies increase with reducing oxygen pressure during the

deposition of the BFO films, and they influence the overall conduction mechanisms of the BFO layers.

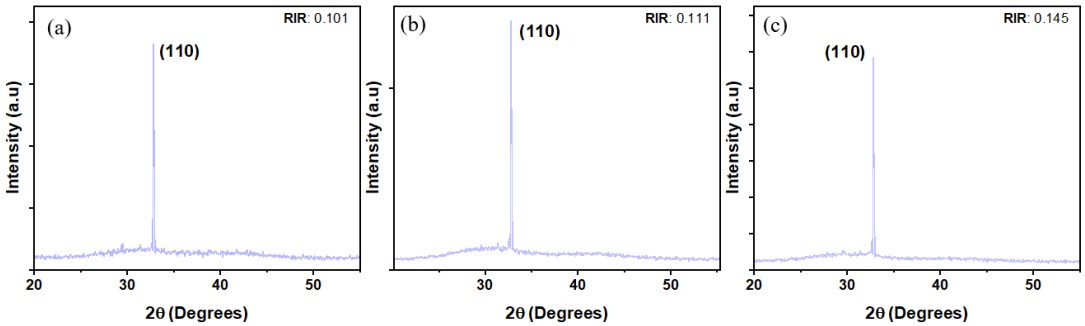

Figure 4.2 X-ray diffraction of the different films shows that despite the oxygen vacancy variations among the films, the crystallography remains similar. (a) RIR: 0.101 (b) RIR: 0.111 and (c) RIR: 0.145

Further, we examined the influence of the oxygen vacancies in the neuromorphic properties of the BFO devices. This allows us tuning the neuromorphic properties of the device as per the application needs. Oxygen vacancies are a key player in the conduction mechanisms in dielectric materials and have been extensively studied using various techniques.[176] For studying the effect of oxygen vacancies in the neuromorphic properties of BFO neuromorphic device, we applied a series of voltage pulses and examined the electrical responses from the device. From these responses, the main neuromorphic responses such as paired pulse facilitation (PPF), spike-timing-dependent plasticity (STDP) and linearity of the response have been studied.

With the series of positive voltage pulses an increase in current is observed, which is termed as potentiation and when a reverse voltage pulse is applied, the synaptic current diminishes in an exponential way, which is termed as depression.[177] Potentiation corresponds to an increased synaptic weightage, while depression corresponds to a memory decay. The possibility of electrically activated depression is an advantage of the electronic synapse compared to the biological synapse, where memory degradation is gradual and occurs over longer timescales. Normally the time constant of the exponential function fitted to the depression curve, one can identify whether the system has long range potentiation (LTP) or short-range potentiation (STP).

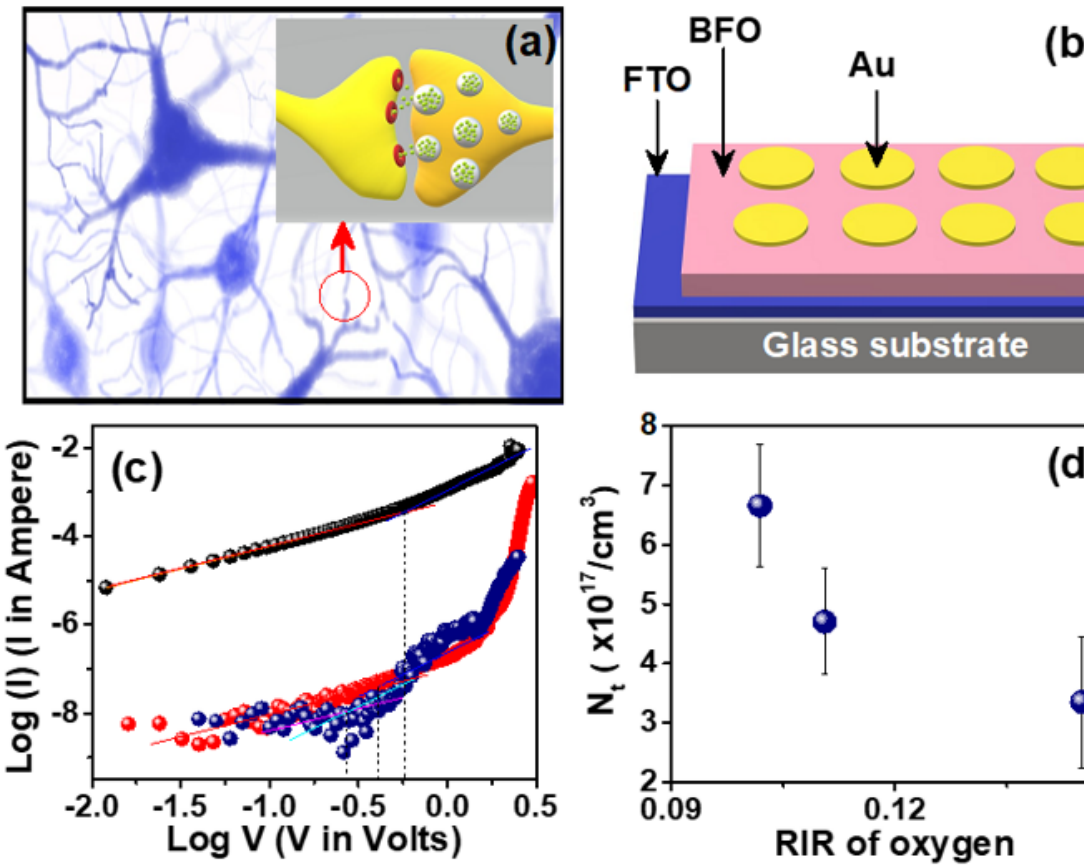

Figure 4.3 (a) A pictorial representation of synaptic connections. The inset image shows the representation of a single synapse. (b) A simple BFO neuromorphic device, (c) The log (I) versus log(V) plot to explore the conduction regimes of the currents (d) shows the trap density in the material (Nt) determined using Equation (1)

Figure 4.4 (a) shows the potentiation and depression behaviour of Device 1, Device 2, and Device 3, where each curve is an average over 5 consecutive measurements. For measuring the synaptic weight, a series of voltage train with a peak voltage of 2.5 V was applied to the device and its current output was monitored. A similar voltage pulse series of peak voltage -2.5V was applied to study the depression behaviour.

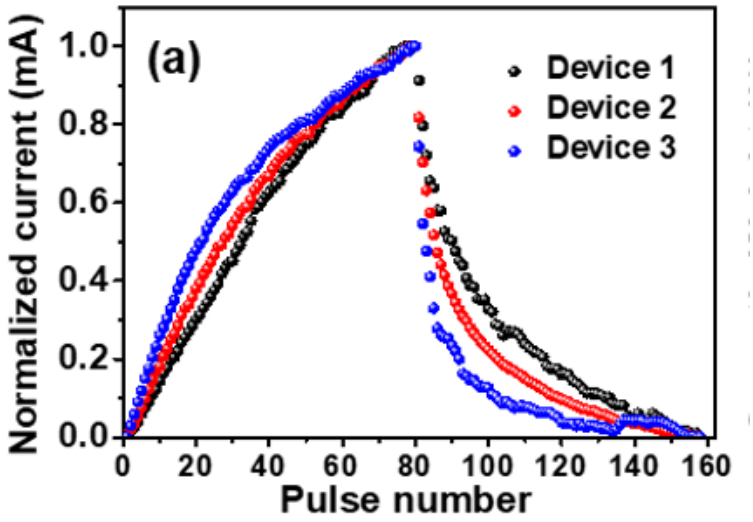

Figure 4.4 The potentiation and depression curves of Device 1, Device 2 and Device 3 plotted together

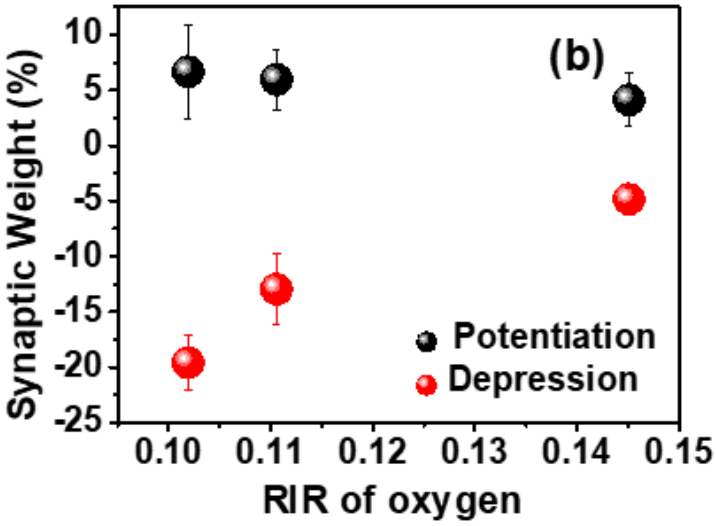

Figure 4.5 The synaptic weight as a function of Relative Intensity Ratios of oxygen peaks in XPS.

Figure 4.5 illustrates the synaptic weight of three samples deposited at varying oxygen ratios, resulting in different densities of oxygen vacancies, as indicated by their respective RIR values. The graph clearly shows that the synaptic current response becomes more linear with an increase in oxygen vacancies. Additionally, Figure 4.5 demonstrates that as the RIR increases (indicating fewer oxygen vacancies), the synaptic weight also increases. Synaptic weight, or Paired Pulse Facilitation (PPF), was calculated by measuring the percentage change in the output amplitude of the device

compared to the preceding pulse.[178] This is a clear indication that neuromorphic characteristics are heavily influenced by the oxygen vacancies in the material.

Neuromorphic devices emulate the basic ion kinetics of biological neurons. Here it is achieved by the manipulation of oxygen vacancies in the BFO films. The only difference is that the spiking of a neuron in biological neural systems may be caused by multiple factors – not only by the neurotransmitters released by the pre-neuron, but due to the influence of other neurons connected to it as well. While the coherence of the release of neurotransmitters and their entry to the post-neuron gives the highest memory, any time delay in releasing the neurotransmitters or receiving them in the post-synapse considerably affects the memory of the network. This introduces a spike-time dependent plasticity (STDP), which determine the Hebbian associative learning behaviour of the neural system.[179] In electronic synapse, STDP is estimated by measuring the synaptic weight update for pulses when a deliberate time difference between the pulses is provided. These pulses represent the voltage spike from a pre-neuron to post-neuron. One pulse corresponding the release of the chemical from preneuron, while the opposite pulse corresponds to the binding of the chemical to the post neuron. When the supply (from preneuron) and demand (to post neuron) are delayed by a time factor, the probability of quality transaction have an exponential impact. If the timing between the two are lesser, the transaction happens with more probability and for larger intervals, the transaction probability and hence the quality of synaptic weight update reduces considerably. Figure 4.6 shows the STDP measured for the devices with different oxygen vacancies.

Figure 4.6 (a)-(c) show the STDP measured for the devices with different oxygen vacancies. All these curves show Hebbian pattern of associative learning, but with different potentiation and depression timescales. By fitting exponential functions to the data (shown as the solid curves in the figures (a) to (c)), their timescales can be extracted. Figure 4.6 (d) shows the potentiation and depression timescales of the devices with various oxygen vacancies, which shows a clear trend of increasing the time constant with reducing the number of oxygen vacancies (larger RIR means lower density of oxygen vacancies). This can be explained by considering the simple ion kinetics in the system.

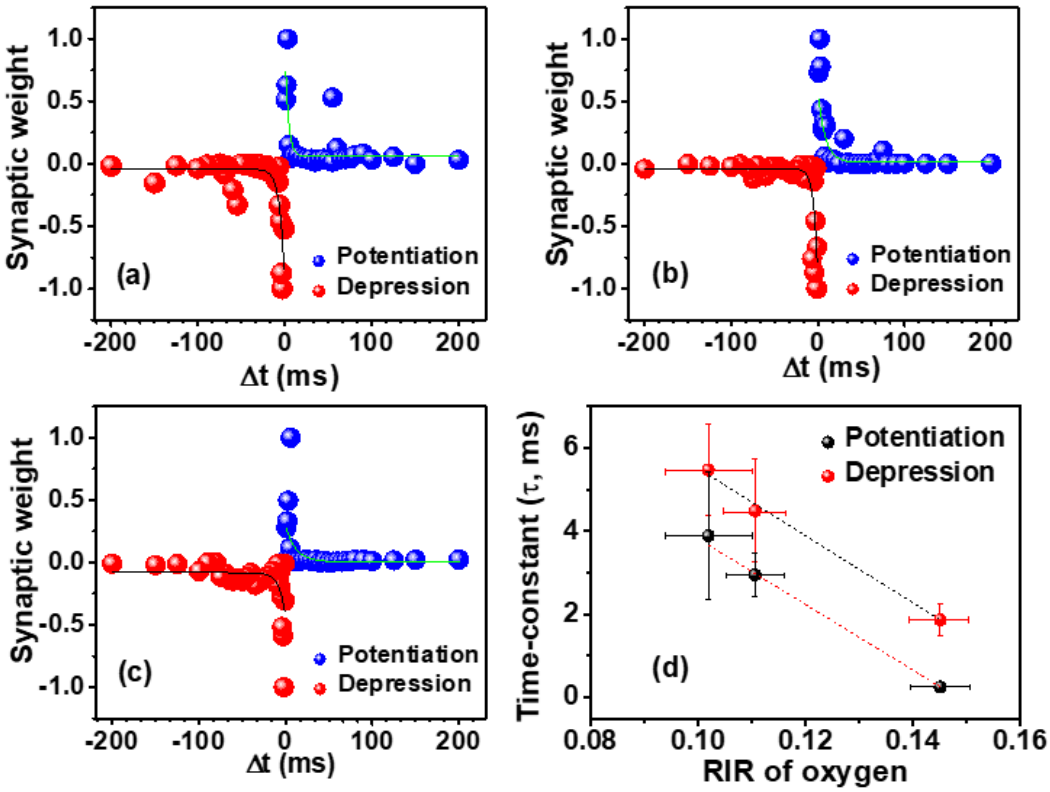

Figure 4.6 STDP measured for (a) Device 1, (b) Device 2, and (c) Device 3. The data given is an average of 10 measurements. (d) the time-constants associated with potentiation and depression in the Hebbian learning curves shown in (a) to (c).

Figure 4.7 (a) shows the band diagram of the Au/BFO/FTO device. Since Au has a larger work function (5.1 eV) as compared to the electron affinity of $BiFeO_3$ (3.4 eV),[180] a sudden electron depletion occurs at the Au/BFO interface, which gives rise to the BFO bands bending up, introducing a Schottky barrier of 1.7eV at this junction. This Schottky barrier separates the electrons in Au and the positive charges (oxygen vacancies) in the BFO film. Thus, a high-density layer of the oxygen vacancies arises in BFO layer close to the junction. When a positive voltage pulse of peak voltage V is applied, the Schottky barrier lowers by eV, thus releasing the oxygen vacancies into the bulk of the BFO film as Fig. 4.7 (b) shows. Since the applied voltage (2.5V) is larger than the Schottky barrier (1.7 eV), the band bending is downward in BFO, and the quasi-static Fermi level of Au will match with the conduction band of BFO. This makes electron pumping across the interface possible during the positive cycle of the pulse.

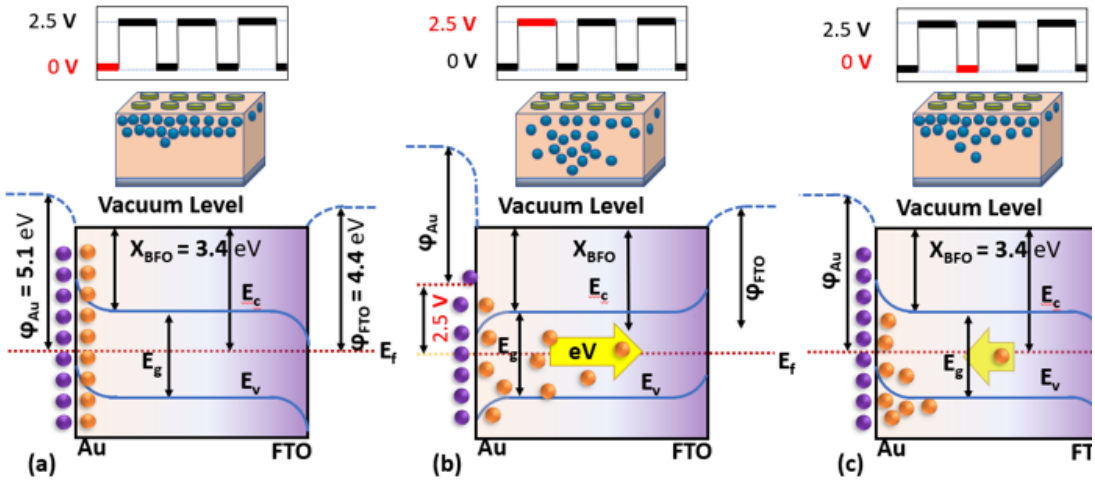

Figure 4.7 The band diagram modulation of the Au/BFO/FTO device explaining the mechanism when voltage pulses are applied. (a) Band diagram of the Au/BFO/FTO device forming the Schottky junction between Au and BFO. (b) when the voltage pulse is applied, the oxygen vacancies diffuse into the bulk of BFO; (c) when the voltage pulse goes back to zero, the barrier is restored, and the ions undergo drift and diffusion back to the interface.

When the voltage pulse comes back to zero, the Schottky barrier is set again, and the released ions are driven back to the interface (Fig. 4.7 (c)). However, by applying successive voltage pulses of certain duty cycle, continuous release and partial withdrawal of oxygen vacancies occur. Due to this dispersion of the oxygen vacancies, the conductivity of the medium increases with successive pulses, which manifests as the PPF (Fig. 4.4 The release of oxygen vacancies is driven mostly by diffusion and inter-ionic Coulomb repulsion, while the withdrawal back to the interface is driven by drift due to internal electric field set up by the work function difference. Therefore, the potentiation will be slower than depression, as seen in Figure 4.4 (a). How long the memory is retained will be decided by the drift and diffusion of the ions back to their equilibrium positions, where they are thermodynamically and electrostatically stable. The transport of the ions back to the interface can be enhanced or slowed down by the Coulomb repulsion between ions. Figure 4.6 (d) suggests that the dynamics of the system is slower when the defect density is larger, which is understandable from the time taken for the defects to return to their equilibrium positions once they are disturbed by an action potential. Δt in STDP is the timescale between the release of ions from their equilibrium positions and their return to equilibrium positions. Similar to the larger timescales of electron-hole dynamics in a defective medium, due to the inter-ionic Coulomb repulsion, the ions disturbed from equilibrium takes more time to come back when the defect density is larger. This trend is evident in the depression curve as well,

shown in Figure 4.6, where the exponential decay of the curve is faster for low-defect density samples.

As evident from Figure 4.4 (a), the response of the neuromorphic device to the voltage pulses is more linear for the samples with low RIR (larger defect density). Nonlinearity in weight update is a topic of wide discussion in the application point of view, where a linear circuit will be simpler than a circuit for nonlinear functions. A nonlinear synaptic weight saturates as the number of pulses increases, which leads to a smaller number of accessible states, while linear weight update has increasing number of states.[181] Therefore, for neuromorphic applications, the conductance of the memristor should be linearly tuned with the voltage pulses. If the conductance modulation is not linear, a peripheral circuit should be added to change the amplitude or width of the applied pulse to obtain the linear modulation of conductivity.[182]

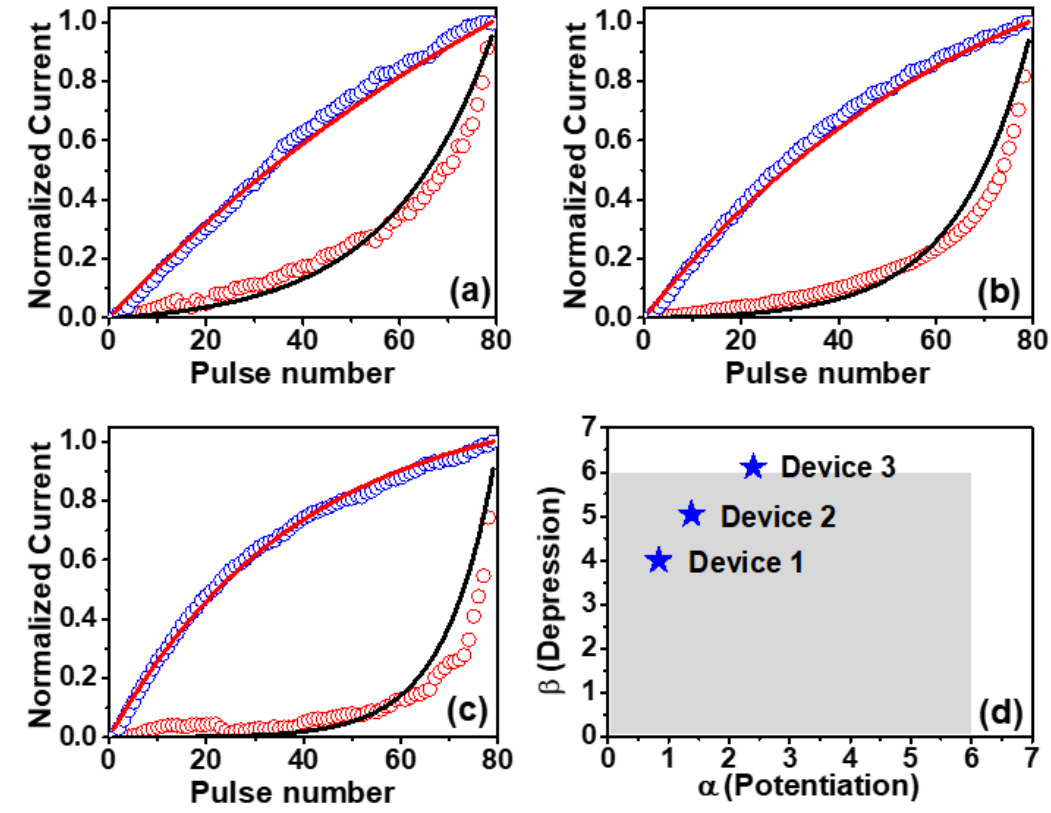

Figure 4.8 The nonlinearity of the potentiation and depression of the different devices with different oxygen vacancy concentrations: (a) for the highest oxygen vacancies (Device 1), (b) for lower oxygen vacancies (Device 2) and (c) for the lowest density of oxygen vacancies (Device 3). (d) plot between the nonlinearity factors for potentiation and depression for these three sets of devices.

Nonlinearity factors (NLF) of the potentiation (α)and depression (β) of these devices were calculated by exponentially fitting the function using the previously reported method.[183] We have taken the potentiation and depression values of series of pulses and normalized those. Theoretical fitting to the experimental data for different devices is shown in figure 4.8. As figure 4.8 shows, the devices with highest amount of oxygen vacancies are having the better linearity than those with less oxygen vacancies. Figure 4.8 (d) shows the plot between the NLF of potentiation (α) and depression (β), for the three sets of devices with different oxygen vacancies. Device 1 has the highest oxygen vacancy density, in the decreasing order to Device 3. Figure 4.8 is a generic representation popularly used for neuromorphic pattern recognition, where the prediction accuracy is highest when the synaptic weight is linear. Maximum nonlinearity for this application is 6 for both potentiation and depression, shown as the shaded area in the figure. As evident from the figure, Device-3 with the lowest defect density does not satisfy the condition for pattern recognition applications since it is highly nonlinear.

Figure 4.8 (a)-(d) show that the nonlinearity of the devices has an interesting correlation with the defect density in it. Further, the potentiation of the devices is more linear than the depression part of the corresponding devices. This could be because the potentiation is caused by the drift-driven mechanism, while the depression is facilitated by drift, diffusion as well as the Coulombic repulsion between the ions. Similar to the STDP measurements shown in Fig. 4 (d), the linearity is simply determined by the response of the ions to the applied voltage pulses. In a medium of relatively large defect density, the system does not reach saturation in potentiation, which is manifested as the linear synaptic response.

4.4 Conclusion

Here we have studied the synaptic responses of the neuromorphic devices comprising BFO with different oxygen concentrations. As the oxygen vacancies increase, the mean leakage current is increasing for devices. The devices with larger defect density exhibit larger synaptic weight, and the STDP shows larger plasticity time constant when the density of the oxygen vacancies is larger. However, when it comes to the linearity of the devices, devices with lower defect densities exhibit high nonlinearity, which could adversely affect the usage of such devices in applications for which linear weight update is required. However, our experiments suggest that the linearity of the devices could be tuned by controlling the oxygen vacancies in the material. This observation could be of importance for a large span of applications of artificial synaptic systems to tune their properties as per the requirements of the applications.

Chapter 5:

Pattern recognition using BFO neuromorphic devices for advanced artificial intelligence.

5.1 Introduction

Chapter 5 delves into Bismuth Ferrite (BFO) neuromorphic devices and their role in pattern recognition. We apply these devices to address practical pattern recognition challenges. Our primary aim in this chapter is to leverage BFO devices for pattern recognition tasks. We employ neural network models, with BFO neuromorphic devices as crucial components in our data processing pipeline. We start by using artificial neural networks (ANNs) to achieve high pattern recognition accuracies. Later, we introduce Convolutional Neural Networks (CNNs), known for their precise pattern extraction and efficiency through fewer training iterations. Our decision to utilize both ANNs and CNNs are of interest in efficiency. CNNs, with their exceptional feature extraction capabilities, hit a balance between pattern recognition accuracy and resource conservation.

Additionally, we explore parallel processing by combining the computational power of multiple neuromorphic devices. This approach enhances efficiency, improving the overall effectiveness of our pattern recognition techniques. Throughout this chapter, we use schematic diagrams to illustrate the hierarchical structure of neural networks and data flow within them. We demonstrate the practicality of BFO-based neuromorphic devices in pattern recognition through an example involving handwritten digit recognition.

Chapter 5 represents a significant milestone in our research journey, highlighting the potential of BFO devices in real-world applications and their contribution to pattern recognition technology.

5.2 Applications of pattern recognition

Applications of pattern recognition in daily life are intervened with gadgets we use, especially with the mobile phone. Advanced applications of artificial intelligence necessitate that intelligent systems have the capability to discern real-world patterns, enabling them to address issues in real-time effectively. When we observe our environment, it becomes evident that AI technologies like face unlock, smart speakers and assistants, AI traffic cameras, and face tagging are increasingly integrated into our daily lives. These innovations rely on pattern recognition to operate effectively in the modern world. We explore the use of pattern recognition to highlight the potential of neuromorphic devices in advanced artificial intelligence.

In this chapter, our primary focus is on training and testing neuromorphic devices for digit recognition tasks. These devices, integrated with electrical circuits and managed by neural networks, are trained using an extensive dataset of numerical digits. Subsequently, they are tasked with recognizing these digits. For both training and testing, we utilized the Modified National Institute of Standards and Technology (MNIST) datasets. This chapter highlights the specific training and testing processes of BFO neuromorphic devices, emphasizing their potential for solving real-world problems.

5.2.1 Recognition of Handwritten digits using the BFO neuromorphic devices.

Recognizing handwritten digits is within the realm of pattern recognition tasks. To accomplish this, one must choose patterns for both training and testing. The MNIST database, an abbreviation for Modified National Institute of Standards and Technology database, serves as a resource of handwritten digits for training and testing image processing systems.[184] This database comprises thousands of distinct handwritten digits. These digits are utilized to train and test machine learning systems. The whole data set contains a total of 70,000 digits among which 60,000 digits were used for training and 10,000 were used for testing. Each digit being a representation of a digit from zero to nine, these digits hence are labelled accordingly. Every digit was standardized into a 28x28 pixel box, with intensity levels ranging from 0 to 256, following a grayscale format.

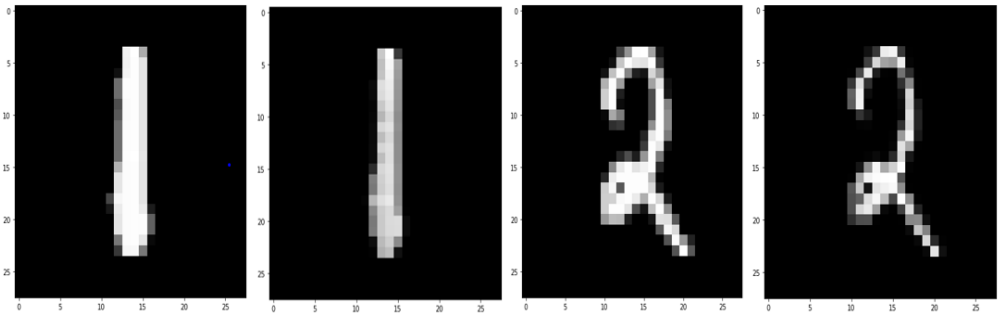

Figure 5.1 A few handwritten digits from MNIST database

MNIST database is generally used to train neural networks. In real world projects that involve machine learning, like digit recognition, a critical process is the training and testing of data sets.[161] This helps in evaluating the learning effectiveness of the system by comparing the accuracy of the output with expected results. MNIST being the benchmark for testing the neural networks, here we use a neural network on the neuromorphic device and test the efficiency of the pattern recognition of the system. The core of this implementation involves a neuromorphic device, which is connected to a source meter unit. This setup is further interfaced with a computer. The computer runs the specialized neural network code, which is responsible for controlling the operations of the neuromorphic device.

Data input is a crucial step in this procedure. Here, relevant data is fed into the neuromorphic device as voltage pulses that mimic the action potentials in biological neurons. The output from this device is measured as an electrical current, which is a direct indicator of the device processing the input data. This output is then analysed for its accuracy and relevance. The neural network, which plays a pivotal role in this process, is structured into three main layers: the input layer, the hidden layer, and the output layer. The input layer is where the data enters into the network. This data is then passed to the hidden layer, which is the computational heart of the network. In the hidden layer, the network assigns different weights to the various input values. These weights are crucial as they determine how much influence each input will have on the final output. The output layer is where the results of the processing are generated. This layer interprets the weighted inputs from the hidden layer and produces an outcome, which is then compared against the expected result.[106]

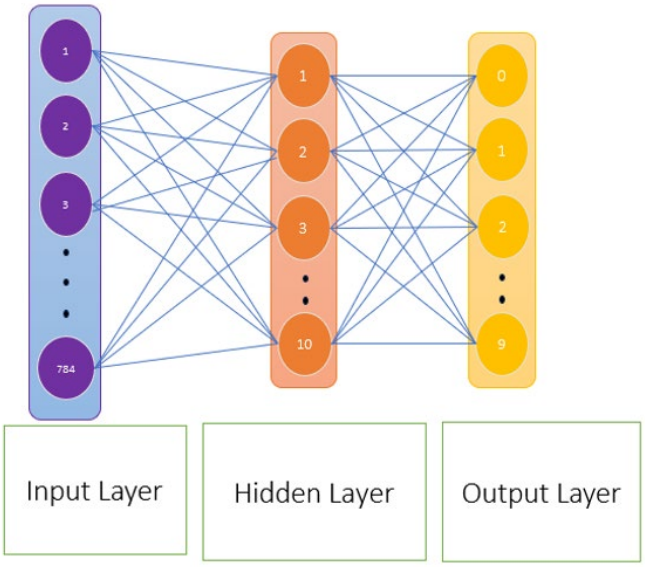

Figure 5.2 The neural network architecture

An iterative process is central to refining the accuracy of the neural network. Each time an input is processed, the network adjusts the weights in an attempt to match the desired outcome. This is done through numerous iterations. If the network's output is not as expected, a loss function is calculated. This function quantifies the difference between the expected result and the actual output.[185] The value derived from the loss function is then used to make adjustments in the initial layers, particularly in the input layer, for subsequent iterations.[186]

This feedback mechanism is critical in neural networks. It allows the system to learn from its errors and gradually improve its accuracy. The goal is to reduce the number of iterations, or epochs, required to achieve a high level of accuracy. Fewer epochs indicate a more efficient learning process, where the network quickly adapts to produce the desired outcomes with minimal data input and processing time. This efficiency is vital in practical applications, where speed and accuracy are essential.[187]

5.3 Artificial Neural Network

Artificial neural network outline has to have feedback. We first discuss how to train and test the device with the artificial neural network, and later we do discuss the convolutional network which has more feature extraction capabilities. [188]

The training and testing of a neuromorphic device using the MNIST dataset for handwritten digit recognition involve several detailed steps:

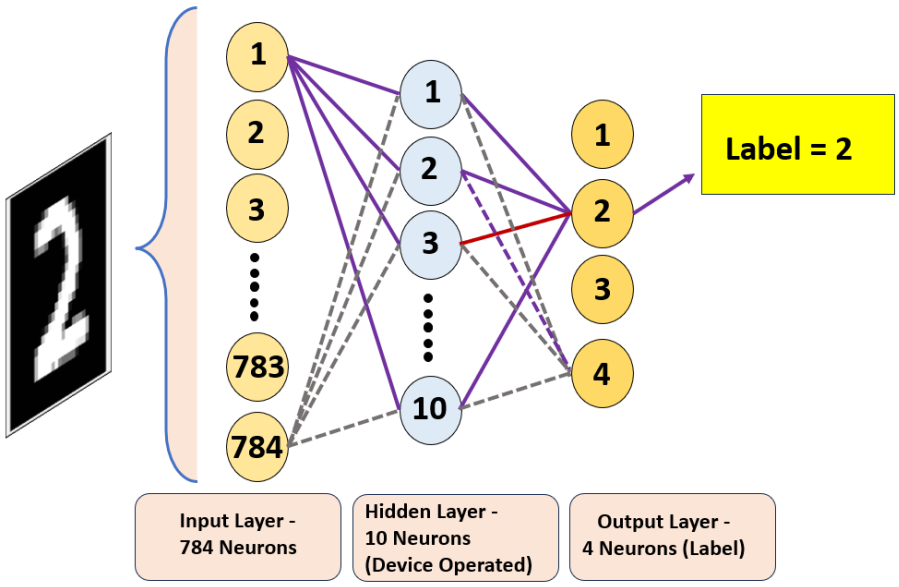

Figure 5.3 ANN distribution diagram

Dataset Overview: The MNIST dataset, a cornerstone in the machine learning field, comprises a vast collection of handwritten digits.[19] Each digit is presented as a 28x28 pixel grayscale image, which, for processing purposes, is converted into a 784-element vector. This transformation facilitates the feeding of these images into a neural network as input.[189]

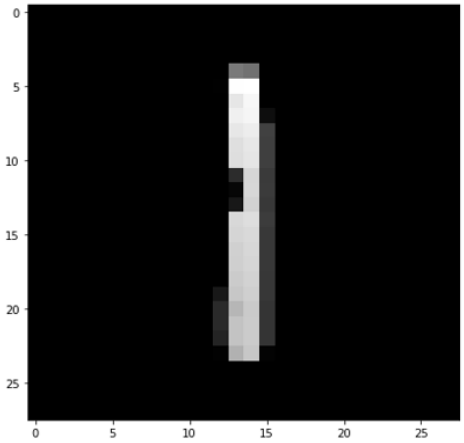

Figure 5.4 MNIST sample data digit 1

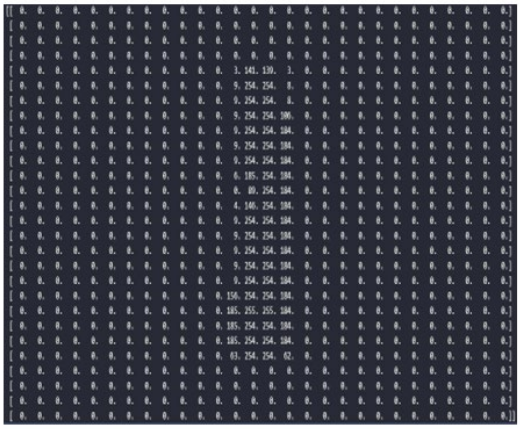

Figure 5.5 MNIST digit 1 intensity.

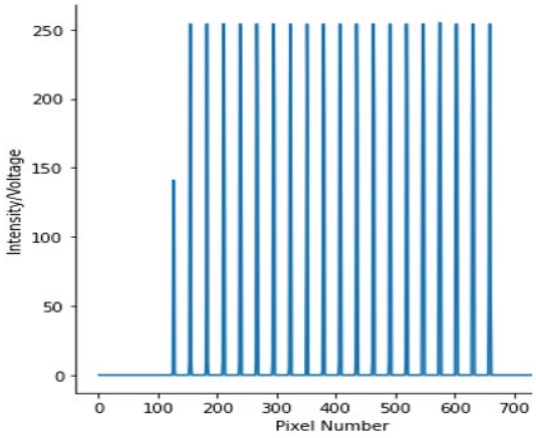

Figure 5.6 MNIST digit 1 pulse intensity.

Neuromorphic Device Set-up: In this specific setup, the neuromorphic device features a layer with 10 hidden nodes, representing a simplified model of neural interactions.

5.3.1 Training Phase:

Input Layer: The training begins with feeding the 784-element vector, representing each digit, into the neuromorphic device. This step is similar to sensory neurons receiving external stimuli in the human brain.

Hidden Layer Processing: These inputs then pass through the 10 nodes in the hidden layer. These nodes act as intermediate neurons, applying various

transformations to the inputs using weights and activation functions. This process determines the extent of influence one neuron has on another.[190]

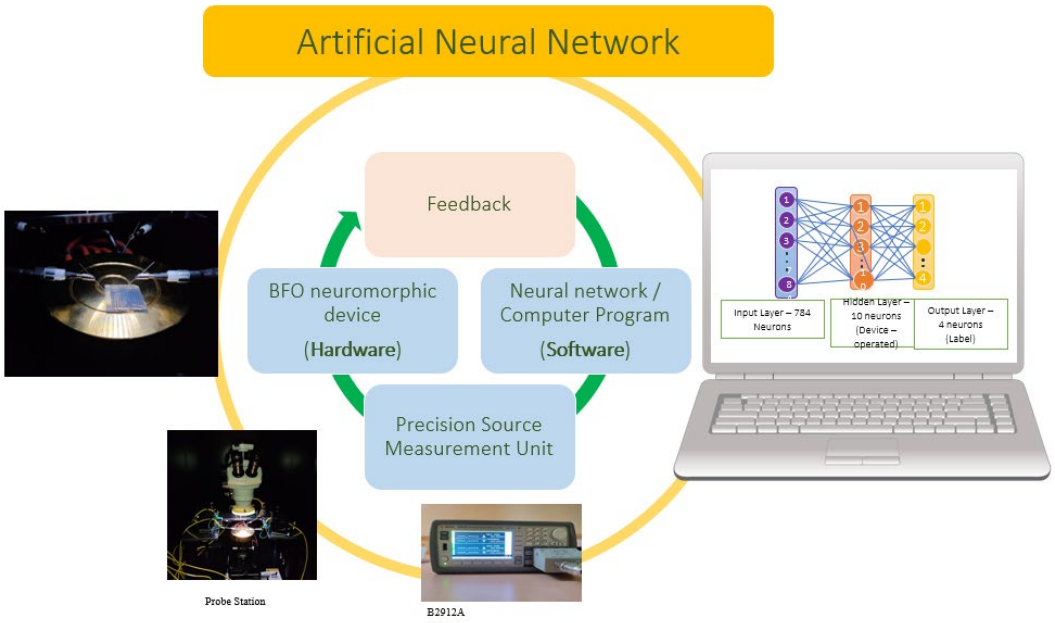

Figure 5.7 Schematics of the Pattern recognition set up

Learning: The device adjusts the synaptic weights—the connections between neurons—based on the input data. The objective is to minimize the error between the network's output and the desired output (the correct digit label). This learning is typically achieved using backpropagation algorithms and optimization techniques like gradient descent.[181]

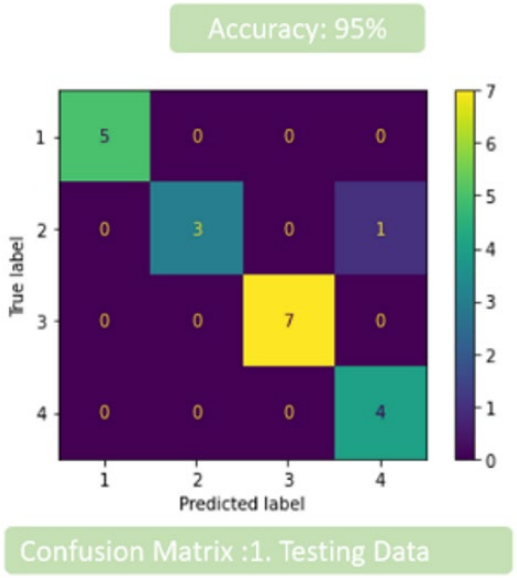

Figure 5.8 Confusion Matrix for testing (ANN)

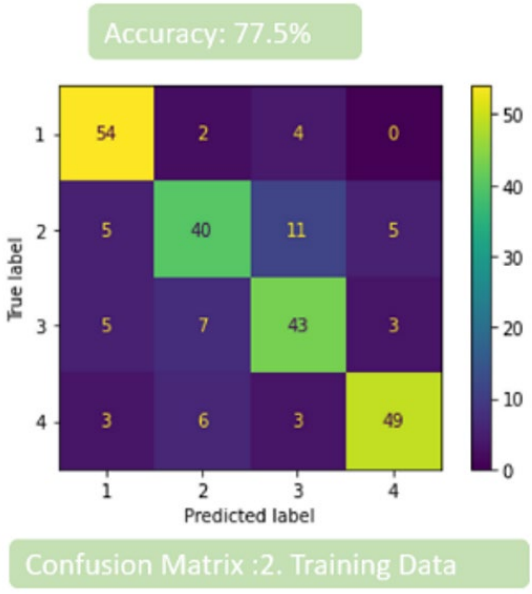

Figure 5.9 Confusion Matrix for training (ANN)

5.3.2 Testing Phase:

After training, the device is exposed to new, unseen images from the MNIST dataset. This phase mirrors the training process, except that the synaptic weights are no longer adjusted. The network makes predictions by processing the input through the trained network and identifying which output neuron is most activated.[191]

5.3.3 Evaluation:

The effectiveness of the neuromorphic device is measured by its accuracy in recognizing digits during the testing phase. The device's performance is compared to the known labels of the test images.

This entire process demonstrates the impressive capabilities of neuromorphic devices in tasks like pattern recognition. By mimicking the brain's architecture, these devices offer enhanced computational efficiency and reduced power consumption, making them highly suitable for complex tasks in machine learning and artificial intelligence.[112]

5.4 Convolutional Neural Network (CNN)

Convolutional Neural Network (CNN) is used to train and recognize digits from the MNIST dataset. When we understand CNN, these are specialized for processing data with a grid-like topology, like images. They are particularly effective for image recognition tasks.[192] CNN can automatically and adaptively learn spatial hierarchies of features.[108] Hence, CNN are better options as they can extract features because of this. MNIST Dataset is the dataset that consists of grayscale images of handwritten digits, each 28x28 pixels. For CNN, each image is input as a 28x28 matrix of pixel values.

The CNN Architecture for MNIST digit recognition contains a few layers. The first layer is the input layer. The input layer takes the 28x28 pixel image. Next, we have Convolutional Layers, which apply a number of filters to the input. Each filter detects different features like edges, corners, etc. The result is a feature map that gives the network spatial information about the image.[193]

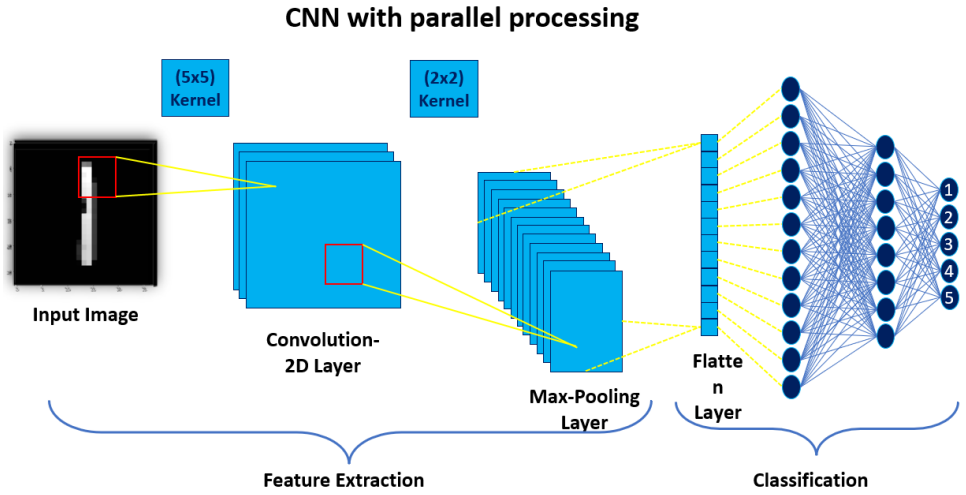

Figure 5.10 Pictorial representation of the CNN Architecture

Rectified linear unit (ReLU) introduces nonlinearity, allowing the network to handle complex patterns.

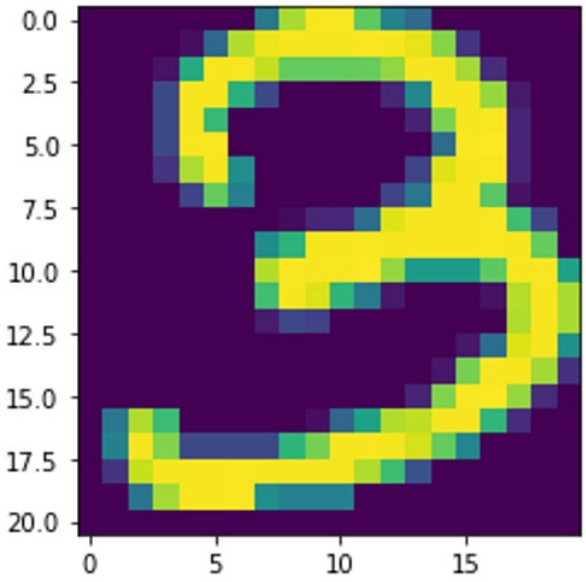

Figure 5.11 A digit 3 as input

Pooling Layer reduces the spatial size of the representation, lowering the amount of computation and weights. It also helps in making the detection of features invariant to scale and orientation changes.

Fully Connected Layer: After several convolutional and pooling layers, the high-level reasoning is done through fully connected layers. The final layer's output size corresponds to the number of classes in this case, four (one for each digit).

Training Convolutional Neural Networks (CNNs) involves a process of learning that can be broken down into two main phases: forward propagation and backpropagation.

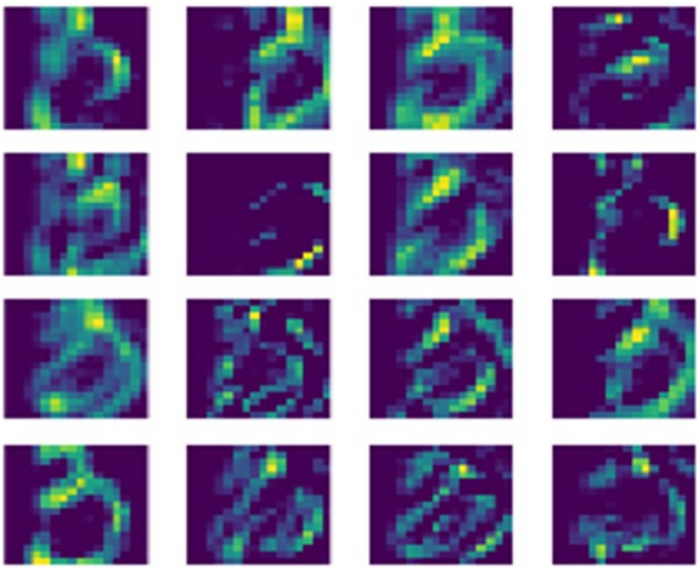

Figure 5.12 Feature Maps Extracted by 2D-Convolution

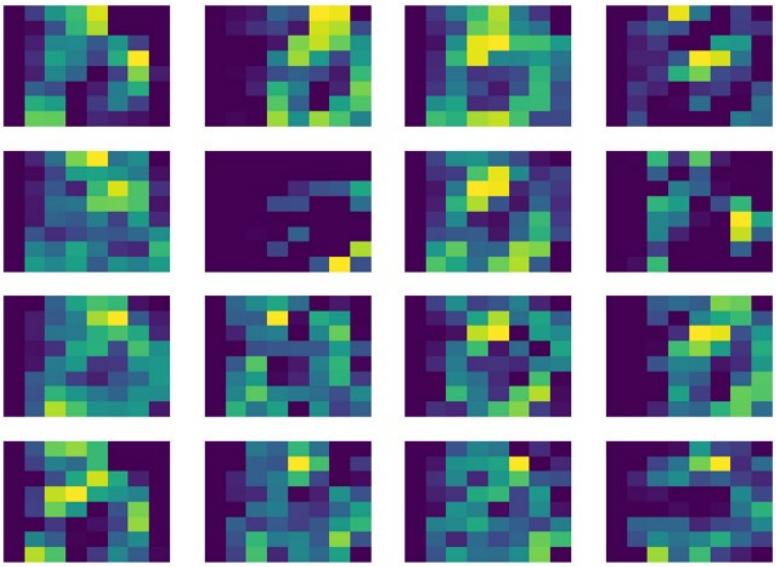

Figure 5.13 Feature Maps after max-pooling layer

Forward Propagation: This is the initial phase where CNN starts the learning process. It begins with the network taking an input, which is typically an image in the case of CNNs. This image is then fed through various layers of the network. Each layer consists of filters and performs specific operations, such as identifying edges, textures, or patterns in the image. As the image data passes through these layers, the network extracts, and processes features, gradually building a more abstract representation of the input. This process continues until the network makes a prediction based on the cumulative analysis of the data by all these layers.

Back propagation: Once the network has made a prediction, the next step is to evaluate the accuracy of this prediction. This is done by comparing the predicted output of the network against the actual label or ground truth associated with the input image. The difference between the prediction and the actual label is quantified as an error or loss. Backpropagation is the process where the CNN adjusts its internal parameters to minimize this error. It involves computing the gradient of the loss function with respect to each weight in the network using calculus and then updating the weights in a direction that reduces the loss. Optimization algorithms, such as stochastic gradient descent, are employed to perform these updates efficiently. This process of adjusting the weights continues iteratively, with the network repeatedly going through cycles of forward propagation and backpropagation, each time learning from the errors made in the previous cycle, until the network's predictions are sufficiently accurate or other stopping criteria are met.

Figure 5.14 shows the training of the neuromorphic device with the CNN. Neural network controls the electronics which are connected to the BFO neuromorphic device. The feature of the digit is extracted and prepared for flattening. [194] Flattened data are fed into the neural network through the input layer. The hidden layer adjusts the conductivity of the device for different patterns and hence the features. The final output layer directs to the element of the set.

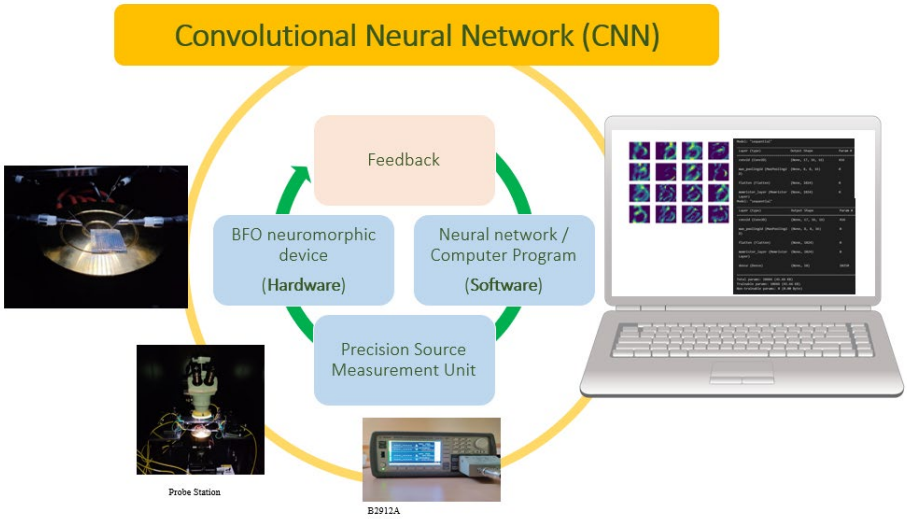

Figure 5.14 Sketch of training with Convolutional neural network

Testing the CNN involves a critical evaluation phase after its training. During this phase, the CNN is exposed to images from the MNIST dataset that it has not encountered during the training process. This step is crucial as it aims to assess CNN's ability to apply its learned knowledge from the training data to new, unseen data. Essentially, this testing phase is designed to evaluate the network's capacity for generalization.[186]

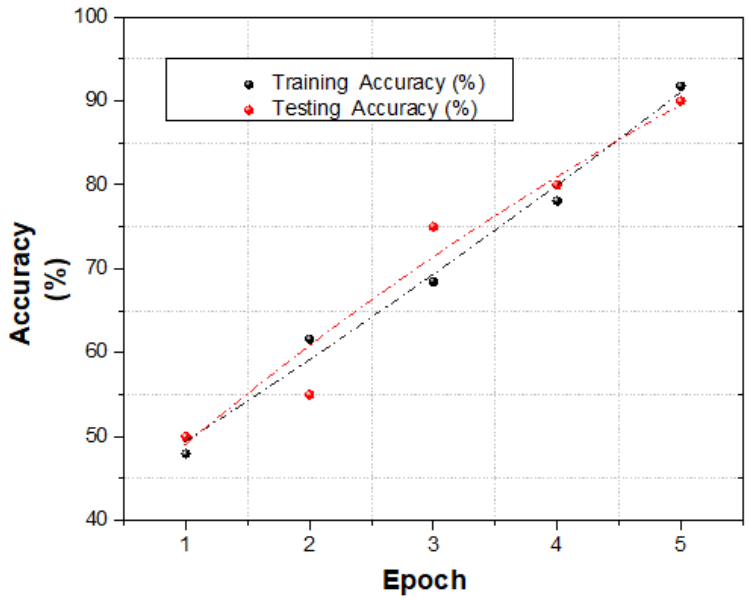

Figure 5.15 Accuracy of training and testing in CNN model

In the context of evaluation, the performance of CNN is primarily measured using specific metrics, with accuracy being a key indicator. Accuracy in this scenario refers

to the proportion of digits from the MNIST dataset that the CNN correctly identifies. A high accuracy rate would indicate that the network has effectively learned from the training data and is capable of accurately recognizing and classifying new images that it wasn't explicitly trained on. This metric is essential for understanding the effectiveness and reliability of CNN in practical applications. CNNs are powerful for tasks like digit recognition because they can learn and identify spatial hierarchies in images, making them competent at understanding the complex patterns in handwritten digits.

5.5 Parallel Processing of Devices

The creation of a neuromorphic device is the foundational step in the development of neuromorphic technology. This initial stage focuses on constructing an individual unit, which is a critical component of the broader system. However, the real challenge and the key factor lye in the architecture: specifically, how to efficiently assemble millions of these units together. This architectural design is pivotal because it enables the distribution of computational tasks across multiple devices, thereby enhancing processing speed and efficiency.[195]

In neuromorphic technology, one of our primary objectives is to facilitate parallel processing – a method where multiple tasks are processed simultaneously, as opposed to sequentially. This approach significantly accelerates computational processes and is more akin to the functioning of the human brain. By employing multiple neuromorphic devices in tandem, we can divide the workload among them, thereby achieving this goal of parallel processing. [196]

Here we demonstrate this concept of parallel processing by integrating two neuromorphic devices simultaneously. To achieve this, we utilized two force channels, one on each of the two devices, while maintaining a common gate. This setup of keeping a shared gate and probing the two devices independently is effectively equivalent to connecting two identical devices in parallel. Such a configuration enhances the overall processing capabilities of the system.[184]

The method of probing these devices and their parallel configuration is visually illustrated in the figure 5.16. This pictorial representation provides a clear understanding of how the devices are interconnected and operate in unison, thereby showcasing the practical application of parallel processing in neuromorphic technology.

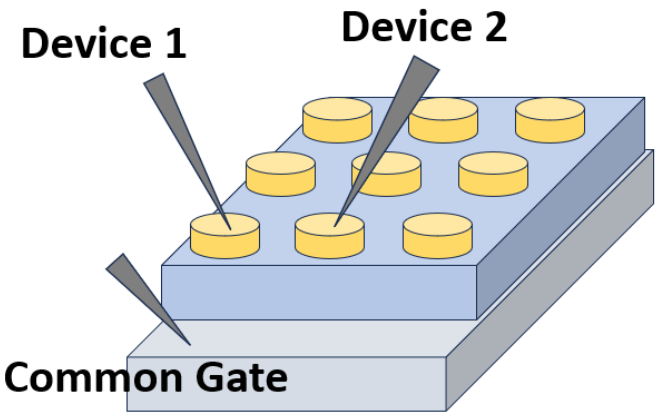

Figure 5.16 Sketch showing the parallel processing using two identical neuromorphic devices

Since the neuromorphic devices are closely adjacent, it's reasonable to assume that any variations between them are minimal and can largely be disregarded. This similarity allows for an effective strategy when combining, or "clubbing," two neuromorphic devices: the goal is to decrease processing duration while maintaining high efficiency. Upon integrating these devices, we observed that their efficiency remained consistent, and notably, the accuracy of the tasks they performed was almost unchanged.

To further explore this synergy, we divided a single task between the two devices. This division resulted in a significant reduction in overall processing time—halving it, in fact—since each device handled a part of the task simultaneously. This outcome highlights the primary advantage of using multiple devices: by employing parallel processing, where tasks are distributed and processed concurrently, we can achieve a substantial decrease in the time required to complete complex operations, enhancing overall productivity without sacrificing performance quality.[197]

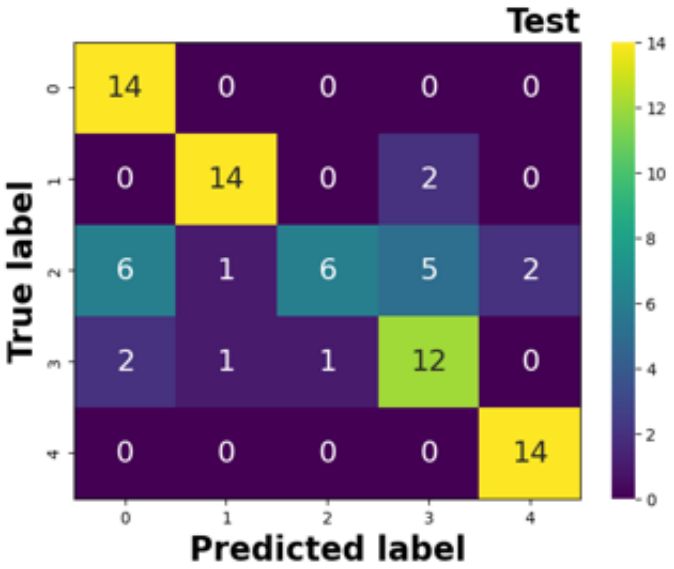

Figure 5.17 Confusion matrix for the parallel processing doublet

In the provided figure 5.17, we present a detailed confusion matrix for a pair of neuromorphic devices operating in a parallel processing configuration. This setup is instrumental in illustrating the integration capabilities of these devices. Confusion matrix is read with true label in the rows against the predicted label of the columns in the matrix. That is when a true label is one, then the most accurate prediction is when the predicted label also is one, for all the test data. Similarly, across the other true values, predicted label should give total number of test labels corresponding to the true values. However, we see that the predicted labels and true values are not matching every time. That shows that the variation in prediction from the true values for the device.[198]

When tested using a Convolutional Neural Network (CNN), the accuracy of the system reaches approximately 85%. This high level of accuracy underscores the effectiveness of parallel processing with two neuromorphic devices, highlighting their potential for collaborative operations. [199]

The significance of parallel processing in this context cannot be overstated. It not only demonstrates the current capabilities of neuromorphic devices but also points towards a promising future where such devices can be seamlessly integrated to tackle complex computational problems. The figure 5.18 further compares the testing and training accuracy of these neuromorphic devices when they are linked in a parallel processing arrangement. Our observations indicate that the devices exhibit commendable efficiency in this setup. This efficiency is a crucial indicator of the

potential advancements in the field of neuromorphic computing, suggesting an optimistic outlook for the integration and performance of these devices in solving advanced computational tasks.

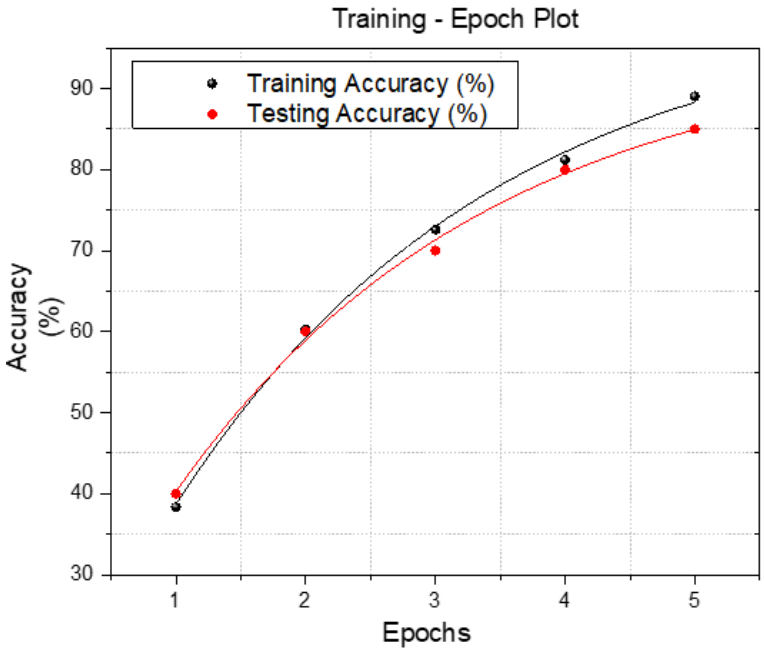

Figure 5.18 Accuracy curve for the pair in parallel processing

Here in figure 5.18, we see that the accuracy of recognition of the MNIST digits when processed with two identical devices are depicted. The training accuracy is around 92%, while the testing accuracy is 90%. The accuracy of the recognition is concerned with the fact that there could be existence of individual dissimilarities among the devices, the total work is divided to both devices, so that allocation of the process can also be question of deep study for proper understanding.

5.6 Conclusions

In Chapter 5 of our thesis, we explored the use of Bismuth Ferrite (BFO) neuromorphic devices for pattern recognition. This chapter is critical as it applies the theoretical concepts and material properties from earlier chapters to real-world problems. Our approach focused on the full potential of BFO devices in pattern recognition, integrating neural network models with BFO devices at the core of our data processing.

We began with artificial neural networks (ANNs) for high accuracy in pattern recognition tasks and then moved to Convolutional Neural Networks (CNNs) for their efficiency in complex pattern extraction with less training. We chose ANNs and CNNs for their balance of efficiency and effectiveness.

CNNs showed strength in feature extraction, optimizing computational resources and time. We also employed parallel processing with multiple neuromorphic devices, reducing execution time and increasing efficiency. Overall, Chapter 5 highlights the potential of BFO devices in pattern recognition, setting the stage for the final chapter of the thesis, where we explore wider implications and future directions of our research.

Chapter 6:

Conclusion and Future Scope

This dissertation has taken a profound journey into the realm of neuromorphic technology, a field poised at the intersection of hardware development and artificial intelligence. At the outset, it recognized the urgent need for hardware that could evolve in tandem with the rapidly advancing algorithms of AI, a need that neuromorphic technology is uniquely positioned to fulfil. The focus on Bismuth Iron Oxide ($BiFeO_3$ or BFO) emerged from its intriguing multifunctional ferroic properties, which were hypothesized to contribute significantly to neuromorphic applications.

The cornerstone of this research was the development of a novel reactive Pulsed Laser Deposition (PLD) system, which I personally engineered and optimized in our laboratory. This system was critical for the deposition of high-quality BFO thin films, which are essential for the reliable performance of neuromorphic devices. The choice of a simple metal-insulator-metal (MIM) structure for the devices, utilizing Fluorine-doped tin oxide (FTO) as the bottom electrode and gold as the top electrode, was driven by the aim to streamline fabrication while ensuring optimal functional characteristics.

Throughout this research, the neuromorphic properties of these devices were thoroughly investigated. Special attention was given to the nonlinearity of synaptic weight updates—a crucial aspect for mimicking the human brain's ability to learn from variable inputs. We explored how different parameters, such as oxygen vacancies, influenced these synaptic dynamics. It was found that varying oxygen vacancy levels not only affected the device's response curve but also enhanced its application in complex pattern recognition tasks, such as those involving the MNIST dataset for handwritten digits.

Moreover, the integration of multiple neuromorphic devices demonstrated a potential reduction in operational times, suggesting that parallel processing in neuromorphic hardware could mimic the brain's efficiency. This capability was exemplified in experiments where combining two devices halved the time required for pattern recognition tasks, thereby increasing computational efficiency significantly.

As we look to the future, several avenues for further research and development present themselves. First, the integration of BFO-based neuromorphic devices with conventional CMOS technology stands out as a promising direction. This integration could potentially lead to the creation of more compact, efficient, and powerful neuromorphic systems. Exploring this possibility would involve addressing the challenges of material compatibility and interface optimization to ensure seamless functionality across different technological platforms.

Additionally, there is substantial scope for enhancing the material properties and device architectures based on BFO. Future studies could focus on refining the deposition processes to achieve even higher quality thin films or experimenting with different electrode materials to optimize performance and durability. Such advancements could pave the way for BFO devices that not only excel in pattern recognition but are also capable of performing more diverse cognitive tasks such as real-time decision-making and complex problem-solving.

Beyond the technical enhancements, the broader implications of this technology for AI and cognitive computing are immense. As neuromorphic devices become more sophisticated, they could increasingly contribute to areas such as autonomous systems, robotics, and personalized medicine, where adaptive and efficient processing of vast amounts of data is crucial.

In conclusion, this thesis has not only demonstrated the practical capabilities of BFO in neuromorphic applications but also highlighted the extensive potential for future innovations in this exciting area. The groundwork laid by this research is expected to inspire continued advancements that will push the boundaries of what neuromorphic technology can achieve, shaping the future of artificial intelligence and computing technology.

References

1. S. Kunwar, Z. Jernigan, Z. Hughes, C. Somodi, M. D. Saccone, F. Caravelli, P. Roy, D. Zhang, H. Wang, Q. Jia, J. L. MacManus-Driscoll, G. Kenyon, A. Sornborger, W. Nie, and A. Chen, Adv. Intell. Syst. **5**, 2300035 (2023).

2. D. V. Christensen, R. Dittmann, B. Linares-Barranco, A. Sebastian, M. Le Gallo, A. Redaelli, S. Slesazeck, T. Mikolajick, S. Spiga, S. Menzel, I. Valov, G. Milano, C. Ricciardi, S.-J. Liang, F. Miao, M. Lanza, T. J. Quill, S. T. Keene, A. Salleo, J. Grollier, D. Marković, A. Mizrahi, P. Yao, J. J. Yang, G. Indiveri, J. P. Strachan, S. Datta, E. Vianello, A. Valentian, J. Feldmann, X. Li, W. H. P. Pernice, H. Bhaskaran, S. Furber, E. Neftci, F. Scherr, W. Maass, S. Ramaswamy, J. Tapson, P. Panda, Y. Kim, G. Tanaka, S. Thorpe, C. Bartolozzi, T. A. Cleland, C. Posch, S. Liu, G. Panuccio, M. Mahmud, A. N. Mazumder, M. Hosseini, T. Mohsenin, E. Donati, S. Tolu, R. Galeazzi, M. E. Christensen, S. Holm, D. Ielmini, and N. Pryds, Neuromorphic Comput. Eng. **2**, 022501 (2022).

3. C. D. Wright, P. Hosseini, and J. A. V. Diosdado, Adv. Funct. Mater. **23**, 2248 (2013).

4. A. Sebastian, M. Le Gallo, and E. Eleftheriou, J. Phys. Appl. Phys. **52**, 443002 (2019).

5. G. E. Moore, Proc. IEEE **86**, (1998).

6. E. Linn, R. Rosezin, S. Tappertzhofen, U. Böttger, and R. Waser, Nanotechnology **23**, 305205 (2012).

7. J. D. Kendall and S. Kumar, Appl. Phys. Rev. **7**, 029901 (2020).

8. C. Prakash, L. R. Gupta, A. Mehta, H. Vasudev, R. Tominov, E. Korman, A. Fedotov, V. Smirnov, and K. K. Kesari, Mater. Adv. **4**, 5882 (2023).

9. J. Végh, Brain Inform. **6**, 4 (2019).

10. R. P. Seisyan, Tech. Phys. **56**, 1061 (2011).

11. S. V. Garimella, T. Persoons, J. A. Weibel, and V. Gektin, IEEE Trans. Compon. Packag. Manuf. Technol. **7**, 1191 (2017).

12. V. Saxena, X. Wu, and K. Zhu, in *2018 IEEE Int. Symp. Circuits Syst. ISCAS* (IEEE, Florence, 2018), pp. 1–5.

13. C. Mead, Nat. Electron. **3**, 434 (2020).

14. J. D. Kendall and S. Kumar, Appl. Phys. Rev. **7**, 011305 (2020).

15. D. Marković, A. Mizrahi, D. Querlioz, and J. Grollier, Nat. Rev. Phys. **2**, 499 (2020).

16. D. G. Roe, S. Kim, Y. Y. Choi, H. Woo, M. S. Kang, Y. J. Song, J. Ahn, Y. Lee, and J. H. Cho, Adv. Mater. **33**, 2007782 (2021).

17. E. E. Tsur, *Neuromorphic Engineering: The Scientist's, Algorithm Designer's and Computer Architect's Perspectives on Brain-Inspired Computing*, First edition (CRC Press, Boca Raton, 2021).

18. N. Mohta, A. Rao, N. Remesh, R. Muralidharan, and D. N. Nath, RSC Adv. **11**, 36901 (2021).

19. Y. Fu, C.-C. Huang, Z.-Y. Lin, C.-C. Lee, and J.-C. Wang, IEEE Trans. Electron Devices **70**, 4473 (2023).

20. V. Milo, G. Malavena, C. Monzio Compagnoni, and D. Ielmini, Materials **13**, 166 (2020).

21. K. He, C. Wang, Y. He, J. Su, and X. Chen, Chem. Rev. **123**, 13796 (2023).

22. W. Gerstner, R. Ritz, and J. L. Van Hemmen, Biol. Cybern. **69**, 503 (1993).

23. J. J. Langille and R. E. Brown, Front. Syst. Neurosci. **12**, 52 (2018).

24. J. Cohen, J. Appl. Phys. **35**, 3056 (1964).
25. R. Yang, Chin. Phys. B **29**, 097305 (2020).
26. C. Sung, H. Hwang, and I. K. Yoo, J. Appl. Phys. **124**, 151903 (2018).
27. Y. Li, Y. Zhong, J. Zhang, L. Xu, Q. Wang, H. Sun, H. Tong, X. Cheng, and X. Miao, Sci. Rep. **4**, 4906 (2014).
28. G. W. Burr, R. M. Shelby, A. Sebastian, S. Kim, S. Kim, S. Sidler, K. Virwani, M. Ishii, P. Narayanan, A. Fumarola, L. L. Sanches, I. Boybat, M. Le Gallo, K. Moon, J. Woo, H. Hwang, and Y. Leblebici, Adv. Phys. X **2**, 89 (2017).
29. P.-Y. Chen and S. Yu, IEEE Des. Test **36**, 31 (2019).
30. J. Del Valle, J. G. Ramírez, M. J. Rozenberg, and I. K. Schuller, J. Appl. Phys. **124**, 211101 (2018).
31. I. Boybat, M. Le Gallo, S. R. Nandakumar, T. Moraitis, T. Parnell, T. Tuma, B. Rajendran, Y. Leblebici, A. Sebastian, and E. Eleftheriou, Nat. Commun. **9**, 2514 (2018).
32. C. Bengel, K. Zhang, J. Mohr, T. Ziegler, S. Wiefels, R. Waser, D. Wouters, and S. Menzel, Front. Electron. Mater. **3**, 1061269 (2023).
33. P. Balakrishna Pillai and M. M. De Souza, ACS Appl. Mater. Interfaces **9**, 1609 (2017).
34. D. Kim and J.-S. Lee, NPG Asia Mater. **12**, 62 (2020).
35. A. S. Sokolov, Y.-R. Jeon, S. Kim, B. Ku, and C. Choi, NPG Asia Mater. **11**, 5 (2019).
36. S. Bhattacharjee, R. Wigchering, H. G. Manning, John. J. Boland, and P. K. Hurley, Sci. Rep. **10**, 12178 (2020).
37. T. Serrano-Gotarredona, T. Masquelier, T. Prodromakis, G. Indiveri, and B. Linares-Barranco, Front. Neurosci. **7**, (2013).
38. P. J. Srinidhi, T. R. Yashaswini, N. Uttunga, S. A. Ali, and M. R. Ahmed, in *2017 Int. Conf. Intell. Comput. Control Syst. ICICCS* (IEEE, Madurai, 2017), pp. 1105–1110.
39. L. Xu, H. Xiong, Z. Fu, M. Deng, S. Wang, J. Zhang, L. Shang, K. Jiang, Y. Li, L. Zhu, L. He, Z. Hu, and J. Chu, Phys. Rev. Appl. **16**, 044049 (2021).
40. C. Yang, D. Shang, N. Liu, E. J. Fuller, S. Agrawal, A. A. Talin, Y. Li, B. Shen, and Y. Sun, Adv. Funct. Mater. **28**, 1804170 (2018).
41. D. M. Bishop, P. Solomon, S. Kim, J. Tang, J. Tersoff, T. Todorov, M. Copel, J. Collins, K. T. Lee, S. Shin, W. Haensch, and J. Rozen, in *Ext. Abstr. 2018 Int. Conf. Solid State Devices Mater.* (The Japan Society of Applied Physics, Hongo Campus, The University of Tokyo, Tokyo, Japan, 2018).
42. D. Ivanov, A. Chezhegov, M. Kiselev, A. Grunin, and D. Larionov, Front. Neurosci. **16**, 959626 (2022).
43. C. D. Schuman, S. R. Kulkarni, M. Parsa, J. P. Mitchell, P. Date, and B. Kay, Nat. Comput. Sci. **2**, 205 (2022).
44. D. Kuzum, R. G. D. Jeyasingh, S. Yu, and H.-S. P. Wong, IEEE Trans. Electron Devices **59**, 3489 (2012).
45. S. Choi, J. Yang, and G. Wang, Adv. Mater. **32**, 2004659 (2020).
46. Z. Wang, L. Wang, M. Nagai, L. Xie, M. Yi, and W. Huang, Adv. Electron. Mater. **3**, 1600510 (2017).
47. Y. Zhu, H. Mao, Y. Zhu, X. Wang, C. Fu, S. Ke, C. Wan, and Q. Wan, Int. J. Extreme Manuf. **5**, 042010 (2023).
48. R. Islam, H. Li, P.-Y. Chen, W. Wan, H.-Y. Chen, B. Gao, H. Wu, S. Yu, K. Saraswat, and H.-S. Philip Wong, J. Phys. Appl. Phys. **52**, 113001 (2019).

49. L. Camuñas-Mesa, B. Linares-Barranco, and T. Serrano-Gotarredona, Materials **12**, 2745 (2019).

50. F. Pavanello, E. I. Vatajelu, A. Bosio, T. Van Vaerenbergh, P. Bienstman, B. Charbonnier, A. Carpegna, S. Di Carlo, and A. Savino, (2023).

51. S. Jiang, S. Nie, Y. He, R. Liu, C. Chen, and Q. Wan, Mater. Today Nano **8**, 100059 (2019).

52. J. H. Baek, K. J. Kwak, S. J. Kim, J. Kim, J. Y. Kim, I. H. Im, S. Lee, K. Kang, and H. W. Jang, Nano-Micro Lett. **15**, 69 (2023).

53. G. Dayal and K. B. Jinesh, ACS Appl. Electron. Mater. **4**, 592 (2022).

54. K. Udaya Mohanan, Nanomaterials **14**, 527 (2024).

55. W. Huang, H. Zhang, Z. Lin, P. Hang, and X. Li, Crystals **14**, 69 (2024).

56. S. R. Nandakumar, M. Le Gallo, I. Boybat, B. Rajendran, A. Sebastian, and E. Eleftheriou, J. Appl. Phys. **124**, 152135 (2018).

57. S. Jain, A. Ranjan, K. Roy, and A. Raghunathan, IEEE Trans. Very Large Scale Integr. VLSI Syst. **26**, 470 (2018).

58. Z. Hu, Q. Li, M. Li, Q. Wang, Y. Zhu, X. Liu, X. Zhao, Y. Liu, and S. Dong, Appl. Phys. Lett. **102**, 102901 (2013).

59. Y. Noguchi, H. Matsuo, Y. Kitanaka, and M. Miyayama, Sci. Rep. **9**, 4225 (2019).

60. S.-H. Kuk, S. Han, D. H. Lee, B. H. Kim, J. Shim, M. H. Park, J.-H. Han, and S.-H. Kim, IEEE Electron Device Lett. **44**, 36 (2023).

61. H. Kwak, N. Kim, S. Jeon, S. Kim, and J. Woo, Nano Converg. **11**, 9 (2024).

62. In *2020 IEEE 15th Int. Conf. Solid-State Integr. Circuit Technol. ICSICT* (IEEE, Kunming, 2020), pp. 1–47.

63. X. Duan, Z. Cao, K. Gao, W. Yan, S. Sun, G. Zhou, Z. Wu, F. Ren, and B. Sun, Adv. Mater. **36**, 2310704 (2024).

64. V. K. Sangwan and M. C. Hersam, Nat. Nanotechnol. **15**, 517 (2020).

65. C. Feng, W. Wu, H. Liu, J. Wang, H. Wan, G. Ma, and H. Wang, Nanomaterials **13**, 2720 (2023).

66. R. Zhang, R. Su, C. Shen, R. Xiao, W. Cheng, and X. Miao, Sensors **23**, 8838 (2023).

67. M.-K. Kim, Y. Park, I.-J. Kim, and J.-S. Lee, iScience **23**, 101846 (2020).

68. S. Oh, H. Hwang, and I. K. Yoo, APL Mater. **7**, 091109 (2019).

69. B. Sun, G. Zhou, L. Sun, H. Zhao, Y. Chen, F. Yang, Y. Zhao, and Q. Song, Nanoscale Horiz. **6**, 939 (2021).

70. S. Boyn, J. Grollier, G. Lecerf, B. Xu, N. Locatelli, S. Fusil, S. Girod, C. Carrétéro, K. Garcia, S. Xavier, J. Tomas, L. Bellaiche, M. Bibes, A. Barthélémy, S. Saïghi, and V. Garcia, Nat. Commun. **8**, 14736 (2017).

71. R. Guo, L. You, Y. Zhou, Z. Shiuh Lim, X. Zou, L. Chen, R. Ramesh, and J. Wang, Nat. Commun. **4**, 1990 (2013).

72. B.-B. Tian, N. Zhong, and C.-G. Duan, Chin. Phys. B **29**, 097701 (2020).

73. L. Zhao, H. Fang, J. Wang, F. Nie, R. Li, Y. Wang, and L. Zheng, Appl. Phys. Lett. **124**, 030501 (2024).

74. J. P. B. Silva, R. Alcala, U. E. Avci, N. Barrett, L. Bégon-Lours, M. Borg, S. Byun, S.-C. Chang, S.-W. Cheong, D.-H. Choe, J. Coignus, V. Deshpande, A. Dimoulas, C. Dubourdieu, I. Fina, H. Funakubo, L. Grenouillet, A. Gruverman, J. Heo, M. Hoffmann, H. A. Hsain, F.-T. Huang, C. S. Hwang, J. Íñiguez, J. L. Jones, I. V. Karpov, A. Kersch, T. Kwon, S. Lancaster, M. Lederer, Y. Lee, P. D. Lomenzo, L. W. Martin, S. Martin, S. Migita, T. Mikolajick, B. Noheda, M. H. Park, K. M. Rabe, S. Salahuddin, F. Sánchez, K. Seidel, T. Shimizu, T. Shiraishi, S. Slesazeck, A. Toriumi,

H. Uchida, B. Vilquin, X. Xu, K. H. Ye, and U. Schroeder, APL Mater. **11**, 089201 (2023).

75. S. H. Park, H. J. Lee, M. H. Park, J. Kim, and H. W. Jang, J. Phys. Appl. Phys. **57**, 253002 (2024).

76. A. Bogusz, T. You, D. Blaschke, A. Scholz, Y. Shuai, W. Luo, N. Du, D. Burger, I. Skorupa, O. G. Schmidt, and H. Schmidt, in *2013 Int. Semicond. Conf. Dresd. - Grenoble ISCDG* (IEEE, Dresden, Germany, 2013), pp. 1–4.

77. J. Cha, J. Ahn, and K. Lee, J. Korean Phys. Soc. **54**, 844 (2009).

78. A. Roy, R. Gupta, and A. Garg, Adv. Condens. Matter Phys. **2012**, 1 (2012).

79. H.-U. Krebs, M. Weisheit, J. Faupel, E. Süske, T. Scharf, C. Fuhse, M. Störmer, K. Sturm, M. Seibt, H. Kijewski, D. Nelke, E. Panchenko, and M. Buback, in *Adv. Solid State Phys.*, edited by B. Kramer (Springer Berlin Heidelberg, Berlin, Heidelberg, 2003), pp. 505–518.

80. C. Himcinschi, I. Vrejoiu, M. Friedrich, L. Ding, C. Cobet, N. Esser, M. Alexe, and D. R. T. Zahn, Phys. Status Solidi C **7**, 296 (2010).

81. A. Mishra, V. Sharma, and B. K. Kuanr, IEEE Trans. Electron Devices **64**, 5087 (2017).

82. T. Yang, J. Wei, Y. Guo, Z. Lv, Z. Xu, and Z. Cheng, ACS Appl. Mater. Interfaces **11**, 23372 (2019).

83. G. Dayal and K. B. Jinesh, Appl. Phys. A **129**, 777 (2023).

84. H. Wang, J. Huang, X. Sun, J. Jian, J. Liu, and H. Wang, RSC Adv. **10**, 40229 (2020).

85. Z. Chai, P. Freitas, W. Zhang, F. Hatem, J. F. Zhang, J. Marsland, B. Govoreanu, L. Goux, and G. S. Kar, IEEE Electron Device Lett. **39**, 1652 (2018).

86. K. Aboumerhi, A. Güemes, H. Liu, F. Tenore, and R. Etienne-Cummings, J. Neural Eng. **20**, 041004 (2023).

87. A. Vitale, E. Donati, R. Germann, and M. Magno, IEEE Sens. J. **22**, 19490 (2022).

88. Y. Hajjaji, W. Boulila, I. R. Farah, I. Romdhani, and A. Hussain, Comput. Sci. Rev. **39**, 100318 (2021).

89. R. Sharma and D. Sharma, editors , *New Trends and Applications in Internet of Things (IoT) and Big Data Analytics* (Springer International Publishing, Cham, 2022).

90. E. Müller, E. Arnold, O. Breitwieser, M. Czierlinski, A. Emmel, J. Kaiser, C. Mauch, S. Schmitt, P. Spilger, R. Stock, Y. Stradmann, J. Weis, A. Baumbach, S. Billaudelle, B. Cramer, F. Ebert, J. Göltz, J. Ilmberger, V. Karasenko, M. Kleider, A. Leibfried, C. Pehle, and J. Schemmel, Front. Neurosci. **16**, 884128 (2022).

91. Y. Zhou and S.-T. Han, Sci. Technol. Adv. Mater. **24**, 2263265 (2023).

92. C. D. Schuman, J. S. Plank, G. S. Rose, G. Chakma, A. Wyer, G. Bruer, and N. Laanait, in *Proc. 4th ACM Int. Conf. Nanoscale Comput. Commun.* (ACM, Washington D.C., 2017), pp. 1–7.

93. F. Zayer, W. Dghais, M. Benabdeladhim, and B. Hamdi, AEU - Int. J. Electron. Commun. **100**, 56 (2019).

94. P.-Y. Chen, B. Lin, I.-T. Wang, T.-H. Hou, J. Ye, S. Vrudhula, J. Seo, Y. Cao, and S. Yu, in *2015 IEEEACM Int. Conf. Comput.-Aided Des. ICCAD* (IEEE, Austin, TX, USA, 2015), pp. 194–199.

95. E. T. Rolls and G. Deco, *The Noisy BrainStochastic Dynamics as a Principle of Brain Function* (Oxford University Press, 2010).

96. Phys. Unserer Zeit **7**, 126 (1976).

97. C. Mead, in *Twenty-Third Asilomar Conf. Signals Syst. Comput. 1989* (IEEE, Pacific Grove, California, USA, 1989), pp. 1–1.

98. Y.-C. Hsieh, Y.-C. Lin, Y.-H. Huang, Y.-D. Chih, J. Chang, C.-J. Lin, and Y.-C. King, Discov. Nano **19**, 54 (2024).

99. S. Lim, M. Kwak, and H. Hwang, Nanotechnology **30**, 455201 (2019).

100. Y. K. Lee, J. W. Jeon, E.-S. Park, C. Yoo, W. Kim, M. Ha, and C. S. Hwang, Micromachines **10**, 306 (2019).

101. Y. Li and K.-W. Ang, Adv. Intell. Syst. **3**, 2000137 (2021).

102. P. Kumar, K. Zhu, X. Gao, S.-D. Wang, M. Lanza, and C. S. Thakur, Npj 2D Mater. Appl. **6**, 8 (2022).

103. W. S. Wang and L. Q. Zhu, Sci. Technol. Adv. Mater. **24**, 2152290 (2023).

104. J. H. Yoon, Y.-W. Song, W. Ham, J.-M. Park, and J.-Y. Kwon, APL Mater. **11**, 090701 (2023).

105. S.-T. Lee and J.-H. Lee, IEEE Trans. Electron Devices **70**, 1019 (2023).

106. N. Rathi, I. Chakraborty, A. Kosta, A. Sengupta, A. Ankit, P. Panda, and K. Roy, ACM Comput. Surv. **55**, 1 (2023).

107. X. Liang, Y. Luo, Y. Pei, M. Wang, and C. Liu, Nat. Electron. **5**, 859 (2022).

108. W. Ye, Y. Chen, and Y. Liu, IEEE Trans. Comput.-Aided Des. Integr. Circuits Syst. **42**, 448 (2023).

109. K. S. Ahmed and F. F. Shereif, in *Artif. Intell.*, edited by Y. (Cindy) Yi and H. An (IntechOpen, 2023).

110. Andor, 2020 (2020).

111. H.-U. Krebs, M. Weisheit, J. Faupel, E. Süske, T. Scharf, C. Fuhse, M. Störmer, K. Sturm, M. Seibt, H. Kijewski, D. Nelke, E. Panchenko, and M. Buback, 505 (2003).

112. A. Sambri, Pulsed Laser Deposition of Complex Transition Metal Oxides: Plume Expansion and Film Growth Alessia, research-article, Springer US, 2019.

113. M. I. Hossain and S. Mansour, Cogent Eng. **10**, (2023).

114. A. P. Piedade, F. Romeu, R. Branco, and P. V. Morais, in *Methods Film Synth. Coat. Proced.*, edited by L. Nánai, A. Samantara, L. Fábián, and S. Ratha (IntechOpen, 2020).

115. M. Strikovski and J. H. Miller, Appl. Phys. Lett. **73**, 1733 (1998).

116. C. Yu, A. S. Sokolov, P. Kulik, and V. G. Harris, J. Alloys Compd. **814**, 152301 (2020).

117. N. A. Shepelin, Z. P. Tehrani, N. Ohannessian, C. W. Schneider, D. Pergolesi, and T. Lippert, Chem. Soc. Rev. **52**, 2294 (2023).

118. A. T. B.N. Chicbkov, C. Momma, S. Nolte, F. yon Alvensleben, Appl. Mater. Phys. A **6**, 239 (1996).

119. B. Stuart, M. Feit, S. Herman, A. Rubenchik, B. Shore, and M. Perry, Phys. Rev. B - Condens. Matter Mater. Phys. **53**, 1749 (1996).

120. J. Theerthagiri, K. Karuppasamy, S. J. Lee, R. Shwetharani, H. S. Kim, S. K. K. Pasha, M. Ashokkumar, and M. Y. Choi, Light Sci. Appl. **11**, (2022).

121. J. Haverkamp, R. M. Mayo, M. A. Bourham, J. Narayan, C. Jin, and G. Duscher, J. Appl. Phys. **93**, 3627 (2003).

122. M. I. Hossain, S. Mansour, A. Ojeda-G-P, C. W. Schneider, M. Döbeli, T. Lippert, A. Wokaun, F. H. Read, A. Ojeda-G-P, C. W. Schneider, M. Döbeli, T. Lippert, and A. Wokaun, J. Appl. Phys. **121**, 135306 (2017).

123. H. Koinuma, M. Kawasaki, S. Ohashi, M. Lippmaa, N. Nakagawa, M. Iwasaki, and X. G. Qiu, Supercond. Relat. Oxides Phys. Nanoeng. III **3481**, 153 (1998).

124. K. Sarakinos, D. Magnfält, V. Elofsson, and B. Lü, Surf. Coat. Technol. **257**, 326 (2014).
125. S. N. Ogugua, O. M. Ntwaeaborwa, and H. C. Swart, Coatings **10**, 1 (2020).
126. X. Li and Y. Guan, Nanotechnol. Precis. Eng. **3**, 105 (2020).
127. A. Singh, Z. R. Khan, P. M. Vilarinho, V. Gupta, and R. S. Katiyar, Mater. Res. Bull. **49**, 531 (2014).
128. T.-K. Lin, C.-E. Wu, H.-W. Chang, C.-R. Wang, D.-H. Wei, C.-S. Tu, and P. Y. Chen, Surf. Coat. Technol. **479**, 130557 (2024).
129. R. P. Laughlin, D. A. Currie, R. Contreras-Guererro, A. Dedigama, W. Priyantha, R. Droopad, N. Theodoropoulou, P. Gao, and X. Pan, J. Appl. Phys. **113**, 17D919 (2013).
130. I. Mirza, N. M. Bulgakova, J. Tomáštík, V. Michálek, O. Haderka, L. Fekete, and T. Mocek, Sci. Rep. **6**, 1 (2016).
131. A. Ojeda-G-P, M. Döbeli, and T. Lippert, Adv. Mater. Interfaces **5**, 1 (2018).
132. S. S. Yap, T. K. Yong, C. H. Nee, and T. Y. Tou, Appl. Laser Ablation - Thin Film Depos. Nanomater. Synth. Surf. Modif. (2016).
133. Y. J. Shin, L. Wang, Y. Kim, H. H. Nahm, D. Lee, J. R. Kim, S. M. Yang, J. G. Yoon, J. S. Chung, M. Kim, S. H. Chang, and T. W. Noh, ACS Appl. Mater. Interfaces **9**, 27305 (2017).
134. O. Ceballos-Sanchez, A. Sanchez-Martinez, F. J. Flores-Ruiz, A. M. Huerta-Flores, L. M. Torres-Martínez, R. Ruelas, and M. García-Guaderrama, J. Alloys Compd. **832**, 154923 (2020).
135. V. S. Dharmadhikari, S. R. Sainkar, S. Badrinarayan, and A. Goswami, J. Electron Spectrosc. Relat. Phenom. **25**, 181 (1982).
136. T. Yamashita and P. Hayes, Appl. Surf. Sci. **254**, 2441 (2008).
137. H. Tan, Z. Zhao, W. Bin Zhu, E. N. Coker, B. Li, M. Zheng, W. Yu, H. Fan, and Z. Sun, ACS Appl. Mater. Interfaces **6**, 19184 (2014).
138. T. Yang, J. Wei, Y. Guo, Z. Lv, Z. Xu, and Z. Cheng, ACS Appl. Mater. Interfaces **11**, 23372 (2019).
139. Q. Micard, G. G. Condorelli, and G. Malandrino, Nanomaterials **10**, (2020).
140. M. A. Khan, T. P. Comyn, and A. J. Bell, Acta Mater. **56**, 2110 (2008).
141. Y. Liu, H. Huang, and X. Lin, Key Eng. Mater. **537**, 224 (2013).
142. D. Ielmini and S. Ambrogio, Nanotechnology **31**, 092001 (2020).
143. E. Linn, R. Rosezin, S. Tappertzhofen, U. Böttger, and R. Waser, Nanotechnology **23**, 305205 (2012).
144. M. C. Nwadiugwu, (2020).
145. W. Ou, S. Xiao, C. Zhu, W. Han, and Q. Zhang, Front. Neurorobotics **16**, 1041108 (2022).
146. H. Chen, H. Li, T. Ma, S. Han, and Q. Zhao, Sci. Technol. Adv. Mater. **24**, 2183712 (2023).
147. C. Li, X. Zhang, P. Chen, K. Zhou, J. Yu, G. Wu, D. Xiang, H. Jiang, M. Wang, and Q. Liu, iScience **26**, 106315 (2023).
148. S. Kim, Y. Lee, M. Park, G. Go, Y. Kim, W. Xu, H. Lee, H. Kim, D. Seo, W. Lee, and T. Lee, Adv. Electron. Mater. **5**, 1900008 (2019).
149. S.-J. Ding, J. Xu, Y. Huang, Q.-Q. Sun, D. W. Zhang, and M.-F. Li, Appl. Phys. Lett. **93**, 092909 (2008).
150. X. Zhao, S. Menzel, I. Polian, H. Schmidt, and N. Du, Nanomaterials **13**, 1325 (2023).
151. Y. Dan and M.-M. Poo, Physiol. Rev. **86**, 1033 (2006).
152. J. H. C. Palmer and P. Gong, Front. Comput. Neurosci. **8**, (2014).

153. C. Jiang, H. Xu, L. Yang, J. Liu, Y. Li, K. Takei, and W. Xu, Nat. Commun. **15**, 2109 (2024).

154. Y.-F. Chang, B. Fowler, Y.-C. Chen, F. Zhou, C.-H. Pan, T.-C. Chang, and J. C. Lee, Sci. Rep. **6**, 21268 (2016).

155. T. V. P. Bliss and S. F. Cooke, Clinics **66**, 3 (2011).

156. C. D. Wright, P. Hosseini, and J. A. V. Diosdado, Adv. Funct. Mater. **23**, 2248 (2013).

157. E. Linn, R. Rosezin, S. Tappertzhofen, U. Böttger, and R. Waser, Nanotechnology **23**, (2012).

158. M. Hu, C. E. Graves, C. Li, Y. Li, N. Ge, E. Montgomery, N. Davila, H. Jiang, R. S. Williams, J. J. Yang, Q. Xia, and J. P. Strachan, Adv. Mater. **30**, 1 (2018).

159. T. Van Nguyen, J. An, and K. S. Min, Micromachines **12**, (2021).

160. V. Saxena, X. Wu, and K. Zhu, Proc. - IEEE Int. Symp. Circuits Syst. **2018-May**, 1 (2018).

161. M. C. Nwadiugwu, (2020).

162. I. Boybat, M. Le Gallo, S. R. Nandakumar, T. Moraitis, T. Parnell, T. Tuma, B. Rajendran, Y. Leblebici, A. Sebastian, and E. Eleftheriou, Nat. Commun. **9**, 1 (2018).

163. J. D. Kendall and S. Kumar, Appl. Phys. Rev. **7**, (2020).

164. H. Yu, J. Gong, H. Wei, W. Huang, and W. Xu, Mater. Chem. Front. **3**, 941 (2019).

165. S. Majumdar, H. Tan, Q. H. Qin, and S. van Dijken, Adv. Electron. Mater. **1800795**, 1 (2019).

166. V. K. Sangwan, H. S. Lee, H. Bergeron, I. Balla, M. E. Beck, K. S. Chen, and M. C. Hersam, Nature **554**, 500 (2018).

167. G. Dayal and K. B. Jinesh, ACS Appl. Electron. Mater. **4**, 592 (2022).

168. N. Wang, X. Luo, L. Han, Z. Zhang, R. Zhang, H. Olin, and Y. Yang, Nano-Micro Lett. **12**, (2020).

169. L. Liu, S. Zhang, Y. Luo, G. Yuan, J. Liu, J. Yin, and Z. Liu, J. Appl. Phys. **111**, 1 (2012).

170. A. Chen, W. Zhang, L. R. Dedon, D. Chen, F. Khatkhatay, J. L. MacManus-Driscoll, H. Wang, D. Yarotski, J. Chen, X. Gao, L. W. Martin, A. Roelofs, and Q. Jia, Adv. Funct. Mater. **30**, 1 (2020).

171. X. Chen, H. Zhang, T. Wang, F. Wang, and W. Shi, Phys. Status Solidi Appl. Mater. Sci. **209**, 1456 (2012).

172. R. Yang, S. Lin, X. Fang, X. Gao, M. Zeng, and J. Liu, J. Appl. Phys. **114**, 1 (2013).

173. A. Mijiti, M. Mamat, F. Xiaerding, Q. Wang, A. Abudurexiti, and L. Aihaiti, Mater. Res. Express **8**, (2021).

174. J. H. Jhang, J. A. Boscoboinik, and E. I. Altman, J. Chem. Phys. **152**, (2020).

175. J. G. Simmons, Phys. Rev. **155**, 657 (1967).

176. J. S. Lee, S. Lee, and T. W. Noh, Appl. Phys. Rev. **2**, (2015).

177. P.-Y. Chen and S. Yu, IEEE Des. Test **PP**, 1 (2018).

178. Z. Wang, L. Wang, M. Nagai, L. Xie, M. Yi, and W. Huang, Adv. Electron. Mater. **3**, (2017).

179. H. Z. Shouval, S. S. H. Wang, and G. M. Wittenberg, Front. Comput. Neurosci. **4**, 1 (2010).

180. T. Yang, J. Wei, Z. Lv, Z. Xu, and Z. Cheng, J. Mater. Sci. Mater. Electron. **30**, 12163 (2019).

181. C. Bengel, K. Zhang, J. Mohr, T. Ziegler, S. Wiefels, R. Waser, D. Wouters, and S. Menzel, Front. Electron. Mater. **3**, 1 (2023).

182. K. Yang, J. Joshua Yang, R. Huang, and Y. Yang, Small Sci. **2**, 2100049 (2022).

183. P. Y. Chen, B. Lin, I. T. Wang, T. H. Hou, J. Ye, S. Vrudhula, J. S. Seo, Y. Cao, and S. Yu, 2015 IEEEACM Int. Conf. Comput.-Aided Des. ICCAD 2015 194 (2016).

184. U. Shin, M. Ishii, A. Okazaki, M. Ito, M. J. Rasch, W. Kim, A. Nomura, W. Choi, D. Koh, K. Hosokawa, M. BrightSky, S. Munetoh, and S. Kim, Adv. Intell. Syst. **4**, 2200034 (2022).

185. M. J. Filipovich, Z. Guo, B. A. Marquez, H. D. Morison, and B. J. Shastri, in *2020 IEEE Photonics Conf. IPC* (IEEE, Vancouver, BC, Canada, 2020), pp. 1–2.

186. S. Kunwar, Z. Jernigan, Z. Hughes, C. Somodi, M. D. Saccone, F. Caravelli, P. Roy, D. Zhang, H. Wang, Q. Jia, J. L. MacManus-Driscoll, G. Kenyon, A. Sornborger, W. Nie, and A. Chen, Adv. Intell. Syst. **2300035**, (2023).

187. Y. Gao, S. Wu, and G. C. Adam, ACM Int. Conf. Proceeding Ser. 28 (2020).

188. W. Q. Pan, J. Chen, R. Kuang, Y. Li, Y. H. He, G. R. Feng, N. Duan, T. C. Chang, and X. S. Miao, IEEE Trans. Electron Devices **67**, 895 (2020).

189. J. J. Wang, S. G. Hu, X. T. Zhan, Q. Yu, Z. Liu, T. P. Chen, Y. Yin, S. Hosaka, and Y. Liu, Sci. Rep. **8**, 1 (2018).

190. U. Shin, M. Ishii, A. Okazaki, M. Ito, M. J. Rasch, W. Kim, A. Nomura, W. Choi, D. Koh, K. Hosokawa, M. BrightSky, S. Munetoh, and S. Kim, Adv. Intell. Syst. **4**, 2200034 (2022).

191. E. Miranda and J. Suñé, *Memristors for Neuromorphic Circuits and Artificial Intelligence Applications* (2020).

192. V. Milo, G. Malavena, C. M. Compagnoni, and D. Ielmini, Materials **13**, 166 (2020).

193. Elishai Ezra Tsur, *Neuromorphic Engineering The Scientist's, Algorithm Designer's, and Computer Architect's Perspectives on Brain- Inspired Computing* (2022).

194. M. K. Kim, Y. Park, I. J. Kim, and J. S. Lee, iScience **23**, 101846 (2020).

195. C. Sung, H. Hwang, and I. K. Yoo, J. Appl. Phys. **124**, (2018).

196. A. Krishnaprasad, N. Choudhary, S. Das, D. Dev, H. Kalita, H. S. Chung, O. Aina, Y. Jung, and T. Roy, Appl. Phys. Lett. **115**, (2019).

197. T. H. Lee, H. G. Hwang, J. U. Woo, D. H. Kim, T. W. Kim, and S. Nahm, ACS Appl. Mater. Interfaces **10**, 25673 (2018).

198. M. K. F. Lee, Y. Cui, T. Somu, T. Luo, J. Zhou, W. T. Tang, W.-F. Wong, and R. S. M. Goh, ACM Trans. Archit. Code Optim. **15**, 1 (2019).

199. D. Kuzum, R. G. D. Jeyasingh, S. Yu, and H. S. P. Wong, IEEE Trans. Electron Devices **59**, 3489 (2012).

LIST OF PUBLICATIONS

Journal Publications

1. **Linear Weight Update and Large Synaptic Responses in Neuromorphic Devices Comprising Pulsed Laser Deposited $BiFeO_3$**

G. Dayal and K.B. Jinesh (Published in ACS Applied Electronic Materials, DOI: 10.1021/acsaelm.1c00958)

2. **Correlation Between Oxygen Vacancies and Neuromorphic Properties of Pulsed-Laser-Deposited Bismuth Iron Oxide Artificial Synapses**

G. Dayal and K.B. Jinesh (Published: Applied Physics A, DOI: 10.1007/s00339-023-07060-8)

3. **Resistive switching in formamidinium lead iodide perovskite nanocrystals: a contradiction to the bulk form.**

Chinnadurai Muthu, A. N. Resmi, Johnpaul K. Pious, G. Dayal, Nayana Krishna, K. B. Jinesh and C. Vijayakumar (Published in Journal of Material Chemistry C, DOI: 10.1039/D0TC03275A)

4**. Self-Assembly of Delta-Formamidinium Lead Iodide Nanoparticles to Nanorods: Study of Memristor Properties and Resistive Switching Mechanism**

Chinnadurai Muthu, A N Resmi, Avija Ajayakumar, N E Aswathi Ravindran, G Dayal, K B Jinesh, Konrad Szaciłowski, Chakkooth Vijayakumar (Published in Small, DOI: 10.1002/smll.202304787)

5. **Plasma-Enhanced Atomic Layer Deposition of Titanium Oxynitride (TiOxNy) Thin Films and their Neuromorphic Applications**

Soundararaj Annamalai, Gopalakrishnan Dayal, Jayesh Gondhalekar, and Kochupurackal B. Jinesh (Published in ACS Applied Electronic Materials, DOI: 10.1021/acsaelm.3c01343)

6. **Ultra-high Seebeck coefficient of nanostructured Sb-substituted PbTe and fabrication of a thermoelectric generator module**

P R Sreeram, Neethu M Nair, G Dayal, Senoy Thomas, M R Anantharaman (Published in Bulletin of Materials Science, DOI: 10.1007/s12034-020-02262-9)

7. **Pattern recognition and pulse parameters in a bismuth iron oxide thin film neuromorphic device**

G. Dayal, Gondhalekar Jayesh and K.B. Jinesh (Under Preparation)